
Electrophoretic deposition of inorganic-organic nanocomposites

By

Xinya Zhao, B.ENG

A Thesis

Submitted to the School of Graduate Studies in

Partial Fulfilment of the Requirements for the Degree of:

Master of Applied Science

McMaster University

©Copyright by Xinya Zhao, July 2018

MASTER OF APPLIED SCIENCE (2018)
(Materials Science and Engineering)

McMaster University
Hamilton, Ontario

TITLE: Electrophoretic Deposition of Inorganic-Organic
Nanocomposites

AUTHOR: Xinya Zhao, B. Eng. (Southwest Jiaotong University,
Chengdu, China)

SUPERVISOR: Prof. Igor Zhitomirsky, Distinguished Engineering
Professor, Ph.D., P.Eng.

NUMBER OF PAGES: XVI, 121

Abstract

With many processing advantages, electrophoretic deposition (EPD) has been chosen as the fabrication technique for inorganic-organic nanocomposites. However, before the EPD process, avoiding the particles agglomeration is considered a necessary prerequisite for the success of fabrication.

In this research, two different liquid-liquid extraction methods, one is one-step and the other is two-step, were developed to solve the agglomeration problem of inorganic particles. The adsorption mechanisms of the extractors and extraction mechanisms were investigated during this work. The strong adsorptions provided by –OH groups of the extractors and further Schiff base reaction allowed for the process of extraction.

In the fabrication, polyelectrolytes acted as the film forming and charging agents. Relatively stable suspensions with extracted inorganic particles were prepared for the EPD of inorganic-organic nanocomposites. The thickness of deposited films is proportional to the concentration of the suspension and deposition time. With the addition of flame retardant inorganic particles, the prepared nanocomposite films showed an enhanced flame retardant performance.

Key words: EPD, inorganic-organic nanocomposites, liquid-liquid extraction

Acknowledgement

First, I would like to express my deepest gratitude to my supervisor Prof. Igor Zhitomirsky for his intellectual guidance, patience and encouragement during my graduate studies. Thank you for your tolerance and support in these two years. I feel so lucky and proud to have a supervisor like you.

I would like to thank my groupmates, Jieming Li, Haoyu Fan, Zhengzheng Wang, Mustafa Ata, Cameron Wallar, Amanda Clifford, Ryan Poon, Aseeb Syed and Jordan Milne for their collaboration and kindness of helping me in my graduate research life.

I would like to thank my roommates, Huifang Pang and Mengjie Bian, for their support, help and encouragement in my life. I will never forget our agreement and dreams. I would also like to thank other friends who I met in Canada for their help and kindness.

Last, but the most important, I wish to express my appreciation to my parents. I would like to thank my parents for their support, understand, encouragement and endless love for me. I am so fortunate to have parents like my mom and dad.

Declaration of Academic Achievements

This dissertation is used to fulfill the requirements of M.A.Sc degree. The major research project was undertaken from Sep 2016 to July 2018. I carried out experimental and theoretical research on developing inorganic-organic nanocomposites by EPD and liquid-liquid extraction.

The results of this dissertation were published in 5 papers in peer-reviewed journals. The papers were listed below:

1. **X. Zhao**, A. Clifford, R. Poon, R. Mathews, I. Zhitomirsky, Carbonxymethyl cellulose and composite films prepared by electrophoretic deposition and liquid-liquid extraction, *Colloid and Polymer Science*, 2018, 296, 927-934
2. R Poon, **X Zhao**, MS Ata, A Clifford, I Zhitomirsky, Phase transfer of oxide particles for application in thin films and supercapacitor, *Ceramics International*, 2017, 43, 8314-8320
3. T. Zhang, **X. Zhao**, R. Poon, A. Clifford, R. Mathews, I. Zhitomirsky, Synthesis and liquid-liquid extraction of non-agglomerated Al(OH)₃ particles for deposition of cellulose matrix composite films, *Journal of Colloid and Interface Science*, 2017, 508, 49-55
4. Ri Chen, Mustafa S. Ata, **Xinya Zhao**, Amanda Clifford, Ishwar Puri, Igor Zhitomirsky, Strategies for liquid-liquid extraction of oxide particles

for applications in supercapacitor electrodes and thin films, *Journey of Colloid and Interface Science*, 2017, 499, 1-8

5. R Chen, MS Ata, **X Zhao**, I Puri, I Zhitomirsky, Liquid-Liquid extraction of oxide particles and application in supercapacitors, *Journal of Materials Research*, 2017, pp. 3242-3250

Table of Contents

Acknowledgement.....	III
Declaration of Academic Achievements.....	IV
List of Figures	X
List of Tables.....	XVI
2. Literature review	3
2.1 Particle interactions and suspension stability.....	3
2.1.1 The DLVO theory	3
2.1.2 Other interparticle forces	6
2.2 EPD	9
2.2.1 EPD mechanism.....	9
2.2.2 Kinetics of EPD and electrophoretic mobility	13
2.2.3 Solvents.....	16
2.2.4 Charging methods of particle.....	18
2.2.5 Dispersants and dispersion mechanisms	21
2.2.6 Binders	25
2.3 EPD of polymers.....	27
2.3.1 Anodic EPD	28

2.3.2 Cathodic EPD	29
2.3.3 Other techniques	30
2.4 EPD of organic-inorganic composites	33
2.5 Applications of EPD	35
3. Objective	38
4. Experimental Methodologies	39
4.1 Starting Materials	39
4.2 Synthesis of TiO ₂ and Al(OH) ₃	40
4.3 EPD	41
4.4 Characterization techniques	41
4.4.1 X-ray diffraction analysis.....	41
4.4.2 Fourier transform infrared spectroscopy.....	42
4.4.3 Scanning electron microscope	42
4.4.4 Thermogravimetric and differential thermal analysis.....	42
4.4.5 Deposition yield study	43
4.4.6 Particle size distribution analysis.....	43
5. Results and discussion.....	44
5.1 Agglomeration of synthesized inorganic particles.....	44

5.2 Liquid-liquid extraction and cathodic EPD of cationic cellulose- Al(OH) ₃ composites	45
5.2.1 Two-step liquid-liquid extraction.....	45
5.2.2 Experimental results of liquid-liquid extraction	49
5.2.3 Structure and properties of QHECE.....	53
5.2.4 Experimental results of cathodic EPD	54
5.2.5. Conclusion	60
5.3 Liquid-liquid extraction and anodic EPD	61
5.3.1 One-step liquid-liquid extraction	61
5.3.2 Experimental results of liquid-liquid extraction	65
5.3.3 Structure and properties of CMC	68
5.3.4 Experimental results of anodic EPD	69
5.4 Liquid-liquid extraction of titania	77
5.4.1 Synthesis of TiO ₂	77
5.4.2 Experimental results of liquid-liquid extraction	77
5.4.3 Conclusion	86
5.5 Cathodic EPD of LPEI and its composite films.....	86
5.5.1 Experimental results of Cathodic EPD of LPEI composite films	88

5.5.2 Conclusion	96
6. Conclusions	98
7. References	101

List of Figures

Figure. 2-1. Total interaction between spherical particles as a function of particle separation according to the DLVO theory

Figure. 2-2. Schematic drawing of electrophoretic deposition cell showing the process

Figure. 2-3. Thickness of coatings deposited using ELD and EPD

Figure. 2-4. Zeta potential of colloidal particles versus pH of the suspension

Figure. 2-5. Structures of Dopamine and DHC

Figure. 2-6. Structures of Gallic acid and Salicylic acid

Figure. 2-7. (a) bidentate chelating bonding, (b) bidentate bridging bonding (inner sphere), (c) bidentate bridging bonding (outer sphere)

Figure. 2-8. Cathodic electrophoretic deposition of ceramic particles (a) neutral and (b) charged polymer

Figure. 2-9. Anodic EPD process and Cathodic EPD process

Figure. 5-1. SEM image of $\text{Al}(\text{OH})_3$ powder

Figure. 5-2. Condensation reaction between surface OH groups

Figure. 5-3. Schematic of synthesis and extraction process, involving (a) modification of $\text{Al}(\text{OH})_3$ particles with R-CHO during synthesis in an aqueous phase and (b) particle extraction to n-butanol phase involving a Schiff base reaction of R-COH and NH_2L .

Figure. 5-4. (A) Chemical structure of (a) NH_2L , (b) $\text{R}'\text{-CHO}$ and (c) $\text{R}''\text{-CHO}$, (B) Schiff base reaction of R-CHO ($\text{R}=\text{R}'$ or R'') and NH_2L , (C) adsorption of (a,b) $\text{R}'\text{-CNH-L}$ and (c,d) $\text{R}''\text{-CNH-L}$ on Al(OH)_3 , involving (a,c) chelation and (b,d) bridging of Al atoms.

Figure. 5-5. Particle extraction involving (a,b) $\text{R}'\text{-CNH-L}$ and (c,d) $\text{R}''\text{-CNH-L}$, arrows show liquid-liquid interface.

Figure. 5-6. Particle size distribution for Al(OH)_3 particles, extracted to n-butanol using (A) $\text{R}'\text{-CNH-L}$ and (B) $\text{R}''\text{-CNH-L}$.

Figure. 5-7. FTIR spectra of (a) $\text{R}'\text{-CHO}$, (b) NH_2L , (c) Al(OH)_3 particles synthesized in the presence of $\text{R}'\text{-CHO}$, (d) Al(OH)_3 particles, extracted using $\text{R}'\text{-CNH-L}$.

Figure. 5-8. FTIR spectra of (a) $\text{R}''\text{-CHO}$, (b) Al(OH)_3 particles synthesized in the presence of $\text{R}''\text{-CHO}$, (c) Al(OH)_3 particles, extracted using $\text{R}''\text{-CNH-L}$.

Fig. 5-9. Chemical structure of QHECE

Figure. 5-10. Time dependence of QCM mass gain for deposition from 0.05 g/L QHECE solution at a cell voltage of 5V.

Figure. 5-11. Deposit mass versus QHECE concentration in solutions at a voltage of 30 V and a deposition time of 5 min. The deposit mass data represents average values for 3 experiments with error < 4%

Figure. 5-12. Sedimentation test for Al(OH)_3 , prepared by (a) precipitation and drying and (b) precipitation and extraction. The

suspensions contained 2g/L $\text{Al}(\text{OH})_3$ and 1g/L QHECE in a mixed water-alcohol solvent

Figure. 5-13. SEM image of a composite prepared by EPD from suspensions of 2g/L $\text{Al}(\text{OH})_3$ and 1g/L QHECE in a mixed water-alcohol solvent

Figure. 5-14. TGA (a) and DTA (b) data for as prepared $\text{Al}(\text{OH})_3$, the total mass loss at 800 °C was 40%

Figure. 5-15. TGA (a) and DTA (b) data for as-received QHECE, the mass loss at 200 and 800 °C was 9 and 95%, respectively

Figure. 5-16. TGA (a) and DTA (b) data for QHECE- $\text{Al}(\text{OH})_3$ composite, prepared by EPD from 2g/L $\text{Al}(\text{OH})_3$ and 1g/L QHECE suspensions in a mixed water-alcohol solvent, the mass loss at 200 and 800 °C was 13 and 73%, respectively

Figure. 5-17. Chemical structure of (A) LG and (C) HDPA. (B) adsorption mechanisms of LG, involving (a) chelating bidentate bonding and (b) bridging bidentate bonding. (D) adsorption mechanisms of HDPA, involving (a) chelating bidentate bonding, (b) bridging bidentate bonding, (c) chelating tridentate bonding and (d) bridging tridentate bonding

Figure. 5-18. One-step extraction mechanism (A-B1-B2-D and A-C1-C2-D) in extraction method 1: (A) $\text{Al}(\text{OH})_3$ particles precipitate in aqueous solutions, (B1) extractor is accumulated at the liquid-liquid interface and (B2) adsorption occurs at the interface, (C1) extractor is

transferred from n-butanol to the aqueous phase, (C2) extractor adsorption occurs in the bulk of the aqueous phase, and (D) $\text{Al}(\text{OH})_3$ particles are transferred to the n-butanol phase

Figure. 5-19. Suggested extraction mechanism for HDPA: (a) starting $\text{Al}_2(\text{SO}_4)_3$ solution; (b) formation of particles, containing adsorbed HDPA after addition of HDPA solution in alkali; (c) extraction of particles to the n-butanol phase; and (d) image of $\text{Al}(\text{OH})_3$ extraction using HDPA (arrow shows water-n-butanol interface)

Figure. 5-20. (A). As-precipitated $\text{Al}(\text{OH})_3$, (B). $\text{Al}(\text{OH})_3$ extraction using LG, (C). $\text{Al}(\text{OH})_3$ extraction using HDPA (arrows show water-n-butanol interface), and (D,E) particle size distribution for $\text{Al}(\text{OH})_3$ particles extracted by (D) LG and (E) HDPA

Figure. 5-21. FTIR spectra of (a) LG, (b) $\text{Al}(\text{OH})_3$ extracted using LG, (c) HDPA, and (d) $\text{Al}(\text{OH})_3$ extracted using HDPA

Figure. 5-22. Chemical structure of CMC

Figure. 5-23. A. Deposit mass versus deposition time, measured using QCM, for the deposition from 0.05 g/L CMC-Na at a deposition voltage of 5V. B. Deposit mass versus deposition time for the deposition from 5 g/L CMC-Na at a deposition voltage of 30V

Figure. 5-24. (a) FTIR spectra of as-received CMC-Na and (b) deposited material

Figure. 5-25. Sedimentation test for $\text{Al}(\text{OH})_3$, prepared by (a) precipitation and drying and (b) precipitation and extraction. The suspensions contained 2g/L $\text{Al}(\text{OH})_3$ and 1g/L CMC in a mixed water-alcohol solvent

Figure. 5-26. SEM image of a film, prepared by EPD from a suspension, containing 2g/L $\text{Al}(\text{OH})_3$, extracted using LG, and 1 g/L CMC in a mixed water-alcohol solvent

Figure. 5-27. TGA (a,b) and DTA data (c,d) for as-prepared $\text{Al}(\text{OH})_3$ (a,c) and a deposit (b,d), prepared by EPD from a suspension, containing 2 g/L $\text{Al}(\text{OH})_3$, extracted using LG, and 1 g/L CMC in a mixed water-alcohol solvent

Figure. 5-28. X-ray diffraction pattern of titania

Figure. 5-29. (a) as-prepared titania in water, (b) extraction by the addition of LG in n-butanol, (c) particle size distribution of titania extracted using LG and (d) SEM image of titania agglomerates

Figure. 5-30. FTIR spectra of (a) LG, (b) TiO_2 extracted using LG

Figure. 5-31. (a) as-prepared titania in water, (b) extraction of titania to the n-butanol solvent after addition of HDPA solution in n-butanol and mixing, red arrow shows the interface of water and n-butanol and (c) particle size distribution of titania extracted using HDPA

Figure. 5-32. FTIR spectra of (a) HDPA, (b) TiO_2 extracted using HDPA

Figure. 5-33. (A) as-prepared titania in water, modified with R-CHO (B) extracted titania using Schiff base reaction and (C) particle size distribution.

Figure. 5-34. FTIR spectra of (a) R-CHO, (b) NH₂L and (c) TiO₂ extracted using Schiff base reaction

Figure. 5-35. SEM image of a titania-PVB film

Figure. 5-36. Structure of LPEI

Figure. 5-37. A and B SEM images of LPEI-MgAlLDH film at different magnifications, prepared by EPD from 0.5 g/L LPEI solution, containing 1 g/L MgAlLDH at a deposition voltage of 30V

Figure. 5-38. A and B SEM images of LPEI-halloysite film at different magnifications, prepared by EPD from 0.5 g/L LPEI solution, containing 1 g/L halloysite at a deposition voltage of 30V

Figure. 5-39. A and B SEM images of LPEI-titania film at different magnifications, prepared by EPD from 0.5 g/L LPEI solution, containing 1 g/L titania at a deposition voltage of 30V

Figure. 5-40. (a) TGA and (b) DTA data for as-received halloysite

Figure. 5-41. (a) TGA and (b) DTA data for LPEI-halloysite composite film, prepared by EPD from 0.5 g/L LPEI solution, containing 1 g/L halloysite at a deposition voltage of 30V

Figure. 5-42. (a) TGA and (b) DTA data for as-received MgAlLDH

Figure. 5-43. (a) TGA and (b) DTA data for LPEI-MgAlLDH composite film, prepared by EPD from 0.5 g/L LPEI solution, containing 1 g/L MgAlLDH at a deposition voltage of 30V

List of Tables

Table 2-1 Examples of solvents used for EPD

Table 4-1 Materials purchased from commercial suppliers

1.Introduction

Currently, nanocomposites have generated a great amount of interests due to their combined properties from multiple individual components. Among all the composites, inorganic-organic nanocomposites are considered to be the most popular one with high application potentials in certain fields. The incorporation of inorganic components can provide the possibility of added thermal, mechanical, electronic, magnetic and optical properties that may be difficult to add by using polymers alone. Consequently, different compositions, systems and strategies have been developed for the fabrication of inorganic-organic nanocomposites to meet the requirement of properties.

In many cases, layer-by-layer assembly, chemical vapor deposition, pulsed laser deposition and dip coating are chosen by researchers to fabricate inorganic-organic nanocomposites. However, these common techniques have some typical problems like complex procedures, high-cost and also low deposition rate. Alternatively, electrophoretic deposition (EPD), as an electrochemical method, is ideal for the fabrication of inorganic-organic nanocomposites with its low-cost, high deposition rate, simple procedure and also adequate control of coating thickness. Besides, EPD also has the capacitance to produce uniform deposits with high homogeneity and thus enhance the performance of the

composites.

Before the fabrication of composites by EPD, there is a strong need for solving the problem of particle agglomeration in the suspension. The agglomeration of particles is detrimental for the fabrication process and also for the performance of the resulting composites. Many efforts have been devoted to the development of dispersing agents focusing on the understanding of the structures of these additives. In our research, we employed liquid-liquid extraction method to avoid the agglomeration problem, and similarly, we tried to understand the structures of our extractors, which have various functional groups and therefore provide strong adsorption on inorganic particles.

For the fabrication of inorganic-organic nanocomposites, we used different EPD methods, such as cathodic EPD and anodic EPD, for different polymers with their different charging properties. The thickness of the resulting film can be manipulated by the variation of polymers concentration in the suspension and deposition time. Moreover, we analyzed and characterized the properties of the fabricated composites by different characterization methods.

The subject of my research is thus related to the development of novel liquid-liquid extraction methods and the fabrication of functional inorganic-organic nanocomposites by EPD techniques.

2. Literature review

2.1 Particle interactions and suspension stability

2.1.1 The DLVO theory

DLVO theory which was developed by Derjaguin and Landau, Verwey and Overbeek is considered a classic theory used for determining the stability of colloidal particles in suspensions.

In this theory, van der Waals attraction forces and Coulombic double-layer repulsion forces were considered to be the two main forces, which determine the total energy of interaction between two charged approaching particles¹. These two particles were assumed to be spherical with uniform charge distribution. The particles were identically charged and ions of opposite charge formed electrical double layers around the particles. The total energy V_T can be expressed as the sum of van der Waals attraction energy V_A and electrical double layer repulsive energy V_R :

$$V_T = V_A + V_R \quad (2-1)$$

If the attractive van der Waals force surpasses the repulsive electrostatic force, particle aggregation happens. If the repulsive force exceeds the attractive force, the colloid solution is stable. In order to change the

stability of colloid solution, it is necessary to alter the electrostatic force in the system.

The attractive energy V_A can be represented as

$$V_A = -\frac{A}{6} \left(\frac{2}{s^2-4} + \frac{2}{s^2} + \ln \frac{s^2-4}{s^2} \right) \quad (2-2)$$

where A is known as the Hamaker constant and $s = 2 + H/a$, with H being the shortest distance between the two spheres and a the particle radius. If $H \ll a$, equation (2-2) can be simplified into:

$$V_A = -A \frac{a}{12H} \quad (2-3)$$

The repulsive energy V_R is defined as:

$$V_R = 2\pi\epsilon\epsilon_0 a \varphi^2 \ln[1 + e^{-kH}] \quad (2-4)$$

where ϵ is the dielectric constant of the solvent, ϵ_0 is the vacuum dielectric permittivity, φ is the surface potential, $\frac{1}{k}$ is the Debye length:

$$k = \left(\frac{e^2 \sum n_i z_i^2}{\epsilon\epsilon_0 K T} \right)^{1/2} \quad (2-5)$$

where e is the electron charge, K is the Boltzmann constant, T is the absolute temperature, n_i is the concentration of ions with valence z_i . Repulsion between colloidal particles is determined by the diffuse double-layer charge on the particles.

The total interaction energy between the two particles versus interparticle distance is shown in Fig 2-1. When the Coulombic double-layer repulsion forces outweigh the van der Waals attraction forces in the two particles interaction system, the total energy shows positive in the graph, which indicates the particles are stable without coagulation. Moreover, when the

total energy reaches the maximum, it shows an energy barrier in the interaction system. This energy barrier can prevent the approaching of the two spherical particles and thus avoid particles coagulation.

Comparing the equation (2-3) with the combination of equation (2-4) and equation (2-5), it is obvious that both valence and concentration of electrolyte ions can determine the repulsion energy due to their influence on Debye length while the van der Waals energy is nearly independent of them. Based on this relation, the total energy can be controlled by changing the concentration and valence state of the electrolyte ions and the thus energy barrier can be changed at the same time. As the Fig 2-1 shows, with an increase in the concentration of the same electrolyte ions, the total potential energy shows a decrease and the energy barrier disappears, which result in the flocculation of the particles and the colloidal system is out of stability.

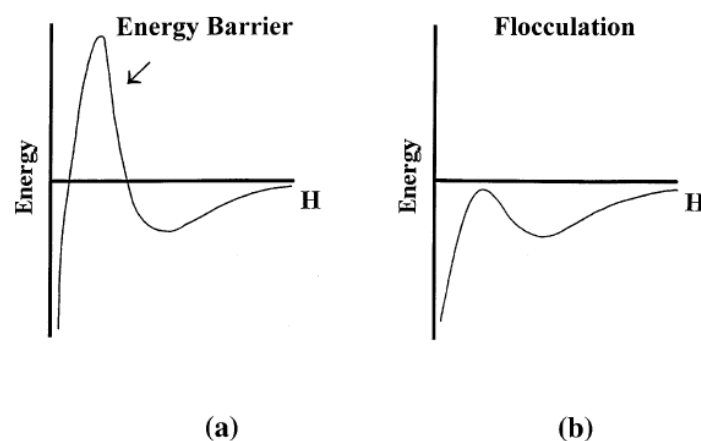


Figure. 2-1. Total interaction between spherical particles as a function of particle separation according to the DLVO theory².

According to the DLVO theory, R.M. Pashley^{3 4} measured the concentration needed for coagulation of divalent cation chloride solutions and concluded that divalent cations coagulate particles at lower concentrations than monovalent cations. Flocculation of ions compressing the double layer also follows the Hofmeister series⁵. Combining with the Hofmeister series, the flocculation value of some common ions increase with the following order²⁻⁵:



Therefore, at the same valence, a negatively charged colloidal particle with larger cation is flocculated at lower concentration than with the smaller one. Apart from that, the concentration and particle size of the sol and temperature also have a potential influence on the flocculation values.

2.1.2 Other interparticle forces

There is also some limitation of the DLVO theory because it only describes van der Waals attraction force and Coulumbic repulsion force. Based on the assumption that the two particles are smooth and flat, it fails to consider the interaction between surfaces with morphological heterogeneity (roughness) which are usually found in many practical colloidal phenomena⁶. S.Bhattacharjee⁶ employed techniques to generate

rough surfaces closing to the realistic models in practical circumstances. Comparing with the smooth surfaces, the incorporation of surface roughness can result in a considerable reduction in the repulsive energy. Moreover, the density and size of the asperities will affect the extent of repulsive energy reduction.

Some 'Extra-DLVO' forces, such as hydration forces, electrodynamic forces, hydrophobic, oscillatory forces⁷, have been pointed out to have a determination effect on colloidal stability. In aqueous solutions, some colloidal surfaces always have an extra stability related to a short-range interaction with adjacent water layers. R.M.Pashley^{3,4,8} explained the hydration forces existing in mica and proposed that the hydration force as an additional force is dependent on the interaction of hydrated cations adsorbed on the mica surface.

Due to the ignored ionic dispersion forces⁹, DLVO theory showed its flaws in the biological salt concentrations. DLVO theory always satisfy the work on low salt concentration (0.01M), where electrostatic forces dominate. However, in many systems with the concentration of 0.1M or higher and biological concentrations where electrostatic is screened, the ionic dispersion forces can dominate the electrostatic forces.

Through the measurements at a low pH and high salt concentrations, three additional forces have been found by W.Ducker¹⁰, oscillatory forces, monotonic repulsion forces and monotonic attractive forces, which are

similar to the hydration forces due to the chemisorption of water followed by protonation or deprotonation. These forces can be expected to consider the anomalous viscosity and consolidation behavior of alumina slurries at high concentration.

Hydrogen bonding¹¹ which widely exists in natural systems also plays an important role in the interparticle interactions. Functional groups on the particle surface can interact with water molecules by forming hydrogen bonding. These water molecules can perform like proton donor or acceptor groups on the surface and thus affect the surface properties and colloidal behaviors in aqueous solutions. Typical minerals possessing hydroxyl- and oxy-surface moieties and surface groups on hydrophilic clays can also help to form hydrogen bond with water molecules¹².

Solution chemistry¹¹ can also considerably influence a number of interfacial forces between particles and then control the stability of the particles. By changing the surface tension of water, additional indifferent electrolytes can lead to a decrease in particle stability. The addition of polymers to a colloidal suspension may bring about both attractive forces and repulsion forces and thus result in colloidal stability or particle coagulation, which is widely applied to the preparing of suspensions for EPD¹³.

2.2 EPD

2.2.1 EPD mechanism

With its high versatility and low cost, EPD is an electrochemical method widely used for the preparation of films, coating and even nano-structured composites. EPD is generally regarded as a two-step process. The first process is the motion of charged particles in a given electric field. These particles in the suspension are forced to move towards the opposite electrode under an electric field. In the second step, particles tend to be accumulated on the opposite electrode and form a uniform and adherent deposit on it. Both cathode and anode can be employed for the particles deposition, depending on the positive and negative charge of the particles. Due to the limits of substrates used for anodic EPD, cathodic EPD is preferred in industrial production². Van der Biest also pointed out that EPD results in a powder compact and a fully dense material that needs further densification manipulation such as sintering or curing¹⁴.

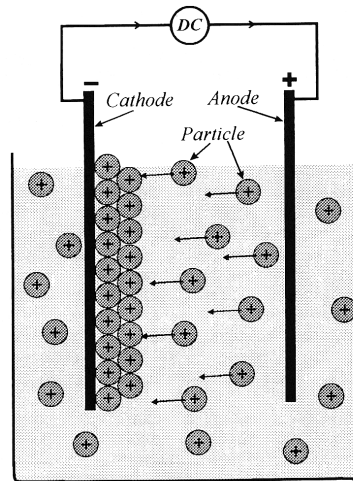


Figure. 2-2. Schematic drawing of electrophoretic deposition cell showing the process¹⁵

Compared with another common deposition method, electrolytic deposition(ELD), EPD can allow for the deposition of thicker films as the figure 2-3 illustrates.

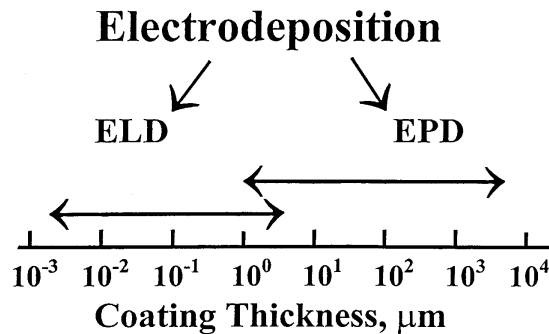


Figure. 2-3. Thickness of coatings deposited using ELD and EPD²

The first explanation of EPD was proposed by Hamaker and Verway^{15,16} in 1940. In their investigation, the mechanism of electrophoretic deposition has a parallel relationship with sedimentation caused by gravity. In addition to that, they considered the electric field only provides a force moving particles toward the electrode and pressing

particles accumulated on the electrode. Some other kinds of description about EPD mechanisms have been claimed after Hamaker and Verway and they almost take DLVO theory as the basis of the EPD mechanism but it cannot satisfy the needs of analyzing the EPD process.

Sarkar and Nicholson¹⁵ provided insight into the distortion of double layers during the motion of the particles. Both fluid dynamics and applied electric field can make the double layers of the ahead particle become thinner in this case, and attractive force surpasses repulsive force allowing for the coagulation of the particles. A following study of Nicholson¹⁷ improved this theory by claiming the chemical reaction of H^+ at the cathode and the resulting pH increase around the cathode can decrease the ζ potential that determines the stability of the colloidal particles as shown in fig.2-4 and thus deposition happens.

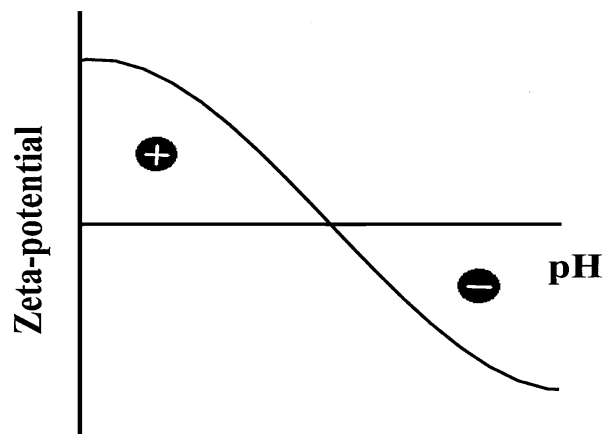


Figure. 2-4. Zeta potential of colloidal particles versus pH of the suspension²

Grillon¹⁸ introduced the electrical neutralization mechanism that the particles cannot leave as soon as they touch the electrode or already deposited particles. This mechanism is the basis of the highly porous deposition film and the deposition of monolayers. However, this mechanism cannot explain the depositions on semi-permeable membranes placed between the electrodes, which do not involve the contact between particles and electrodes¹⁹ and cannot be applied in the deposition of thicker films which needs longer time.

In the review of Van der Biest¹⁴, he showed the importance of hydroxides formed during deposition process, which is also a mechanism of deposition that cannot be ignored. For the suspension where powders are charged positively by the adsorption of metal ions, the processing current in the suspension can trigger the formation of hydroxides. $MgCl_2$, $Mg(NO)_3$ and $AlCl_3$ can be introduced as the additional metal salts providing metal ions. Powders charged by the adsorption of metal ions are required to be neutralized into uncharged metal hydroxides through the electrode reactions. These resulting hydroxides can enhance the coherence of the deposit and its adherence to the electrode surface. Different from the deposition mechanism of this kind of suspension, the particles charged by the adsorption or de-sorption of protons can be deposited by the pH increase of the surrounding area for both electrode surface and membranes placed near the electrode.

A theory presented by Ristenpart²⁰ pointed out that the electrodynamic flows around colloidal particles next to the electrode also makes a contribution to the long range particle-particle attraction near the electrode, which can promote the coagulation of particles on the electrode surface. In their analysis, the alteration of applied electric field has control over the fluid motion that carries particles moving in the suspension because the fluid velocity is proportional to the square of the given electric field and decreases with the increasing frequency.

2.2.2 Kinetics of EPD and electrophoretic mobility

A better understanding of EPD kinetics is important to achieve the controlling of the thickness of the deposits, structure and properties of the deposits²¹. According to the observation from Hamaker¹⁶, the deposition yield is proportional to the concentration of the suspension, deposition time, surface area of the deposit and applied electric field. This relationship can be expressed as the following equation,

$$\frac{dY}{dt} = f \cdot \mu \cdot E \cdot S \cdot c \quad (2-6)$$

where Y is the yield of deposition (kg), t is the deposition time (s), μ is the electrophoretic mobility ($\text{m}^2 \cdot \text{V}^{-1} \cdot \text{s}^{-1}$), S is the surface area of the electrode (m^2), c is the solid concentration ($\text{kg} \cdot \text{m}^{-3}$) and f is a factor concerned to satisfy the uncertain parts in the deposits because not all the powders in the suspension can be finally incorporated into the deposits

and thus the value of f is 1 or less¹⁴. This rate of deposition is very important for controlling the thickness of the deposited layer or getting graded materials¹⁵. As a fundamental rule, this equation can be applied in almost all the studies on the kinetics of EPD. Anne et al²² developed a mathematic model to describe the EPD kinetics of Al₂O₃-based suspension and concluded the needs of considering the changing electric field into the description of a more accurate deposition yield than only predicting through Hamaker equation.

Sarkar¹⁵ found the difference between the EPD kinetics under constant voltage and EPD kinetics existing in constant current process. A dramatic potential gradient is required in the EPD process, which can facilitate the increase of deposition yield. However, for the constant-voltage EPD system, the potential gradient between electrodes is constant, where the electric field E in the bulk of suspension and particle deposition rate can be consequently decreased. On the contrary, the constant-current EPD can avoid the problems in constant-voltage EPD by maintaining the constant E in the suspension and constant deposition rate.

Van der Biest¹⁴ divided the kinetics of EPD into two categories. One is the kinetics of single-powder deposition and another is the kinetics of co-deposition of two or more powders. During the process of co-deposition, different powders show the same deposition rate when the solid volume is high in the suspension. In another circumstance, when the

solid volume is low, powders are inclined to deposit at a proportional rate to their own electrophoretic mobility.

The velocity v of a particle in an electric field E is defined as:

$$v = \mu E \quad (2-7)$$

where μ is the electrophoretic mobility. The electrophoretic mobility of rigid particles and polyelectrolytes follow two different theories². The electrophoretic mobility of a rigid colloidal particle can be measured by the equation below,

$$\mu = \frac{2\varepsilon\varepsilon_0\zeta}{3\eta} f(\kappa\alpha) \quad (2-8)$$

where η is the liquid viscosity. The function $f(\kappa\alpha)$ increases from 1 for $\kappa\alpha \ll 1$ to 1.5 for $\kappa\alpha \gg 1$. For particles smaller than the Debye length, the electrophoretic mobility is expressed as Huckel formula,

$$\mu = \frac{2\varepsilon\varepsilon_0\zeta}{3\eta} \quad (2-9)$$

For particles larger than $1/\kappa$, the electrophoretic mobility is given by Smoluchowski equation,

$$\mu = \frac{\varepsilon\varepsilon_0\zeta}{\eta} \quad (2-10)$$

Different from the expression of electrophoretic mobility of rigid particles, that of polyelectrolytes can be described as the equation below,

$$\mu = \frac{\rho_{fix}}{\eta\lambda^2} \left[1 + \frac{2}{3} \left(\frac{\lambda}{\kappa} \right)^2 \frac{1+\lambda/2\kappa}{1+\lambda/\kappa} \right] \quad (2-11)$$

where $\lambda = \left(\frac{\gamma}{\eta} \right)^{\frac{1}{2}}$, and γ is the frictional coefficient of the polyelectrolyte.

Except for the factors mentioned above, particles interactions in concentrated suspensions and fluid motions involving individual particles have also been studied². The electrophoretic mobility decreases steeply with the increasing double layer thickness because of the overlapping between the electrical double layers of the particles.

2.2.3 Solvents

The success of electrophoretic deposition is related to the proper choice of the solvent. The solvent used in electrophoretic deposition must have the ability to dissolve both organic and inorganic components. Water and organic solvents are the two basic choices for the electrophoretic deposition. Table 1 concludes some typical solvents used in electrophoretic deposition².

Table 2-1 Examples of solvents used for EPD

Solvent	Deposited material
Water	Al ₂ O ₃
Ethyl alcohol-water	CaSiO ₃
Isopropyl alcohol	Hydroxyapatite
Ethyl alcohol-acetylacetone	MgO, Al ₂ O ₃
Glacial acetic acid	Lead zirconate titanate

Ethyl alcohol	Al_2O_3 , ZrO_2
Dichloromethane	β -alumina
Acetone	Lead zirconate titanate
Acetylacetone	Lead zirconate titanate
Cyclohexanone	Lead zirconate titanate
Methyl ethyl ketone	Al_2O_3
Toluene-ethyl alcohol	Al_2O_3

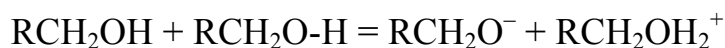
Organic liquids are preferred over water in most cases because organic solvent can protect the deposits from hydrating by extracting free water and nonbridging hydroxyl groups²³. Besides, in alcohol-water solutions, the additional alcohol can result in a decline in the total dielectric constant of the solvent and therefore reduces the solubility of the deposits, which can help to enhance the deposition rate². The decrease in dielectric constant leads to the consequent decrease in the thickness of the double layer, which can thus cause particle coagulation. Aruna and Rajam²⁴ studied the different ratios of acetone and ethanol mixture solvent and found that the intimate relation between the bath composition and weight and microstructure of deposits and concluded that the use of mixed solvents can avoid the cracking problems of the deposits. Du et al²⁵ also test the potential microstructures got from different composition of solvent and speculated that the reduction of porous size is related to

the decreasing of hydrogen ion concentration from additional ethanol. However, the deposition rate becomes slow for solvent mixtures where the volume of ethanol is higher than that of acetone and the film taken from this suspension also shows poor adhesion.

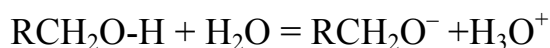
The solvent used for EPD also needs to be inert with deposits and thus organic liquids are always chosen as the solvent because they cannot cause gas formation like some water-based solvents².

2.2.4 Charging methods of particle

One way for particle charging is to charge particle through the suspension directly. Alcohols were found to be able to behave as proton donors by Damodaran and Moudgil²⁶. A pure alcohol can ionize as the following way,



and an aqueous alcohol ionize as follows,



For pure alcohol, the ionization process yields an alkoxide ion and a protonated alcohol. It was found that the calcium phosphate particles²⁶ can adsorb undissociated alcohol molecules on their surface and these

adsorbed alcohol molecules will ionize and the resulting protonated alcohol will dissociate and leave the proton on the particle surface. As a result, the particles are charged positively. Some other mixed solvents were also employed for charging particles, like acetylacetone-iodine²⁷, acetone-ethanol²⁵, acetone-water²⁸ and acetone-iodine²⁸, where acetone release protons for particle charging²⁹ and iodine or water works as a stabilizer^{28,29}.

Van der Biest¹⁴ showed that there are four mechanisms for particle charging: selective adsorption onto solid particles from liquid, dissociation of ions from solid phase into the liquid phase, adsorption of dipolar molecules on the particle surface and electron transfer between solid and liquid phase. Based on these four particle charging mechanisms, adding additives is a simple and efficient method for achieving charging particles.

Acids, bases, specifically adsorbed ions or polyelectrolytes are always selected as the charging agents for EPD³⁰. Concentrated acids were used as the charging agents for carbon nanotubes^{31,32} in some early studies. With the ionization of functional groups, such as $-\text{COOH}$, $-\text{OH}$, $-\text{C}=\text{O}$, acids can create a negatively charged surface and also provide hydrophilic sites onto the nanotube surface to impart cation-exchange properties. After thermal or chemical treatment of the attached functional groups, it was worth noting that the modified functional groups have an

enhancement effect on the capacitance of the carbon nanotubes³².

However, it was pointed out that acids can potentially react with powders and cause corrosion of the electrodes².

For charging ceramics, the adsorption of ions can be achieved from the solution of metal ions³³ but the incorporation of the corresponding hydroxides or oxides from the reactions of metal ions during EPD are possible to contaminate the deposits²⁹.

Organic molecules are always introduced to cause steric stabilization by attaching to the particle surface or deplete stabilization by keeping free in the suspension². This steric stabilization is applicable in both aqueous and non-aqueous solution. Polyelectrolytes used for charging particles can be divided into two categories, cationic charging agents and anionic charging agents³⁰. Polyethylene imines(PEI) and polyamines are two typical cationic polymers. PEI was found to achieve cationicity through protonation of its amine groups from the surrounding medium, which is affected by the pH of the suspension³⁰. The quaternary ammonium group of polyamine helps polyamine molecules maintain very strong cationic charge over a wide range of pH. For anionic charging agent like polyacrylic acid, the efficiency of charging is high at a pH where the “native” charge of the surface is minimal. There is also some limitation existing with polyelectrolytes due to the bridging flocculation of the small particles³⁴.

2.2.5 Dispersants and dispersion mechanisms

In order to prepare a stable suspension for EPD, adding a dispersant is usually required for the efficient dispersing of particles. Dispersants can first adsorb on the particles and then provide electrostatic repulsion or steric repulsion between particles to avoid agglomeration and achieve stable suspensions. Adsorption of a dispersant can be dramatically enhanced by coordinating with metal atom to form a complex³⁵. Some ionic dispersants can even function as charging agents that can impart charges to particles for their motion under applied electric field. It is worth noting that additional non-adsorbed ionic dispersant can be considered as an electrolyte which can increase the ionic strength of the suspension and decrease electrostatic repulsion between particles, resulting in the increasing tendency to agglomeration². This increased ionic strength can lead to an increase in the conductivity of the suspension and promote corresponding gas evolution at the electrodes.

Organic additives are considered as the most widely used dispersing agents for EPD due to their strong adsorption on oxide particles³⁶. The mechanism of organic additives for dispersing is based on increasing the repulsive forces between the ceramic particles. Some of these additives are charge-carrying long-chain polyelectrolytes which can adsorb on the particle surface and modify the surface charge of the particles in the

suspension and then enhance the electrostatic repulsion between the particles, which can form a steric barrier for agglomeration. However, these kinds of polyelectrolytes are always having high molecular weight. Hanaor³⁶ proposed carboxylic acid as a dispersant which has lower molecular weight than polyelectrolytes and shows higher adsorption capacitance and lesser effect on post-firing microstructure. Other organic molecules like catechol, gallic acid and salicylic acid also generated significant interest in working as dispersing agents because of their special functional groups, structure and size of molecules³⁴.

It was discovered that materials from catechol family always adhere effectively to oxide particle surface via their catechol group^{34,37}. Catechol group is composed of two OH groups bonded to adjacent carbon atoms of aromatic ring, which allows for strong adsorption on different surfaces. Dopamine, a typical material from catechol group, exhibits cationic properties through the protonation of its amino group in acidic solutions and thus increases particle charge for EPD of metal oxides³⁴. Apart from this, dopamine was discovered to adsorb on multiwalled carbon nanotubes (MWCNTs) with the help of π - π interaction. The resulting MWCNTs were well dispersed in MnO₂ and showed enhanced electrochemical performance³⁸.



Figure. 2-5. Structures of Dopamine and DHC³⁴

3,4-dihydroxyhydrocinnamic acid (DHC), an organic molecule with long hydrocarbon chains, imparts anionic properties ascribed to the carboxylic groups, which makes it work as a good dispersing and charging agent. DHC was investigated to adsorb on metal particles like Fe_3O_4 during synthesis and allow the fabrication of nanoparticles of a controlled size³⁹.

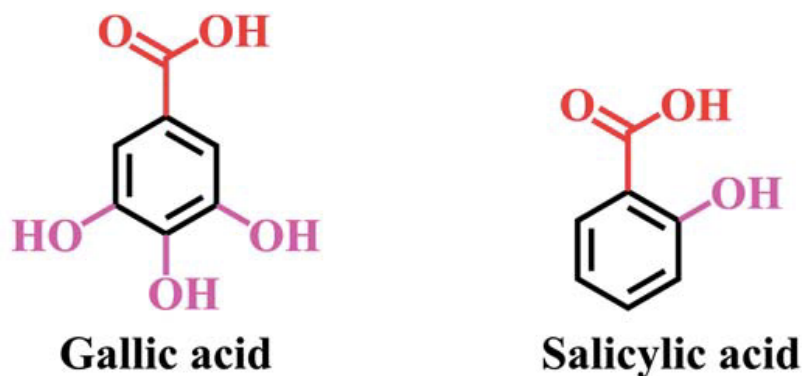


Figure. 2-6. Structures of Gallic acid and Salicylic acid³⁴

Gallic acid (GA) having three OH groups bonded to adjacent carbon atoms of aromatic ring and COOH group shows strong adsorption on a wide range of metal oxides. This adsorption mechanism is also related to

its OH groups and it was found that only two of the three OH groups participate in forming the complex while the third one and COOH group did not influence the stability of the complex⁴⁰.

As Fig.2-6 shows, salicylic acid (SA), an aromatic carboxylic acid, includes an OH group and a COOH bonded to adjacent carbon atoms of aromatic ring. Different from GA, the adsorption mechanism of SA on metal oxides is related to both OH and COOH groups. In an investigation of the adsorption mechanism of SA on TiO_2 ⁴¹, it was found that SA can give rise to three different kinds of surface complexes with TiO_2 by chemisorption, forming bidentate chelating bonding and bidentate bridging bonding (inner sphere and outer sphere). As Fig 2-7 depicts, the formation of an inner sphere complex showed a strongest adsorption because of the influence of molecule volume³⁵. Except for TiO_2 , SA also exhibited strong adsorption on Al_2O_3 ³⁵, ZrO_2 ⁴² and Fe_2O_3 ⁴³. The adsorption of SA onto metal oxides is dependent on the pH value³⁵.

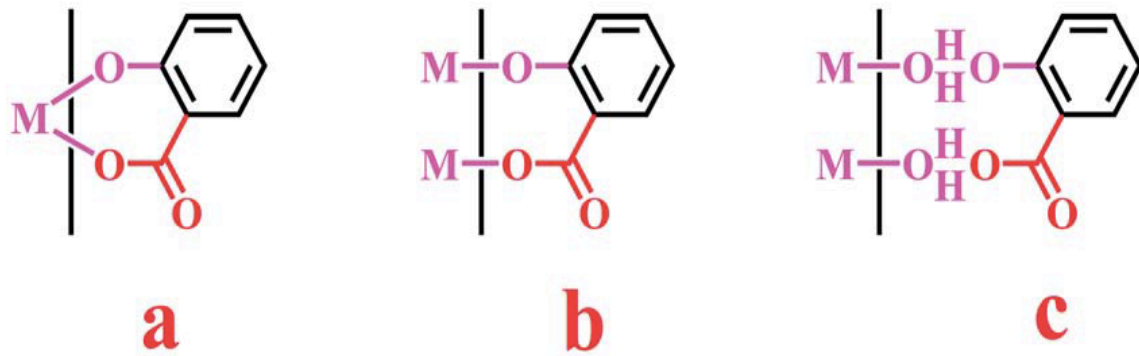


Figure. 2-7. a. bidentate chelating bonding, b. bidentate bridging bonding (inner sphere), c. bidentate bridging bonding (outer sphere)³⁴

2.2.6 Binders

Binders are common additives extensively used to improve the adherence of the particles to the substrate surface and prevent cracking of the deposits. Non-ionic-type polymers are considered as the primary binders used for EPD⁴⁴, having ability to increase the strength and toughness of the deposits. Such polymeric molecules can adsorb on and move with ceramic particles in a given electric field.

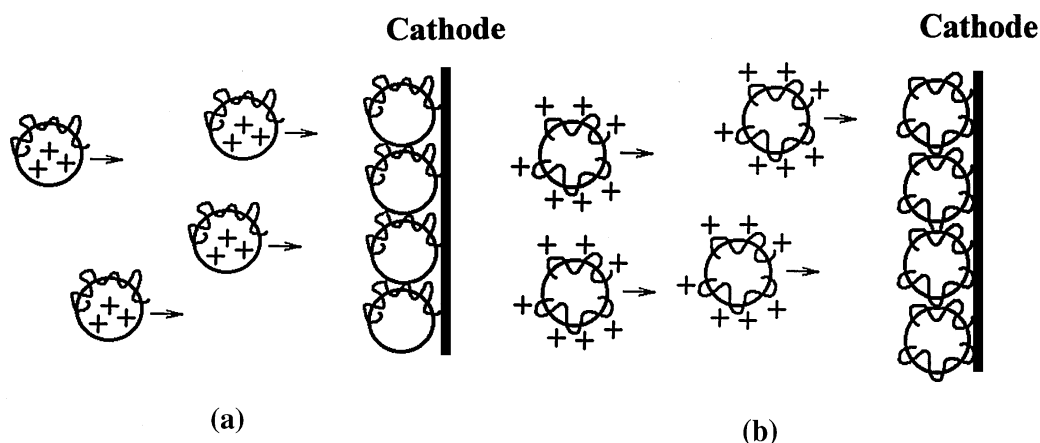


Figure. 2-8. Cathodic electrophoretic deposition of ceramic particles (a) neutral and (b) charged polymer²

There are two kinds of polymeric binders, electrically neutral polymer and charged polymer, always used in deposition. Charged polymer with inherent binding properties like cationic polymer can provide electrophoretic transport for ceramic particles and form deposits together without cracking on the cathodic electrode(Fig.2-8a). Based on this, organiceramic nanocomposites can be formed by EPD and consequently EPD is popular as a novel technique for the deposition of organic/inorganic nanocomposites². Compared with charged polymer binders, neutral polymer binders can be transported by charged ceramic particles to the electrode surface and incorporated in the deposit⁴⁵(Fig.2-8b).

Some metal salts can be added as additives to form binders for EPD, such as $Mg(NO_3)_2$ ⁴⁶⁻⁴⁸ and $Y(NO_3)_3$ ⁴⁹. It was found that the type of binders

formed in EPD was dependent on the amount of water in the suspension⁴⁶.

In a bath with very low amount of water, the binder material finally forms as alkoxide while the binder material primarily exists as hydroxide in a bath with high amount of water.

The stability and chemical compatibility of the binder-dispersant-solvent system are needed to be concerned before EPD⁵⁰.

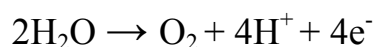
2.3 EPD of polymers

Polymer like polyetheretherketone (PEEK) can be coated on conductive carbon substrates via EPD to form biocompatible medical devices due to its safe, stable and biocompatible properties⁵¹. It was discovered that electrophoretically deposited copolymer poly(4-vinylpyridine-co-butyl methacrylate)(PVPBM)⁵² showed good binding and film forming properties on the surface of substrates, which can be applied in the corrosion protection fields. Except for EPD of pure polymers to be used as coatings and films, in order to improve the performance of the inorganic materials, polyelectrolytes are always preferred to be added into inorganic suspensions to form nanocomposites through EPD. It was found that the addition of polyelectrolytes could stabilize the suspension because the high molecular weight of polyelectrolytes exhibits larger electrostatic repulsive interaction and larger steric effect between

particles⁵³ and also improve the film adherence of the fabricated nanocomposites .

2.3.1 Anodic EPD

The choice between cathodic EPD and anodic EPD is dependent on the nature of particle charge⁵⁴. EPD does not involve the reaction between particles and electrodes. Moreover, there is no charge loss of ceramic particles during deposition¹⁵. In the process of anodic EPD, negatively charged particles are forced to move towards anode in a given electric field as fig.2-9 illustrates. The electrochemical decomposition of water can result in a decrease in pH near the anodic electrode,



which plays an essential role in the deposition of alginic acid or hyaluronic acid⁵⁵ through the neutralization of COO^- group in the low pH area at anodic electrode surface. Anodic EPD performed more effectively than cathodic EPD in the fabrication of metal-organic frameworks without destroying their crystal structures⁵⁶. However, anodic EPD can potentially cause oxidation or dissolution of non-noble electrodes in most cases and thus reduce the adherence of deposited film on the substrate⁵⁷.

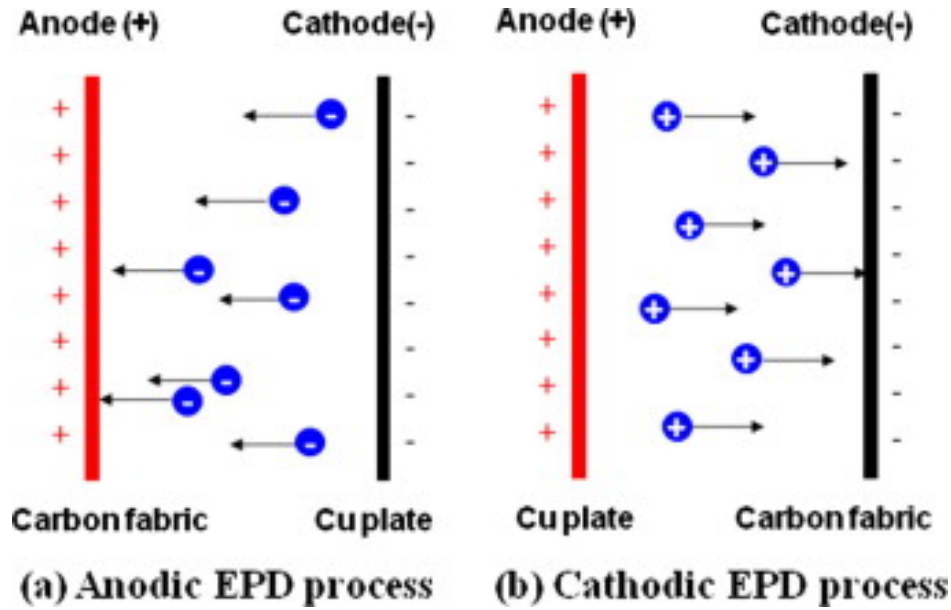
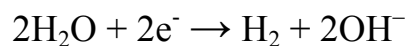


Figure. 2-9. Anodic EPD process and Cathodic EPD process⁵⁸

2.3.2 Cathodic EPD

In the process of cathodic EPD, positively charged particles tend to deposit on cathode. Chemically cleaned Ni foils⁵⁹, carbon steel discs⁶⁰, Pt foils⁶¹ and some other inert substrates⁶² are generally exploited as cathodic electrodes. Compared with anodic EPD, cathodic EPD can effectively avoid the oxidation of non-noble electrode⁶³. There exists a pH increase near the cathode, which is attributed to the cathodic reaction of water,



This can result in the charge neutralization of cations and consequently form hydroxides deposits on the electrode⁶³. The electrolysis of water in both anodic EPD and cathodic EPD can result in the generation of bubbles, which can disturb the electrophoresis of particles on the

substrate. Studies from Bersa⁶⁴ presented that the use of palladium cathodic electrode can effectively deposit high density films and prevent the associated problems from bubbles by adsorbing the generated hydrogen gas.

2.3.3 Other techniques

Apart from EPD, there are also some other common coating and film forming techniques such as layer by layer assembly⁶⁵, chemical vapor deposition⁶⁶, dip coating⁶⁷, spray coating⁶⁸, spin coating⁶⁹ and pulsed laser deposition⁷⁰. They present advantages over EPD in some specific deposition fields.

Layer by layer (LBL) assembly is mainly based on alternating electrostatic adsorption, beginning with the adsorption of charged species onto a substrate with opposite charge and leading to the reversal of substrate surface charge. Further layers can also be deposited by the alternative adsorption of opposite species onto the substrate⁷¹ and multilayer can be obtained by this cyclic deposition. The properties of LBL synthesized films are determined by the type of adsorbed species, the number of layers and the assembly conditions. LBL assembly has the capability to incorporate polyelectrolytes, nanotubes, inorganic molecular cluster, nanoparticles and even proteins and DNA⁷². LBL allows the high

loading of various biological components, which makes it extensively used in biomedical field. Additionally, LBL enables the fabrication of 3D multifunctional electronics that showed high-performance device characteristics⁷³.

Chemical vapor deposition (CVD) involves the decomposition of gas-phase molecules to reactive species which can result in the growth of films or particles⁷⁴. CVD is widely used in the deposition of conducting, semiconducting and insulating materials. It was found that CVD can obviously enhance the electronic properties of graphene⁷⁵. Continuous graphene films with single or few-layer can be grown by CVD on polycrystalline Ni⁷⁶ and also other kinds of substrates. This CVD synthesized graphene films can remain its conductivity even after several processing steps. Besides, one-step growth of graphene-carbon nanotube (CNT) hybrid materials were developed by Dong et al.⁷⁷ via CVD. This CVD synthesized hybrid materials exhibit higher conductivity than those CVD synthesized pure graphene films.

Dip coating is a type of sol-gel coating, having simple process to deposit a thin film from the solution onto the object with regular shape and even some complicated shape. The concentration of the solution was discovered to have an effect on particle size of the ZnO film⁷⁸ and film thickness. In an investigation from Li et al.⁷⁹, dip coating successfully helped hydroxyapatite coat on titanium with stronger bonding strength

and enhanced the biocompatibility of titanium rods that can be applied in the bone implantation. Dip-coated mesoporous silica membranes also present almost two to three times gas permeation rates than hydrothermally deposited ones, which is attributed to the uniform deposition results from dip coating⁸⁰.

Spin coating is another kind of sol-gel coating, which is widely used for the production of thin and ultra thin films⁸¹. During the process, solution is deposited on the substrate before rotation and then substrate accelerates in a desired rotation rate. The centrifugal force can help to spread the coating material and remove the excess. The thickness of the film is related to the concentration, viscosity, diffusivity of the solution⁸² and spin speed and time⁸³. As a simple and fast technique, spinning coating can even fabricate polymeric nanocomposites with high quality and large area coverage. It was demonstrated that spin coating can be also used for polymer molecular weight determination⁸⁴.

Having less steps and similar conversion efficiency, spray coating is considered as a better alternative to spin coating in the fabrication of polymer-based solar cells⁸⁵. Spray coating is established from graffiti art and painting, which is always applied as an ideal coating technique for substrates with different morphologies. With little waste of fluid, spray coating allows for a wide range of fluids and can even deposit any solution systems⁸⁵. As a typical spray coating technique, thermal spray

associated with particle melting is usually selected in steel industry⁸⁶.

Except for conventional thermal spray, cold spray without the requirement of high temperature, as a new kind of spray coating, is extensively employed in a variety of industrial applications, especially for corrosion protection^{87,88}.

Pulsed laser deposition (PLD) with energetic plasma is always chosen for depositing metal oxide thin films such as ZnO and CdO^{70,89}. In the process of PLD, the high power pulsed laser beam strikes on the target material, which result in the vaporization of the target material and the flux of the evaporated material is prone to condense on a substrate and form as a film. The process parameters like laser pulse wavelength and substrate temperature were found to have an influence on the properties of produced films⁹⁰. The ZnO films prepared by PLD showed better optical and electrical properties than films prepared by other techniques^{70,91}.

2.4 EPD of organic-inorganic composites

With the combined properties from inorganic and organic components, organic-inorganic composites have attracted much attention in various fields. As a simple and low-cost deposition technique, EPD offers advantages for the fabrication of organic-inorganic composites. In a

review from Zhitomirsky⁹² of EPD of nanocomposites, polyelectrolytes always act as a matrix and inorganic particles are embedded in it. There are many factors that influence the properties and microstructure of the resulting films like pH, bath composition and molecular weight of polyelectrolytes. Accordingly, composite film can be tailored to satisfy the needs of desired properties.

Polyelectrolytes used in EPD can be divided into two categories, strong polyelectrolytes and weak polyelectrolytes. The ionization of strong electrolytes is independent of pH while the ionization of weak polyelectrolytes can be altered by pH. Based on this, the manipulation of the charge and solubility of polymer can be achieved by changing the pH of a system having weak polyelectrolytes.

It has been pointed out that the formation of composite deposit is influenced by the interactions between polyelectrolytes and inorganic particles on the electrode surface. EPD of PDDA in aqueous solution is failed but co-deposition of PDDA and hydroxides or oxides is observed, which means that potential interactions are critical for the success of deposition and suspension stability.

Polymer-metal ion complexes, with metal ions attached to the polymer ligand by a coordinate bond, can also give rise to the fabrication of novel nanocomposites through EPD⁹². These complexes can be obtained by

adding additional metal salts to a polymer solution. It was found that EPD of polymer-metal ion complexes can be achieved.

2.5 Applications of EPD

Emerging as a high versatility and cost-effective technique, EPD has been utilized for fabricating a wide range of nanoparticles and nanocomposites for applications in different fields, such as biomedical field^{93,94}, solid oxide fuel cells^{27,95-97}, supercapacitors^{31,38,98,99} and nanoarchitectures^{19,100,101}.

EPD has been widely selected in the production of biocompatible coatings for the biomedical implants and devices. Traditional metallic biomaterials like stainless steel, titanium alloys, magnesium alloys and cobalt-chromium alloys are generally chosen for the orthopedic implants¹⁰². However, the potential corrosion problem can increase the possibility of releasing toxic metallic ions and particles¹⁰³. To solve this problem, Razavi¹⁰³ developed nanostructured merwinite bioceramic coating on Mg alloy via EPD to improve its corrosion resistance and enhance the biocompatibility of the Mg alloy. In another investigation, Pang¹⁰⁴ successfully deposited hydroxyapatite (HA)-chitosan coating on stainless steel with EPD and confirmed that the resulting coating effectively provides corrosion protection of the stainless steel substrate. It

was also inferred that chitosan can dramatically promote the EPD of HA particles and avoid the process of high-temperature sintering.

Solid oxide fuel cell (SOFC) is a power generation device, allowing for the clean production of electricity from a fuel¹⁰⁵. It was documented that the ability to produce fully dense electrolyte layers is considered as the key factor in choosing a manufacturing technique. EPD, as a colloidal process, can efficiently meet the requirement of forming uniform and dense electrolyte layers. Besides, EPD can provide porous coating for electrodes and optimize the fabrication process of SOFC stacks with complicated design¹⁰⁶. Yttria stabilized zirconia (YSZ) is a typical electrolyte material used for SOFC¹⁰⁷. Jia et al.¹⁰⁸ obtained relatively dense YSZ film with little pores through EPD and applied it in the SOFC fabrications. Talebi¹⁰⁹ also got a crack-free thick dense YSZ film on a porous NiO-YSZ substrate by EPD. In a discovery by Zhitomirsky and Petric⁵⁴, a ethyl alcohol-phosphate ester-polyvinyl butyral system is proposed as an ideal solvent-dispersant-binder system for the EPD of ceramic materials that used in the formation of SOFC. This system can not only provide good dispersion of ceramic particles but also prevent cracking of the deposits.

Electrochemical supercapacitor is a unique energy storage device, providing a large amount of energy in a short period of time. Conducting polymers¹¹⁰, graphene¹¹¹ and multiwalled carbon nanotubes

(MWCNT)^{38,112,113} have been usually chosen as the base materials for the fabrication of supercapacitor electrodes and EPD was always employed as a technique to deposit corresponding films for supercapacitors. Du and Pan¹¹⁴ fabricated MWCNT thin films by EPD and found that supercapacitor built by this thin film shows a high specific power density and excellent frequency response. Based on its superior performance, MWCNT thin film prepared by EPD paves the way for the manufacturing of batteries and other energy storage devices.

With the increasing needs of developing different nanometer-sized electronic and photonic devices, EPD is introduced in the deposition of nanorods^{100,115} and nanowires^{101,116}. As an appropriate material used for optoelectronic applications, ZnO nanorods are always prepared by chemical vapor deposition¹¹⁷ and thermal evaporation¹¹⁸ in high temperature. Alternatively, Chen¹¹⁹ received ZnO nanorods with high internal quantum efficiency by EPD at a low temperature. High density and well-aligned nanowires are favored in the electronic applications. The crystalline structures can determine their potential applications and polycrystalline nanowires are preferred in photovoltaics. Polycrystalline Te nanowires can be deposited by EPD without complex apparatus or thermal treatment¹²⁰.

3. Objective

In order to develop advanced organic-inorganic nanocomposites, my research mainly involves:

- 1) Development of advanced techniques for agglomerate-free synthesis of metal hydroxides and metal oxides particles.
- 2) Development of particle extraction through liquid-liquid interface (PELLI).
- 3) Development of new methods for polymers deposition.
- 4) Co-deposition of polymers and inorganic materials and testing of flame retardant composites.

4. Experimental Methodologies

4.1 Starting Materials

Table 4-1 Materials purchased from commercial suppliers

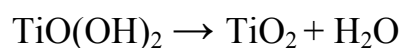
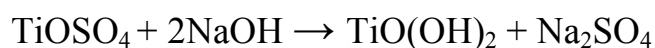
Category	Material	Supplier
Sulfate	TiOSO ₄	Sigma Aldrich
	Al ₂ (SO ₄) ₃	Sigma Aldrich
Dispersing agent	Lauryl gallate (LG)	Sigma Aldrich
	Hexadecyl phosphonic acid (HDPA)	Sigma Aldrich
	3,4-dihydroxybenzaldehyde	Sigma Aldrich
	2,3,4-trihydroxybenzaldehyde	Sigma Aldrich
	1-hexadecylamine	Sigma Aldrich
Film forming agent	Hydroxyethyl cellulose ethoxylate, quaternized (QHECE)	Sigma Aldrich
	Carboxymethyl cellulose sodium salt (CMC-Na)	Sigma Aldrich
	Linear polyethylenimine (PEI)	Sigma Aldrich
	NaOH	Sigma Aldrich

Alkali	$\text{NH}_3 \cdot \text{H}_2\text{O}$	Sigma Aldrich
Other chemicals	Ethanol	Sigma Aldrich
	N-butanol	Sigma Aldrich
Minerals	Mg_2Al double hydroxide (MgAlLDH)	Sigma Aldrich
	Titania	Sigma Aldrich
	$\text{Al}_2\text{Si}_2\text{O}_5(\text{OH})_4$ (Halloysite)	Sigma Aldrich

4.2 Synthesis of TiO_2 and $\text{Al}(\text{OH})_3$

(i) Synthesis of TiO_2 particles at room temperature

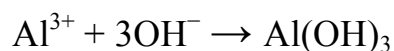
The synthesis of TiO_2 was performed using aqueous TiOSO_4 solutions. The pH of the solutions was adjusted to pH=6 by NaOH. The precipitates were washed with water and dried in air. The reactions follow the equations below¹²¹,



(ii) Synthesis of $\text{Al}(\text{OH})_3$ particles at room temperature

The synthesis of $\text{Al}(\text{OH})_3$ was achieved using $\text{Al}_2(\text{SO}_4)_3$ aqueous solutions. The pH of the solution was adjusted to pH=9 by addition of $\text{NH}_3 \cdot \text{H}_2\text{O}$. Stirring was performed during 3 h. The obtained precipitate

was washed with water and dried in air. The preparation of Al(OH)_3 follows to the reaction,



4.3 EPD

EPD was performed using a cell, containing a stainless steel (304 type, 0.1×30×50 mm) substrate and a platinum (0.1×30×50 mm) counter electrode. The distance between the electrodes was 15mm. The electrode holder was connected to a constant voltage power source. The volume of deposition bath was 300ml. The electrode holder was then submerged in to the suspension.

4.4 Characterization techniques

4.4.1 X-ray diffraction analysis

X-ray diffraction (XRD) investigations were performed using a powder diffraction meter (Nicolet I2, monochromatized $\text{CuK}\alpha$ radiation).

The composition of materials was analyzed by XRD. The precipitated materials were filtrated, washed with water and ethanol, and then dried in air for 72 h.

4.4.2 Fourier transform infrared spectroscopy

Fourier transform infrared spectroscopy (FTIR) studies were performed on a Bruker Vertex 70 spectrometer. For the preparation of samples for the FTIR studies, the suspensions were filtrated and the obtained materials were dried in air.

4.4.3 Scanning electron microscope

Electron microscopy investigations were performed using a JEOL JSM-7000F scanning electron microscope (SEM). The samples for SEM were dried for 72 h before the studies.

4.4.4 Thermogravimetric and differential thermal analysis

The thermogravimetric analysis (TGA) and differential thermal analysis (DTA) were performed using a NETZSCH STA-409 thermoanalyser in air at a heating rate of 5 °C/min. The samples for TGA and DTA were scraped off the electrodes and dried in air for 72 h before the studies.

4.4.5 Deposition yield study

The quartz crystal microbalance (QCM) method was used for the in-situ investigation of deposition yield. The mass Δm of deposited material was calculated using Sauerbrey's equation:

$$-\Delta F = \frac{2F_0^2}{A\sqrt{\mu_q\rho_q}} \times \Delta m$$

where ΔF is frequency decrease of the QCM, F_0 is the parent frequency of QCM (9 MHz), A is the area of gold electrode (0.2 cm^2), μ_q is the shear modulus of quartz, ρ_q is the density of quartz. The deposition yield is calculated as a difference of substrate mass before deposition and after deposition and drying for 72 h in air.

4.4.6 Particle size distribution analysis

Dynamic light scattering (DLS, DelsaMax Pro: Beckman Coulter) was used for the particle distribution analysis. The suspensions of particles in n-butanol, separated from the aqueous phase, were diluted with ethanol for the particle distribution analysis.

5. Results and discussion

5.1 Agglomeration of synthesized inorganic particles

In most cases, we use wet chemical precipitation method for the synthesis of inorganic particles in aqueous solutions. After filtering, washing and drying, the obtained particles must be re-dispersed into an organic solvent, which contains water insoluble polymers and binders for further fabrication of devices. However, the drying process always results in the agglomeration of particles, which is detrimental for the fabrication of inorganic/organic nanocomposites through EPD. The agglomeration of $\text{Al}(\text{OH})_3$ is shown in Fig.5-1. The agglomeration of primary $\text{Al}(\text{OH})_3$ particles result in relatively large agglomerates with a size above $10\ \mu\text{m}$.

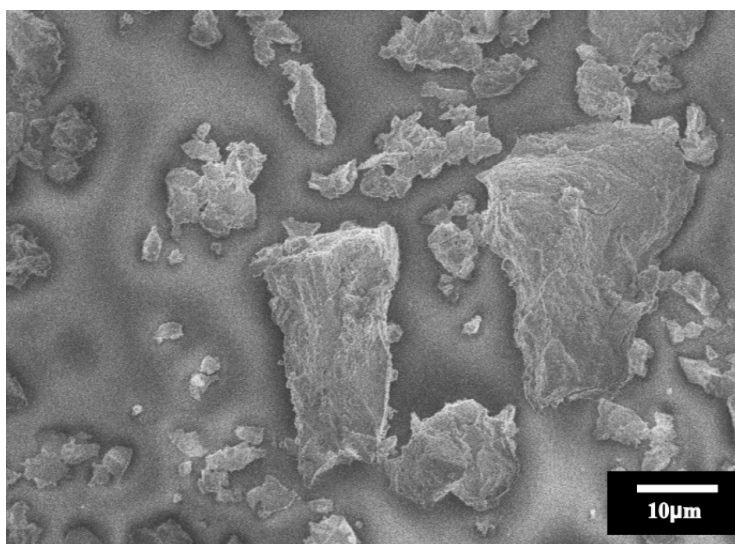


Figure. 5-1. SEM image of $\text{Al}(\text{OH})_3$ powder.

There are two driving forces for the agglomeration, the reduction of

surface area and condensation reactions between surface OH groups.

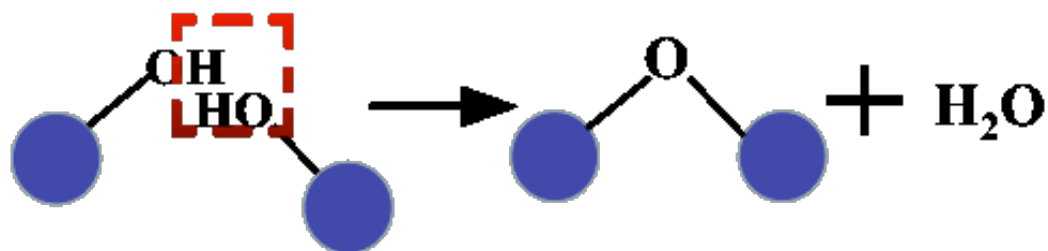


Figure. 5-2. condensation reaction between surface OH groups

An effective method to solve the agglomeration problem is to extract synthesized particles from an aqueous phase into organic phase directly to avoid the drying process. This kind of extraction method is called liquid-liquid extraction. The two-step mechanism of liquid-liquid extraction is based on surface modification of inorganic particles in an aqueous phase followed by a second modification at water-n-butanol interface and subsequent particle extraction through the liquid-liquid interface. In the one-step extraction mechanism, the particles are modified at the liquid-liquid interface and then extracted from one liquid to another.

5.2 Liquid-liquid extraction and cathodic EPD of cationic cellulose- Al(OH)₃ composites

5.2.1 Two-step liquid-liquid extraction

In order to extract synthesized particles efficiently, we used two-step liquid-liquid extraction which involves surface modification of Al(OH)₃

in an aqueous phase followed by a second modification at water-n-butanol interface and subsequent particle extraction through the liquid-liquid interface (Fig.5-3). The synthesis of $\text{Al}(\text{OH})_3$ in solutions, containing aldehyde molecules R-CHO , resulted in the R-CHO adsorption on the particle surface. In the next step, these particles are modified at the liquid-liquid interface by a chemical interaction between adsorbed R-CHO and fatty amine extractor molecule NH_2L , dissolved in n-butanol. This reaction allows for the consequent particle extraction to the n-butanol phase.

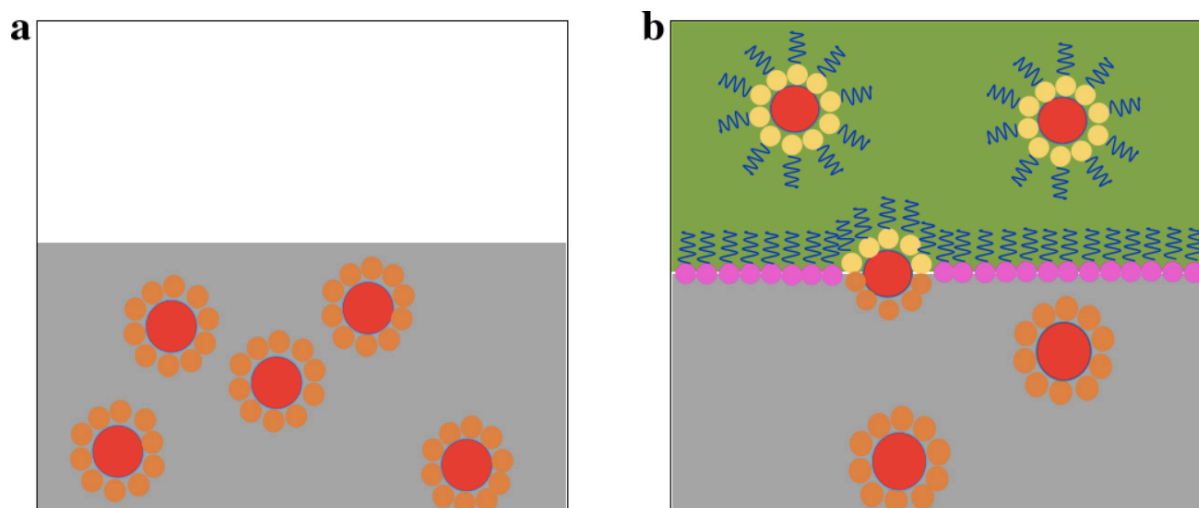
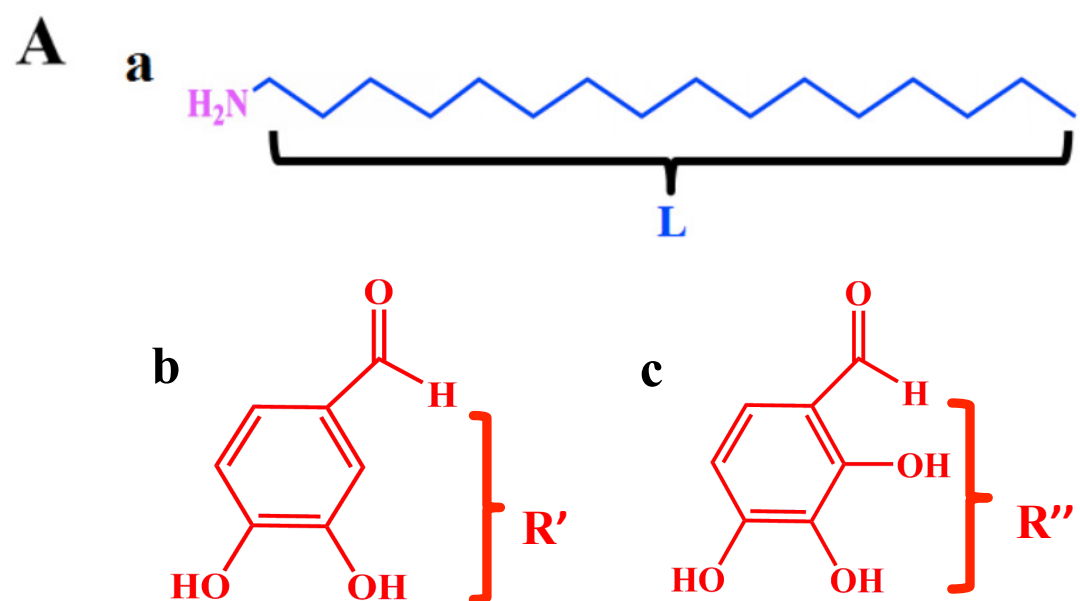


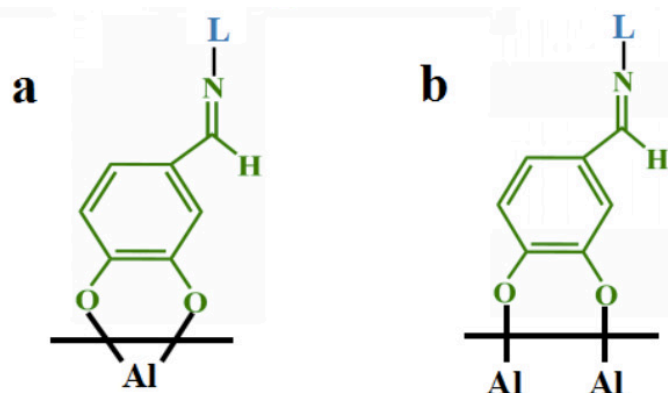
Figure. 5-3. Schematic of synthesis and extraction process, involving (a) modification of $\text{Al}(\text{OH})_3$ particles with R-CHO during synthesis in an aqueous phase and (b) particle extraction to n-butanol phase involving a Schiff base reaction of R-COH and NH_2L

The details of two-step extraction strategy are shown in Fig. 5-4. The chemical structure of the extractor, 1-hexadecylamine (HDA), can be seen in Fig. 5-4 A (a). This NH_2L structure includes a hydrophobic hydrocarbon chain and hydrophilic NH_2 groups. NH_2L is a head-tail type

surfactant, which is insoluble in water, but soluble in n-butanol. The chemical structures of aldehyde molecules, 3,4-dihydroxybenzaldehyde (DBA) and 2,3,4-trihydroxybenzaldehyde (TBA), can be found in Fig. 5-4A(b,c). They both have R-CHO structure which belongs to catechol or gallic acid families of materials.



(R= R' or R'')



C

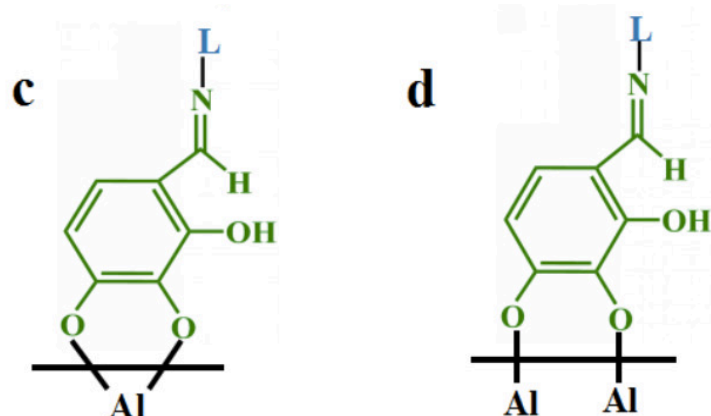
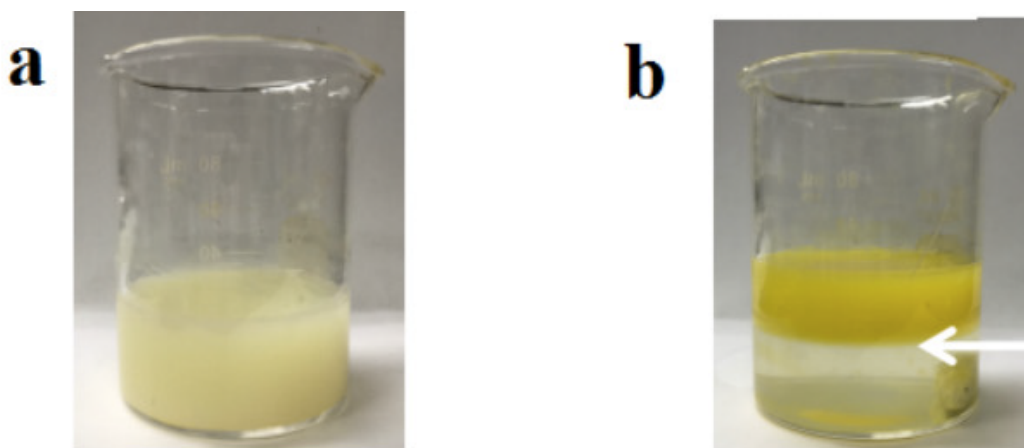


Figure. 5-4. (A) Chemical structure of (a) NH_2L , (b) $\text{R}'\text{-CHO}$ and (c) $\text{R}''\text{-CHO}$, (B) Schiff base reaction of R-CHO ($\text{R}=\text{R}'$ or R'') and NH_2L , (C) adsorption of (a,b) $\text{R}'\text{-CNH-L}$ and (c,d) $\text{R}''\text{-CNH-L}$ on $\text{Al}(\text{OH})_3$, involving (a,c) chelation and (b,d) bridging of Al atoms.

The phenolic OH groups of DBA and TBA can form strong chelating or bridging bond to the metal atoms on the material surface. The aldehyde groups of $\text{R}'\text{-CHO}$ and $\text{R}''\text{-CHO}$ can have Schiff base reaction (Fig. 5-4. B) with NH_2L at the liquid-liquid interface, which links the NH_2L extractors molecules to the modified particles and allows for the extraction. NH_2L accumulates at the liquid-liquid interface with the hydrophilic groups exposed to water and hydrophobic tail extended out of the water phase into the n-butanol phase. The accumulation and orientation of the NH_2L molecules at the liquid-liquid interface can promote their interaction with aldehyde groups of $\text{R}'\text{-CHO}$ and $\text{R}''\text{-CHO}$ (Fig.5-4 C), forming (a,c) chelation and (b,d) bridging of Al atoms on the particle surface.

5.2.2 Experimental results of liquid-liquid extraction

The images of the suspensions before and after extraction are shown in Fig. 5-5. The adsorption of R'-CHO and R''-CHO during Al(OH)₃ synthesis and Al(OH)₃ extraction to the n-butanol phase resulted in color change of the Al(OH)₃ particles. It is worth to note that NH₂L adsorption on unmodified particles was weak and could not result in extraction. Thus, the modification of the Al(OH)₃ particles with R'-CHO or R''-CHO is an important step in the extraction method. Besides, Al(OH)₃ particles modified with R'-CHO or R''-CHO remained in the aqueous phase after addition of n-butanol without NH₂L. The extraction can only be observed after addition of NH₂L to the n-butanol phase.



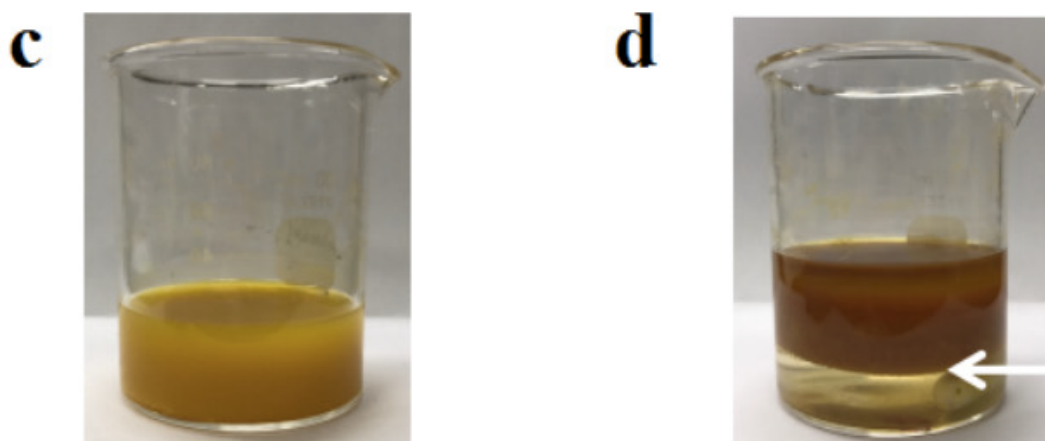


Figure. 5-5. Particle extraction involving (a,b) R' -CNH-L and (c,d) R'' -CNH-L, arrows show liquid-liquid interface.

To investigate the influence of extractors, we used DLS to examine the particle size distribution of extracted particles. The results (Fig. 5-6) showed that the typical radii of $Al(OH)_3$, modified with R' -CHO and R'' -CHO were below 100 and 130 nm, respectively. In comparison with the size of agglomerates (Fig. 5-1), the size of the extracted particles was significantly smaller.

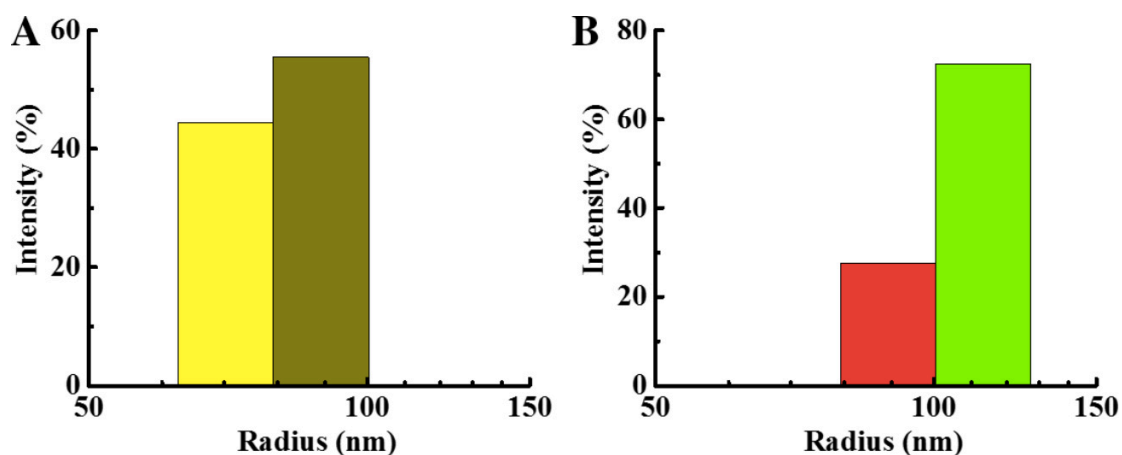


Figure. 5-6. Particle size distribution for $Al(OH)_3$ particles, extracted to n-butanol using (A) R' -CNH-L and (B) R'' -CNH-L.

The suggested modification and extraction mechanism was confirmed by

the results of FTIR studies. Fig. 5-7(a,b) shows FTIR spectra of R'-CHO and NH₂L. The adsorptions at 1649, 1593, 1537 and 1436 cm⁻¹ in the spectrum of R'-CHO (Fig. 5-7a) were ascribed to the aromatic C-C/C=C vibrations and the adsorption at 1294 cm⁻¹ was related to C-O stretching vibrations. Similar adsorptions were observed in the spectra of Al(OH)₃, synthesized in presence of R'-CHO (Fig. 5-7c). Based on this, it is clear that R'-CHO adsorbed on the Al(OH)₃ particles. The peaks at 2918 and 2850 cm⁻¹ in the spectrum of NH₂L (Fig. 5-7b) are resulted from stretching vibrations of CH₂ and CH₃ groups and similar peaks were observed in the spectrum of Al(OH)₃ particles, extracted to the n-butanol phase (Fig. 5-7d). Similar results were obtained for R''-CHO and extracted material. In Fig. 5-8.a, the adsorptions at 1643, 1614, 1504 and 1442 cm⁻¹ are ascribed to the C-C/C=C vibrations. The adsorption at 1278 cm⁻¹

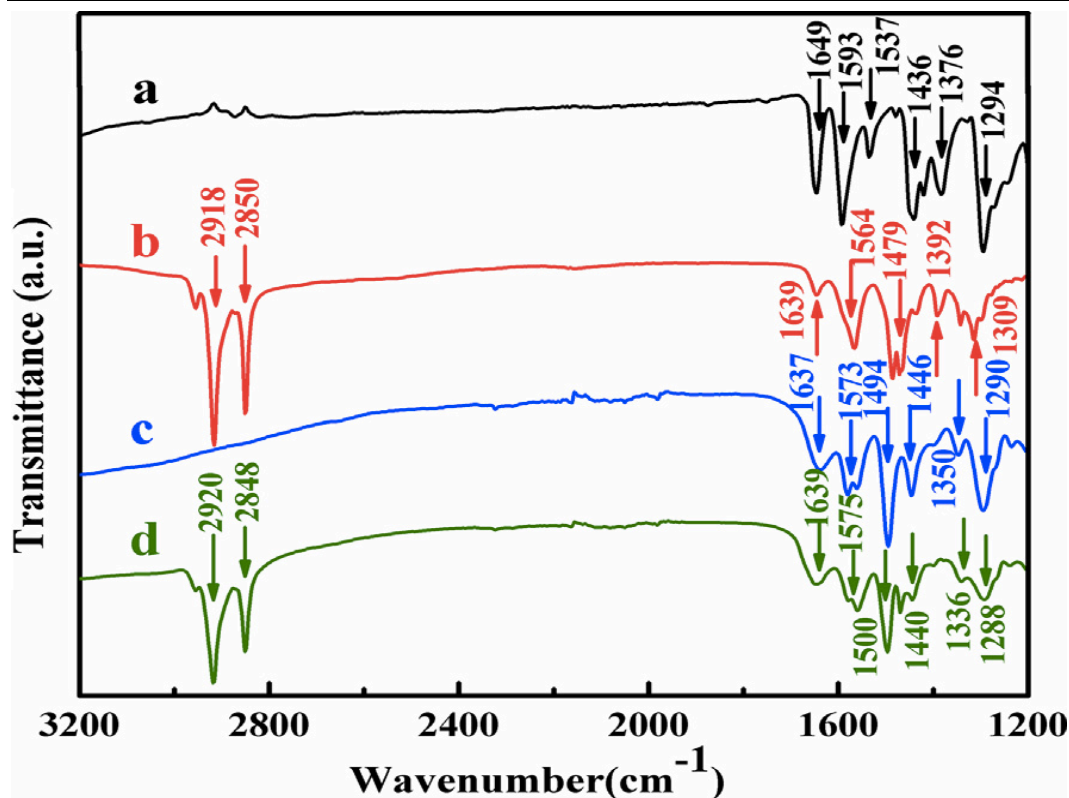


Figure. 5-7. FTIR spectra of (a) R'-CHO, (b) NH₂L, (c) Al(OH)₃ particles synthesized in the presence of R'-CHO, (d) Al(OH)₃ particles, extracted using R'-CNH-L.

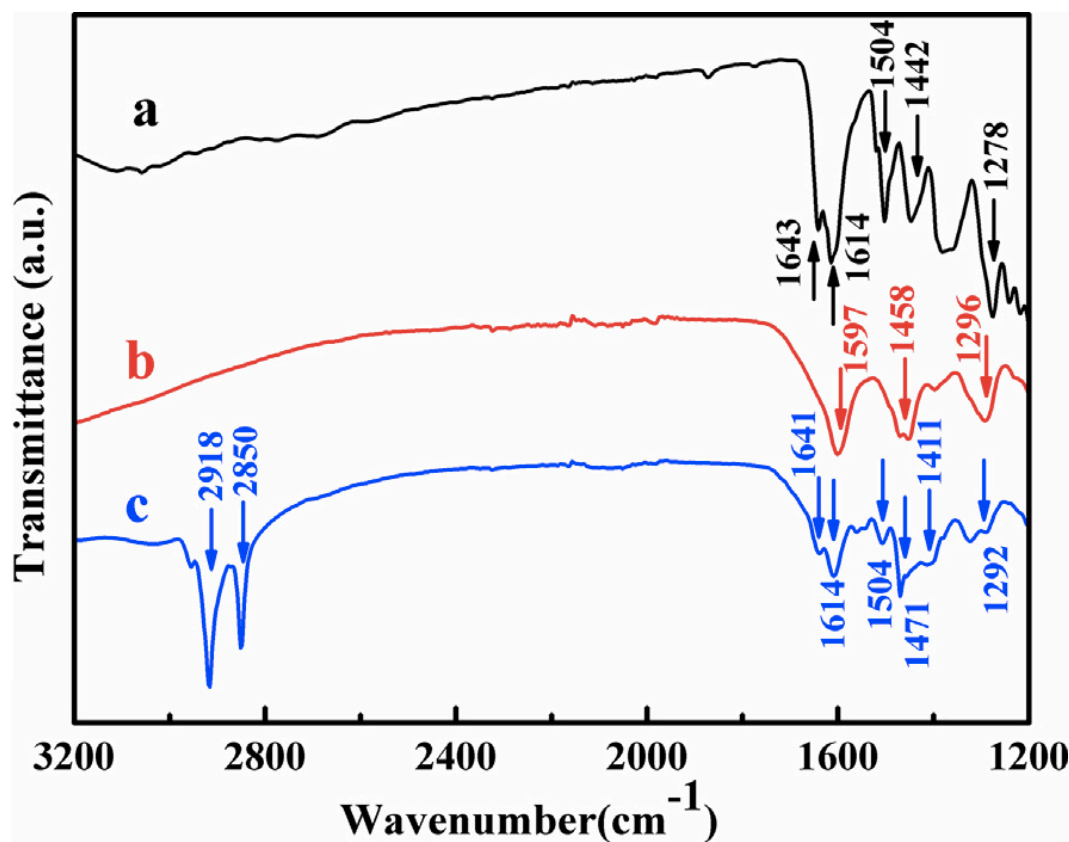


Figure. 5-8. FTIR spectra of (a) R''-CHO, (b) Al(OH)₃ particles synthesized in the presence of R''-CHO, (c) Al(OH)₃ particles, extracted using R''-CNH-L.

is assigned to C-O stretching vibrations. Similar adsorptions were observed in the spectrum of $\text{Al}(\text{OH})_3$ particles, prepared in the presence of $\text{R}''\text{-CHO}$ (Fig. 5-8.b). The adsorption of $\text{R}''\text{-CHO}$ on $\text{Al}(\text{OH})_3$ leads to peak broadening. The extracted material showed additional peaks at 2918 and 2850 attributed to vibrations of CH_2 and CH_3 groups of NH_2L . Therefore, the FTIR data provide evidence for two-step extraction mechanism including the adsorption of R-CHO ($\text{R}=\text{R}'$ or R'') on $\text{Al}(\text{OH})_3$ during synthesis and further modification and also interactions between R-CHO and NH_2L in the Schiff base reaction .

5.2.3 Structure and properties of QHECE

As the most abundant natural polymer resource, cellulose has gained much attention recently. With various advantages, such as biodegradable, low-cost and non-toxic, cellulose and its derivatives have been extensively introduced into the development of drug delivery¹²², energy storage devices¹²³, food package¹²⁴ and also wastes treatment¹²⁵. Moreover, cellulose was always involved in the fabrication of functional nanocomposites with a variety of inorganic nanoparticles^{126,127}. According to the safety regulations, many polymer products must include inorganic flame retardant additive to enhance their flame retardant properties. As a typical flame retardant hydroxide, $\text{Al}(\text{OH})_3$ has been

chosen as a good flame retardant additive for cellulose. The flame retardant properties of such additives are related to their dehydration reaction and potential endothermic effects.

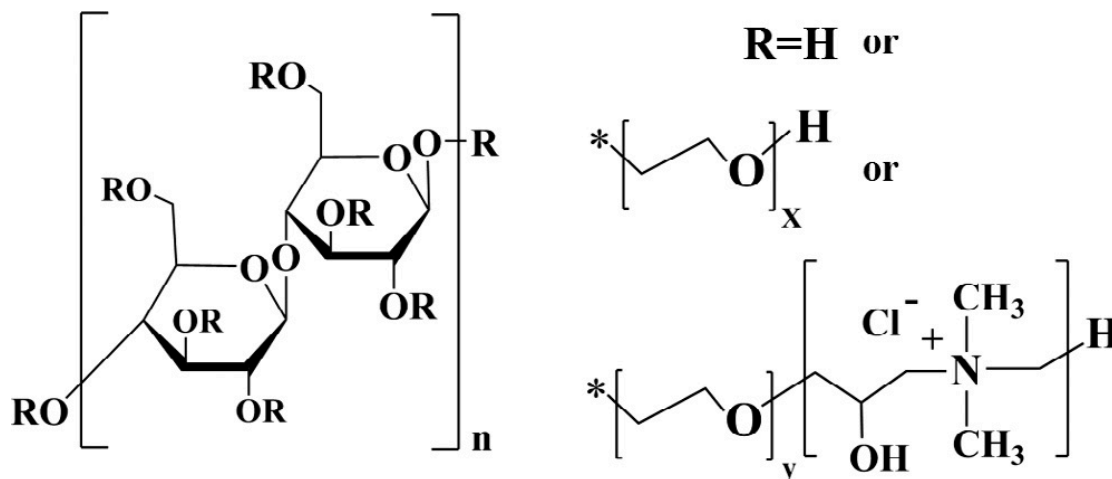


Fig. 5-9. Chemical structure of QHECE

QHECE is a strong cationic polyelectrolyte, which has been utilized for the fabrication of gels and films in combination with some anionic polyelectrolytes¹²⁸. The cationic properties of QHECE are related to the N⁺(CH₃)₃ groups(Fig.5-9). The multiple hydroxyl groups of QHECE impart binding properties that play an essential role in the formation of films. QHECE is also a highly water-soluble copolymer with high OH⁻ conductivity. Based on these, QHECE is a promising film forming and charging agent for cathodic EPD.

5.2.4 Experimental results of cathodic EPD

It was found that QHECE films could be deposited by cathodic EPD. The EPD mechanism involved QHECE cataphoresis, accumulation of

QHECE at the electrode surface and formation of thin gel layers. After drying in air, uniform and adherent QHECE films were obtained. The use of mixed water-ethanol solvent allowed for low film porosity, because of the reduced gas evolution at the electrode surface.

We used QCM to analyze the deposition yield during the deposition process from dilute solutions. The deposit mass rises nearly linearly as deposition time increases at a constant voltage, indicating the continuous film growth (Fig. 5-10). The deposition yield also increased with increasing QHECE concentration (Fig. 5-11) in agreement with the Hamaker equation (2-6).

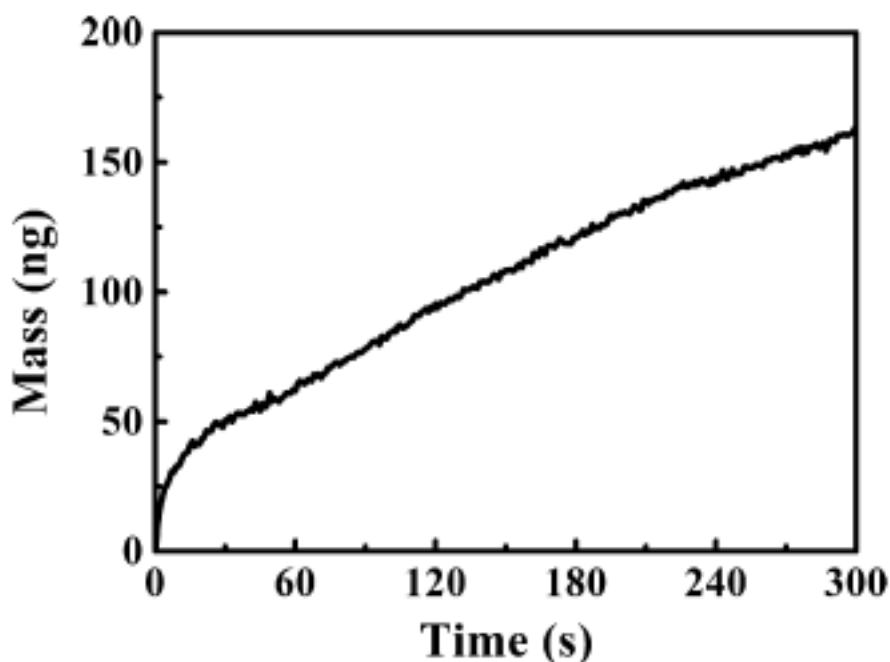


Figure. 5-10. Time dependence of QCM mass gain for deposition from 0.05 g/L QHECE solution at a cell voltage of 5V

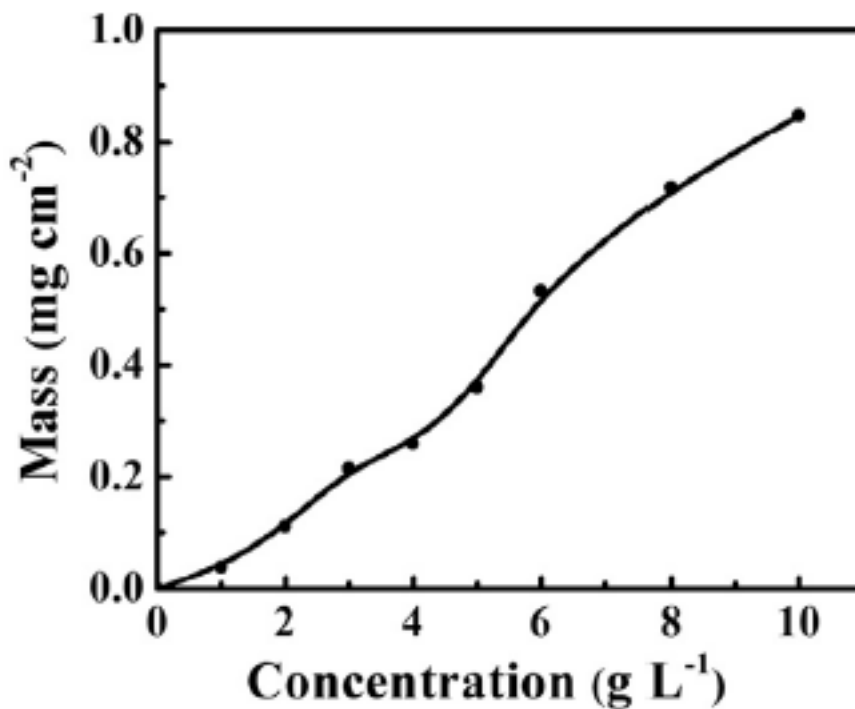


Figure. 5-11. Deposit mass versus QHECE concentration in solutions at a voltage of 30 V and a deposition time of 5 min. The deposit mass data represents average values for 3 experiments with error < 4%

Before EPD, we did sedimentation test for both synthesized $\text{Al}(\text{OH})_3$ with drying process and $\text{Al}(\text{OH})_3$ with extraction. It is obvious that the suspension of extracted $\text{Al}(\text{OH})_3$ showed improved stability while the one with drying process showed rapid sedimentation after ultrasonic agitation due to the relatively large particle size of $\text{Al}(\text{OH})_3$. Moreover, with the smaller particle size, the suspension with extracted $\text{Al}(\text{OH})_3$ were found to be stable for two weeks.

After EPD of film from the stable suspension with extracted $\text{Al}(\text{OH})_3$ and QHECE, we did SEM test for the resulting film (Fig. 5-13). The film was smooth and uniform without agglomerated particles.



Figure. 5-12. Sedimentation test for $\text{Al}(\text{OH})_3$, prepared by (a) precipitation and drying and (b) precipitation and extraction. The suspensions contained 2g/L $\text{Al}(\text{OH})_3$ and 1g/L QHECE in a mixed water-alcohol solvent

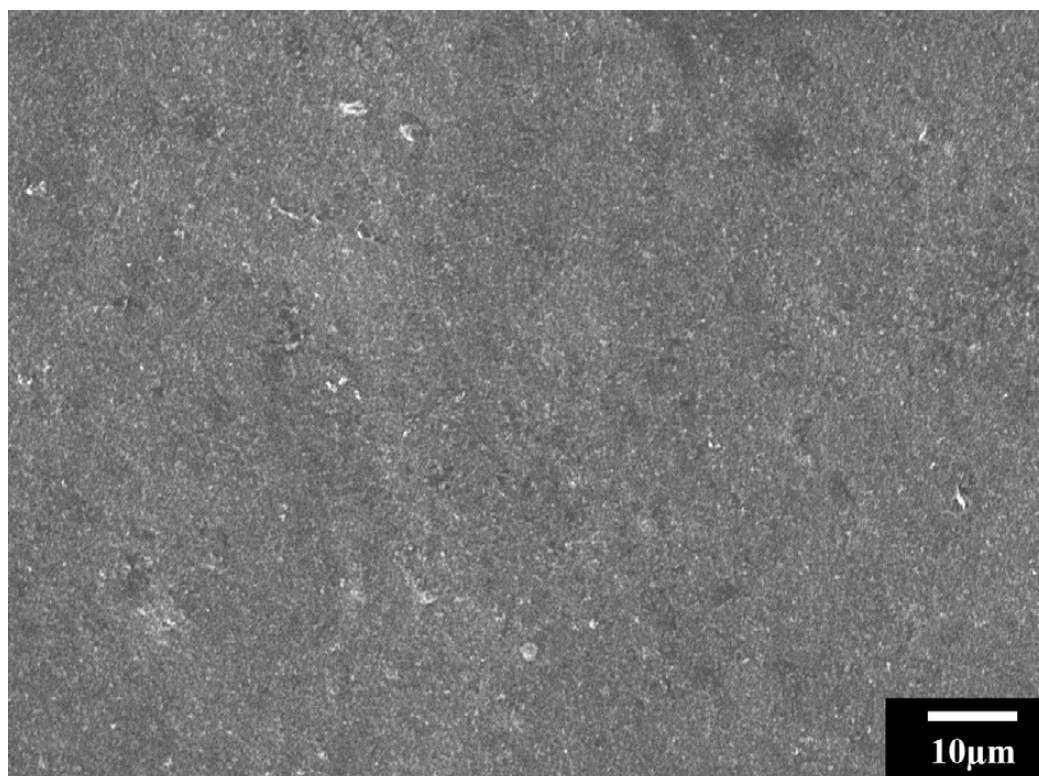


Figure. 5-13. SEM image of a composite prepared by EPD 2g/L $\text{Al}(\text{OH})_3$ and 1g/L QHECE in a mixed water-alcohol solvent

The incorporation of flame retardant $\text{Al}(\text{OH})_3$ into the composite films was confirmed by the TGA and DTA analyses. We collected and compared the TGA and DTA data for pure $\text{Al}(\text{OH})_3$, pure QHECE and QHECE- $\text{Al}(\text{OH})_3$ composite, prepared by EPD. A mass loss was shown in the TGA curve of $\text{Al}(\text{OH})_3$, which is attributed to the dehydration. In the given temperature range, the mass reduction was observed mainly below 250 °C and the total mass loss at 800 °C was about 40% (Fig.5-14.a). Importantly, the theoretical mass loss of $\text{Al}(\text{OH})_3$ is 35% which is caused by the decomposition of $\text{Al}(\text{OH})_3$ and its conversion to Al_2O_3 . Additional mass loss was related to the adsorbed water. The broad endothermic peak centered on 130 °C was caused by dehydration (Fig.5-14.b). Based on above, the flame retardant properties of $\text{Al}(\text{OH})_3$ are related to the water release (TGA data) and endothermic effect (DTA data).

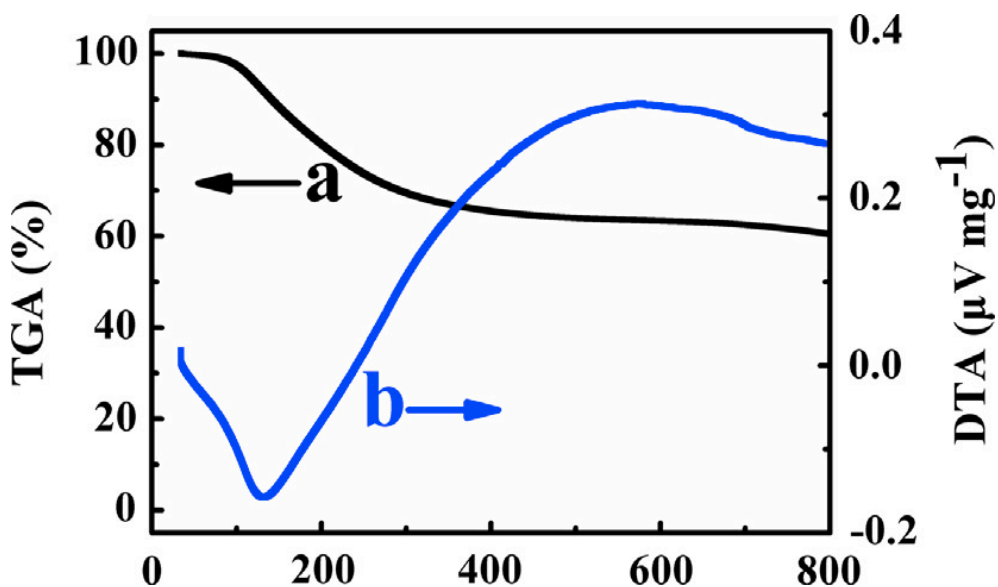


Figure. 5-14. TGA (a) and DTA (b) data for as prepared $\text{Al}(\text{OH})_3$, the total mass loss at 800 °C was 40%

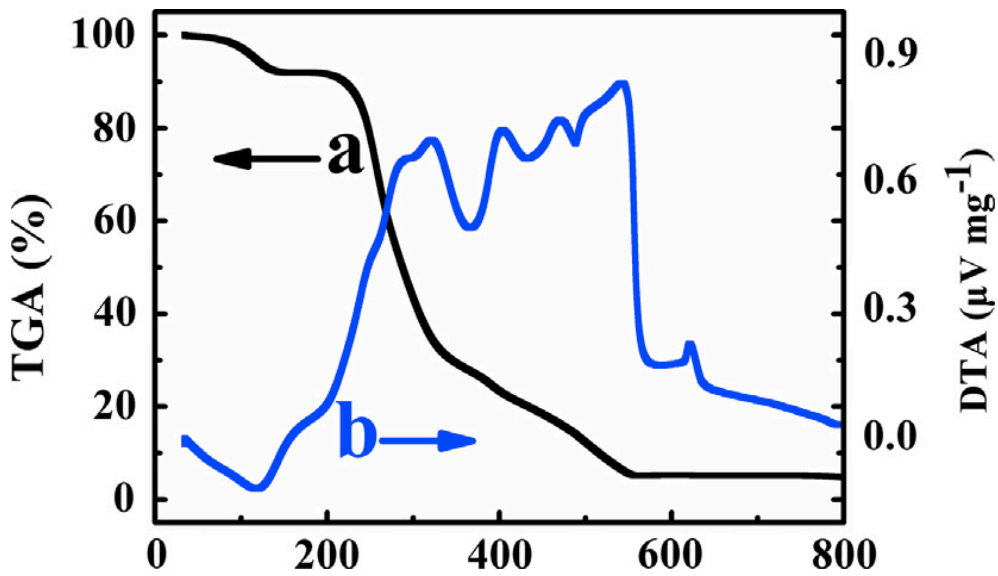


Figure. 5-15. TGA (a) and DTA (b) data for as-received QHECE, the mass loss at 200 and 800 °C was 9 and 95%, respectively

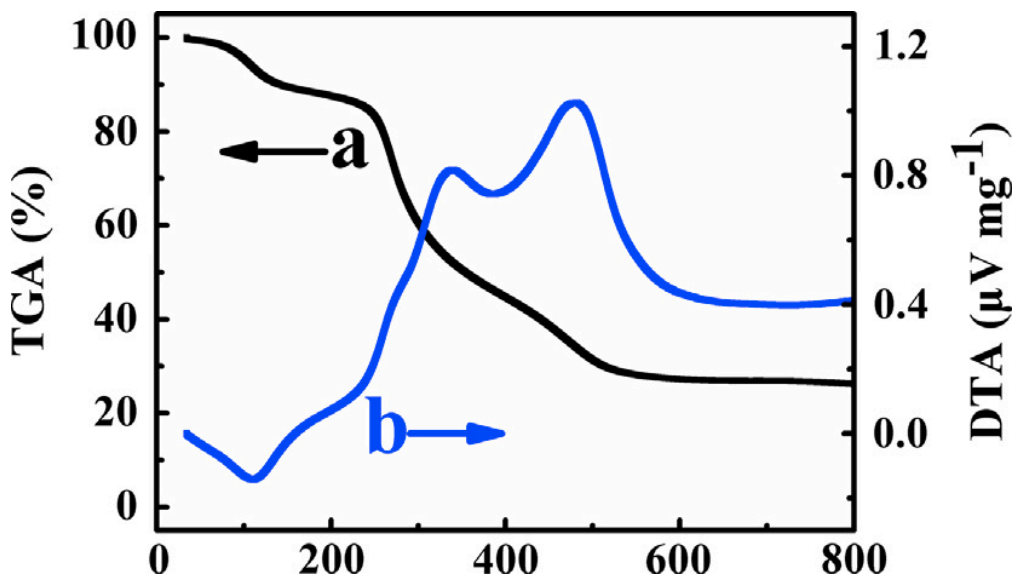


Figure. 5-16. TGA (a) and DTA (b) data for QHECE- $\text{Al}(\text{OH})_3$ composite, prepared by EPD from 2g/L $\text{Al}(\text{OH})_3$ and 1g/L QHECE suspensions in a mixed water-alcohol solvent, the mass loss at 200 and 800 °C was 13 and 73%, respectively

QHECE showed several steps in mass loss of its TGA curve (Fig.5-15.a).

The mass loss at 120 °C and corresponding endothermic effect in the

DTA data are ascribed to the removal of adsorbed water. Additional mass

loss resulted from burning out of QHECE was observed in the range of 330-550 °C. The DTA data showed exothermic effects in the same temperature range (Fig.5-15.b). The broad exothermic peak was attributed to burning out of QHECE.

The QHECE- $\text{Al}(\text{OH})_3$ composite, prepared by EPD showed several steps in mass loss in its TGA curve (Fig.5-16.a). This mass loss is related to dehydration of individual components of the composite and burning out of QHECE. The broad endothermic peak at proximately 120 °C was related to dehydration and exothermic effects at higher temperature were caused by burning out of QHECE. The sample left 27% of the initial sample mass at 800 °C and the residual material was Al_2O_3 . Combining with the TGA data for $\text{Al}(\text{OH})_3$ (Fig.5-14.a), the $\text{Al}(\text{OH})_3$ content in the composite (Fig.5-16.a) was found to be 45%.

5.2.5. Conclusion

The results of our investigations indicate that two-step liquid-liquid extraction is an effective method for the fabrication of non-agglomerated particles with reduced size, which allows for the further formation of uniform composite film. This two-step extraction method modified the particles during their synthesis and then used Schiff base reaction to extract them. This process can reduce the particle size and improve the

stability of the suspension for EPD. EPD method has been developed for the cathodic deposition of QHECE films. The deposition yield can be varied with the variation of deposition time and QHECE concentration. QHECE was found to be a good charging and film firming agent for EPD of $\text{Al}(\text{OH})_3$. Therefore, QHECE was used for the fabrication of composite films containing flame retardant $\text{Al}(\text{OH})_3$. The incorporation of flame retardant $\text{Al}(\text{OH})_3$ particles into the QHECE was confirmed by TGA and DTA studies. Further development of two-step liquid-liquid extraction method can be exploited for the fabrication of advanced QHECE composites, containing various functional inorganic materials.

5.3 Liquid-liquid extraction and anodic EPD

5.3.1 One-step liquid-liquid extraction

In addition to two-step liquid-liquid extraction, we also used one-step liquid-liquid extraction to extract $\text{Al}(\text{OH})_3$. Different from two-step liquid-liquid extraction, the mechanism of one-step liquid-liquid extraction is simpler, which is based on the adsorption of extractors. Such one-step liquid-liquid extraction procedure can effectively avoid the formation of stoichiometric complexes with the amine extractor at the liquid-liquid interface, which is potentially existed in the process of two-step liquid-liquid extraction. LG and HDPA are selected as the

extractors for the one-step liquid-liquid extraction. As Fig.5-17.A shows, LG includes a hydrophilic galloyl group and a hydrophobic hydrocarbon group. The galloyl group contains three phenolic OH groups, which shows strong adsorption on particles by forming chelating(Fig.5-17Ba) or bridging bonds(Fig.5-17Bb) with metal atoms. Performed as an advanced extractor, HDPA (Fig.5-17.C) contains a phosphonate group exhibiting strong adsorption on various inorganic particles. The oxygen atoms of the phosphonate ligand can form bi-or tridentate bonding with metal atoms(Fig.5-17.D).

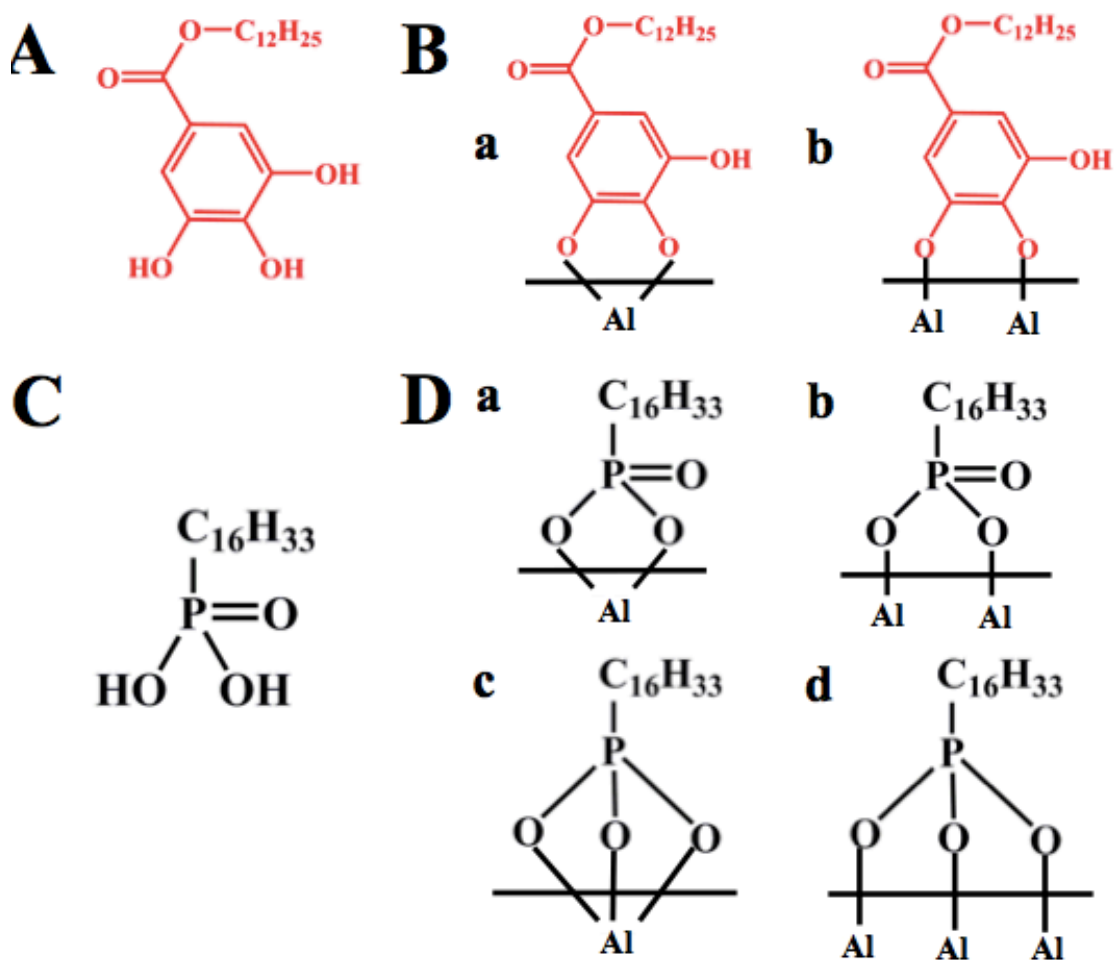


Figure. 5-17. Chemical structure of (A) LG and (C) HDPA. (B) adsorption mechanisms of LG, involving (a) chelating bidentate bonding and (b) bridging

bidentate bonding. (D) adsorption mechanisms of HDPA, involving (a) chelating bidentate bonding, (b) bridging bidentate bonding, (c) chelating tridentate bonding and (d) bridging tridentate bonding

The mechanism of one-step liquid-liquid extraction is illustrated in Fig.5-18. $\text{Al}(\text{OH})_3$ was prepared in an aqueous phase by the addition of NaOH to the $\text{Al}_2(\text{SO}_4)_3$ solution(Fig.5-18.A) and a solution of LG or HDPA in n-butanol was added. In the A-B1-B2-D mechanism, the extractor molecules accumulated at that water-n-butanol interface(Fig.5-18.B1) with the hydrophilic groups exposed to water and the hydrophobic tails extended out of water phase into the n-butanol phase. The accumulation and orientation of the extractor molecules at the liquid-liquid interface promoted their adsorption on particles(Fig.5-18 B2), which were then transferred to the n-butanol phase(Fig.5-18 D). Both LG and HDPA can extract $\text{Al}(\text{OH})_3$ particles to the n-butanol phase via the A-B1-B2-D mechanism. Different from LG, HDPA can also extract $\text{Al}(\text{OH})_3$ particles to the n-butanol phase via the A-C1-C2-D mechanism due to its solubility in alkaline solutions. During the process, HDPA can potentially penetrate the water-n-butanol interface to form a solution in the aqueous alkaline phase(Fig.5-18.C1) and adsorb on the $\text{Al}(\text{OH})_3$ particles(Fig.5-18.C2). There is a condensation reaction between the PO_3H_2 group of HDPA and the surface OH group of $\text{Al}(\text{OH})_3$ during the adsorption. With stirring, the adsorbed HDPA facilitated the transfer

of $\text{Al}(\text{OH})_3$ particles to n-butanol(Fig.5-18.D).

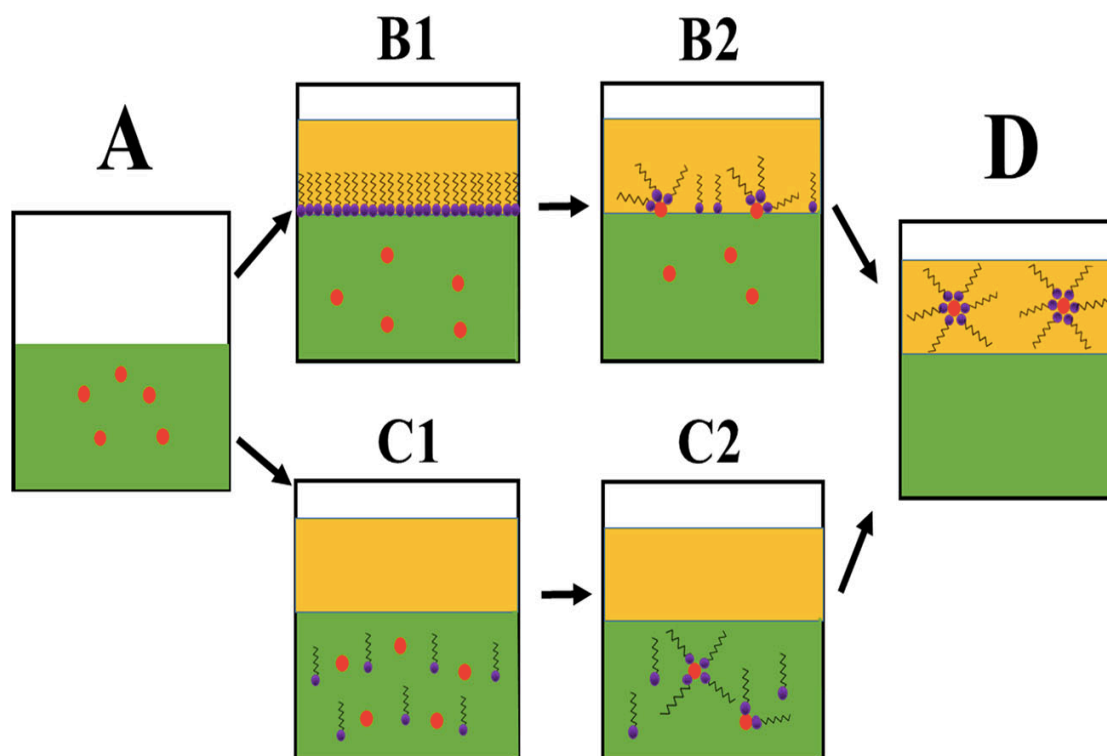


Figure. 5-18. One-step extraction mechanism (A-B1-B2-D and A-C1-C2-D) in extraction method 1: (A) $\text{Al}(\text{OH})_3$ particles precipitate in aqueous solutions, (B1) extractor is accumulated at the liquid-liquid interface and (B2) adsorption occurs at the interface, (C1) extractor is transferred from n-butanol to the aqueous phase, (C2) extractor adsorption occurs in the bulk of the aqueous phase, and (D) $\text{Al}(\text{OH})_3$ particles are transferred to the n-butanol phase

HDPAs can also allow for another extraction procedure like Fig.5-19 shows. The $\text{Al}(\text{OH})_3$ synthesis and extraction involved the mixing of aqueous $\text{Al}_2(\text{SO}_4)_3$ solution(Fig.5-19.a) with aqueous 0.1 M NaOH solution containing dissolved HDPAs. After mixing, HDPAs-modified $\text{Al}(\text{OH})_3$ particles were formed in the aqueous phase(Fig.5-19b). The

addition of n-butanol and stirring can result in the transfer of $\text{Al}(\text{OH})_3$ particles to the n-butanol phase(Fig.5-19c,d). Therefore, HDPA can act as a capping agent for particle synthesis and also an extractor for liquid-liquid extraction.

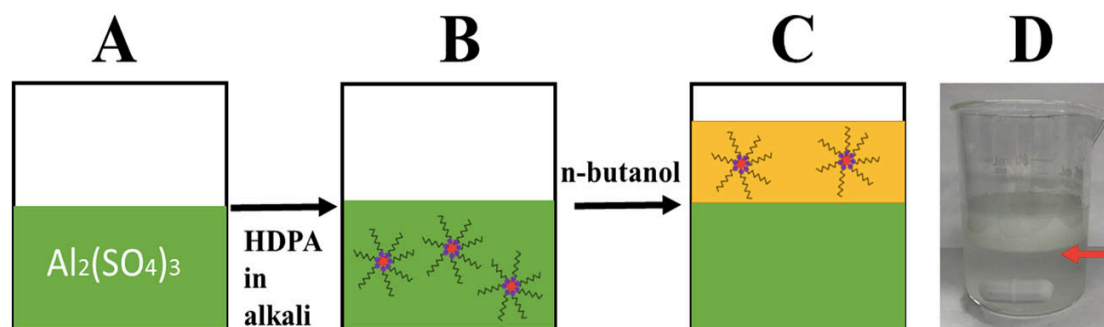


Figure. 5-19. Suggested extraction mechanism for HDPA: A starting $\text{Al}_2(\text{SO}_4)_3$ solution; B formation of particles, containing adsorbed HDPA after addition of HDPA solution in alkali; C extraction of particles to the n-butanol phase; and D image of $\text{Al}(\text{OH})_3$ extraction using HDPA (arrow shows water-n-butanol interface)

5.3.2 Experimental results of liquid-liquid extraction

Compared with as-prepared $\text{Al}(\text{OH})_3$ suspension(Fig.5-20.a), it is clear that the addition of LG(Fig.5-20.b) and HDPA(Fig.5-20.c) solution in n-butanol both resulted in $\text{Al}(\text{OH})_3$ extraction to the n-butanol phase. DLS method was used to analyze the extracted particles. Both LG(Fig.5-20.d) and HDPA(Fig.5-20.e) have relatively narrow particle size distributions. In comparison with HDPA, particles extracted by LG showed a smaller particle size, with typical radius of 50-60nm.

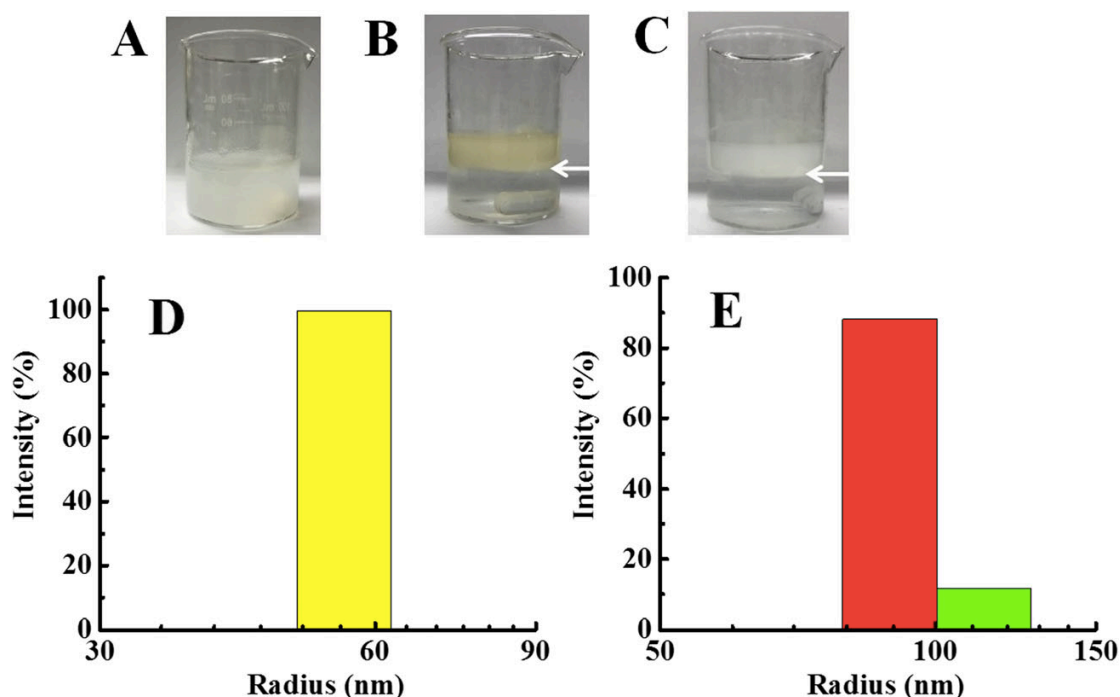


Figure. 5-20. (A). As-precipitated $\text{Al}(\text{OH})_3$, (B). $\text{Al}(\text{OH})_3$ extraction using LG, (C). $\text{Al}(\text{OH})_3$ extraction using HDPA (arrows show water-n-butanol interface), and (D,E) particle size distribution for $\text{Al}(\text{OH})_3$ particles extracted by (D) LG and (E) HDPA

The adsorption of LG and HDPA on $\text{Al}(\text{OH})_3$ particles was confirmed by the FTIR results. Figure. 5-21a,b compares the FTIR spectra of as-received LG and $\text{Al}(\text{OH})_3$ particles, extracted by method 1 using LG. The main bands in the LG spectrum (Fig. 5-21.a) and their assignments were as follows: CH_2 asymmetric and symmetric stretching at 2916 and 2848 cm^{-1} ; ester carbonyl vibrations at 1666 cm^{-1} ; C-C/C=C vibration of aromatic ring at 1608, 1533, 1467 and 1409 cm^{-1} ; C=O stretching at 1380 cm^{-1} ; C-O stretching of phenolic groups at 1301 cm^{-1} ; and ester carbonyl C(=O)-O stretching vibrations at 1257 cm^{-1} . Similar adsorptions can be found in the spectrum of $\text{Al}(\text{OH})_3$ extracted by LG. However, the

adsorption peak at 1301 cm^{-1} decreased drastically, but did not completely disappear(Fig.5-21.b). A similar behavior was observed for hexyl gallate-modified $\text{Al}(\text{OH})_3$ particles. Such behavior indicated that two OH groups of the galloyl ligand were involved in the catecholate-type bonding to the metal atom on the particle surface, whereas the third phenolic OH group remained unbounded. The FTIR spectrum of HDPA(Fig. 5-21.c) showed adsorptions at 2916, 2850 and 1471 cm^{-1} , which can be ascribed to asymmetric stretching, symmetric stretching and bending vibrations of the CH_2 groups, respectively. Similar adsorptions were observed in the spectrum of $\text{Al}(\text{OH})_3$, extracted by HDPA(Fig. 5-21.d). Therefore, the FTIR data confirmed that extracted $\text{Al}(\text{OH})_3$ contained adsorbed LG or HDPA molecules.

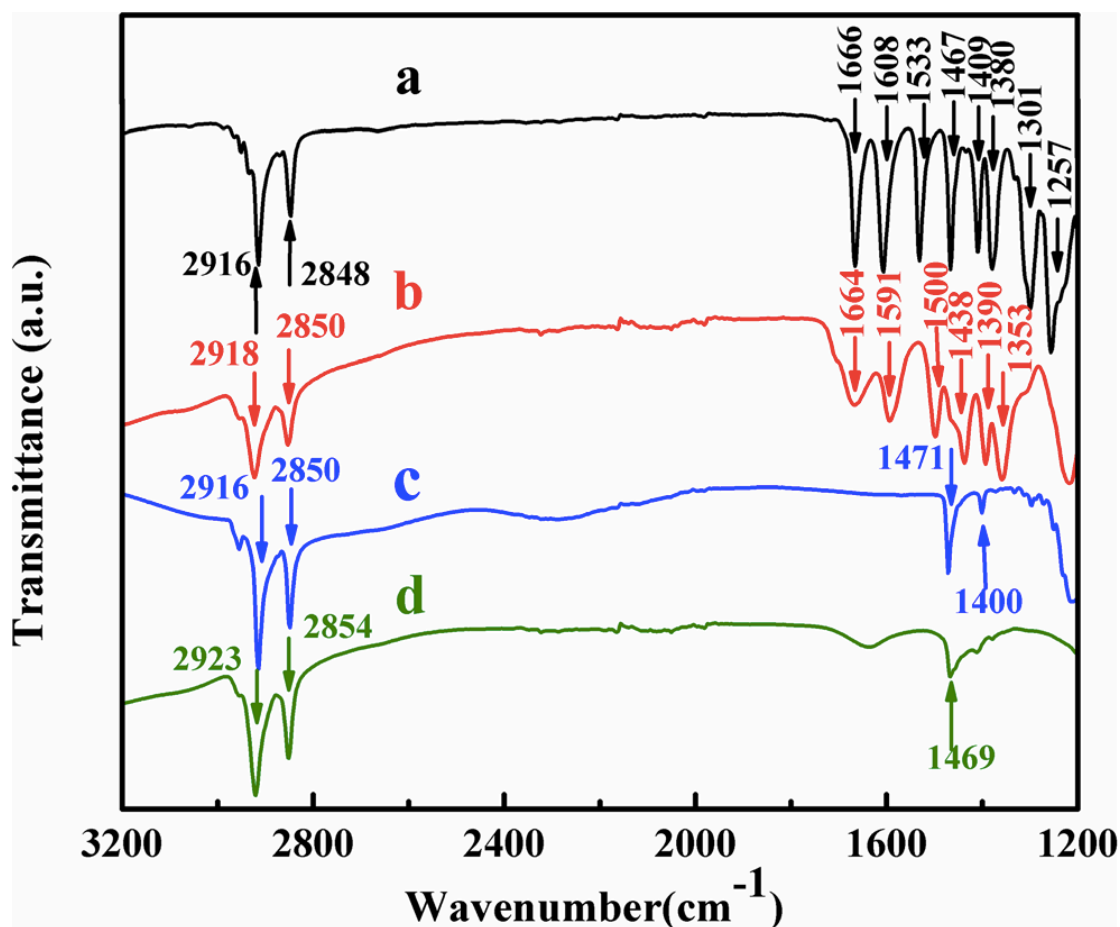


Figure. 5-21. FTIR spectra of (a) LG, (b) Al(OH)₃ extracted using LG, (c) HDPA, and (d) Al(OH)₃ extracted using HDPA

5.3.3 Structure and properties of CMC

CMC is a cellulose-based polymer that has been used as a binder for electrodes¹²⁹. Moreover, its nanocomposites are widely used in biological applications¹³⁰ like biosensors¹³¹, scaffolds¹³² and drug delivery systems¹³³. Aqueous solutions of CMC have the ability to disperse various materials. With excellent binding and film-forming properties, CMC can be exploited in the fabrication of organic-inorganic nanocomposites with functional properties. CMC is an anionic

polyelectrolyte and water-soluble polymer that can be potentially used for film formation by EPD. Different from QHECE, the charge of the CMC macromolecules is negative and pH-dependent, which means anodic EPD can facilitate their charge neutralization and deposit formation in the low-pH region at the anode surface. Similarly, in order to improve the flame retardant properties of CMC, we planned to use anodic EPD to deposit CMC/ Al(OH)₃ nanocomposites.

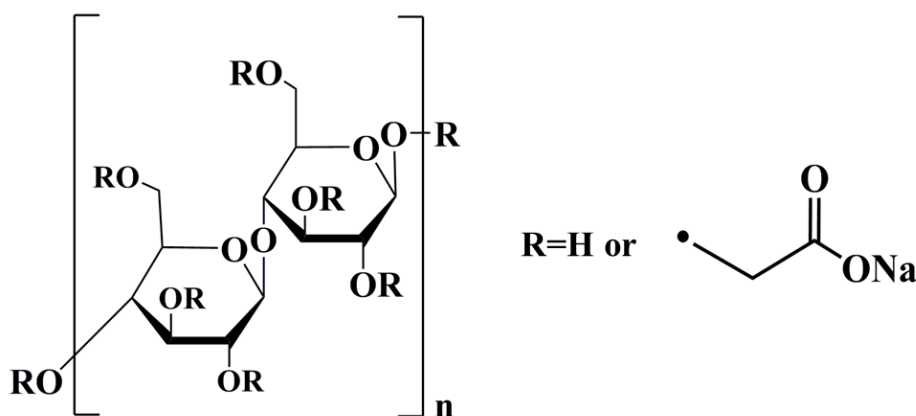


Figure. 5-22. Chemical structure of CMC

5.3.4 Experimental results of anodic EPD

We used QCM method to investigate the deposition yield of CMC. As Fig.5-23.a shows, deposit mass versus deposition time dependence for CMC, deposited from dilute solutions. The QCM data showed continuous mass gain, which indicates film growth at the electrode surface. The deposition yield data, illustrated in Fig.5-23.b, indicated that higher mass gain can be achieved from solutions with higher concentrations. Moreover, the increase in the deposition yield with increasing deposition

time and CMC concentration in the solutions indicated that film thickness can be controlled.

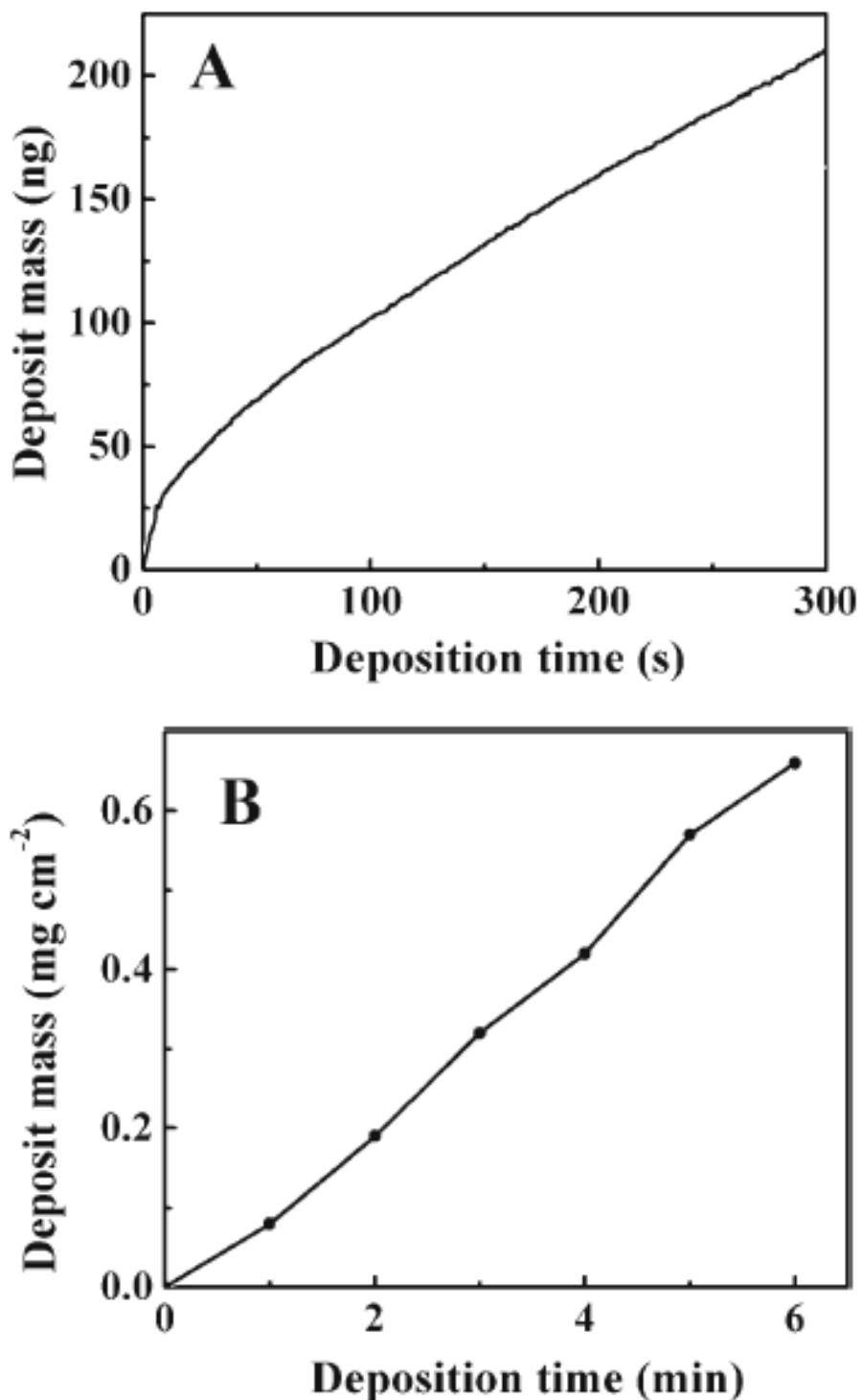
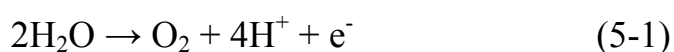


Figure. 5-23. A. Deposit mass versus deposition time, measured using QCM, for the deposition from 0.05 g/L CMC-Na at a deposition voltage of 5V. B. Deposit mass versus deposition time for the deposition from 5 g/L CMC-Na at a deposition voltage of 30V

The film deposition mechanism of CMC is based on the pH-dependent charge and solubility of CMC as well as gel-forming properties of this polymer. Electrophoretic motion of the anionic CMC⁻ macromolecules resulted in their accumulation at the electrode surface, where pH decreased due to the following electrochemical reaction:



The pH reduction of CMC-Na solutions below pH=6 can result in the formation of water-insoluble protonated form of CMC (CMC-H). Thus, the charge neutralization and formation of water-insoluble CMC-H in the electrode reaction,



facilitated film formation. Additionally, the replacement of Na for H in the CMC promoted film formation because of the enhanced hydrogen bonding of the CMC molecules and formation of a gel network.

This suggested deposition mechanism can be confirmed by the FTIR studies of as-received CMC-Na and deposited material(Fig.5-24). The adsorptions at 1589 and 1421cm⁻¹ in the FTIR spectrum of as-received CMC-Na are related to asymmetric and symmetric stretching of -COONa, separately. The adsorption peak at 1325 cm⁻¹ is resulted from the -OH bending vibrations. The additional adsorption at 1726 cm⁻¹ in the spectrum of the deposited material resulted from the stretching vibration

of protonated COOH group. Therefore, the FTIR spectra confirmed the formation of protonated form of CMC (CMC-H).

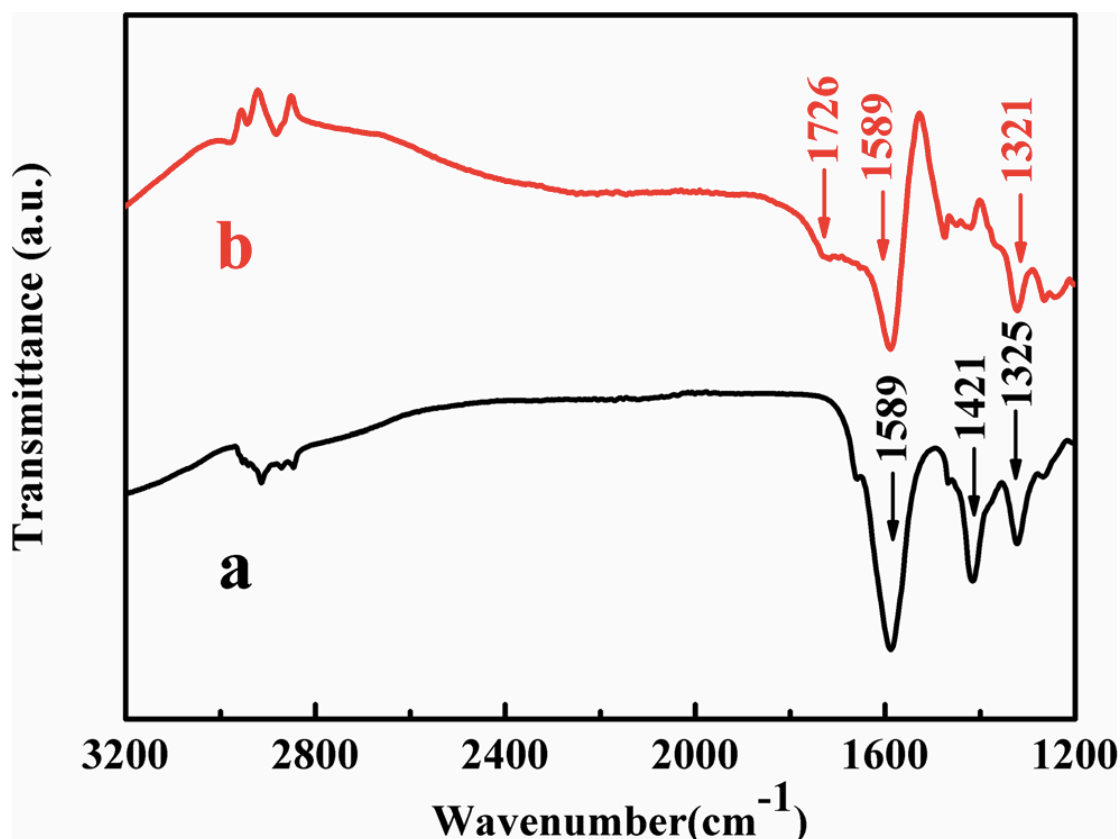


Figure. 5-24. (a) FTIR spectra of as-received CMC-Na and (b) deposited material

Before EPD of CMC-Na solutions, we did sedimentation test for $\text{Al}(\text{OH})_3$ with drying process and $\text{Al}(\text{OH})_3$ with extraction, respectively (Fig. 5-25). Apparently, suspension without extracted $\text{Al}(\text{OH})_3$ showed sedimentation rapidly while another suspension with extracted $\text{Al}(\text{OH})_3$ was stable enough.

After anodic EPD of the stable suspension with extracted $\text{Al}(\text{OH})_3$ and CMC-Na, we did SEM test for the resulting film. It is obvious that anodic EPD allowed the fabrication of smooth and uniform films without large

agglomerated particles(Fig 5-26). Different from large agglomerates causes by drying process, the size of particles prepared by liquid-liquid extraction and EPD was on a submicrometer scale.



Figure. 5-25. Sedimentation test for $\text{Al}(\text{OH})_3$, prepared by (a) precipitation and drying and (b) precipitation and extraction. The suspensions contained 2g/L $\text{Al}(\text{OH})_3$ and 1g/L CMC in a mixed water-alcohol solvent

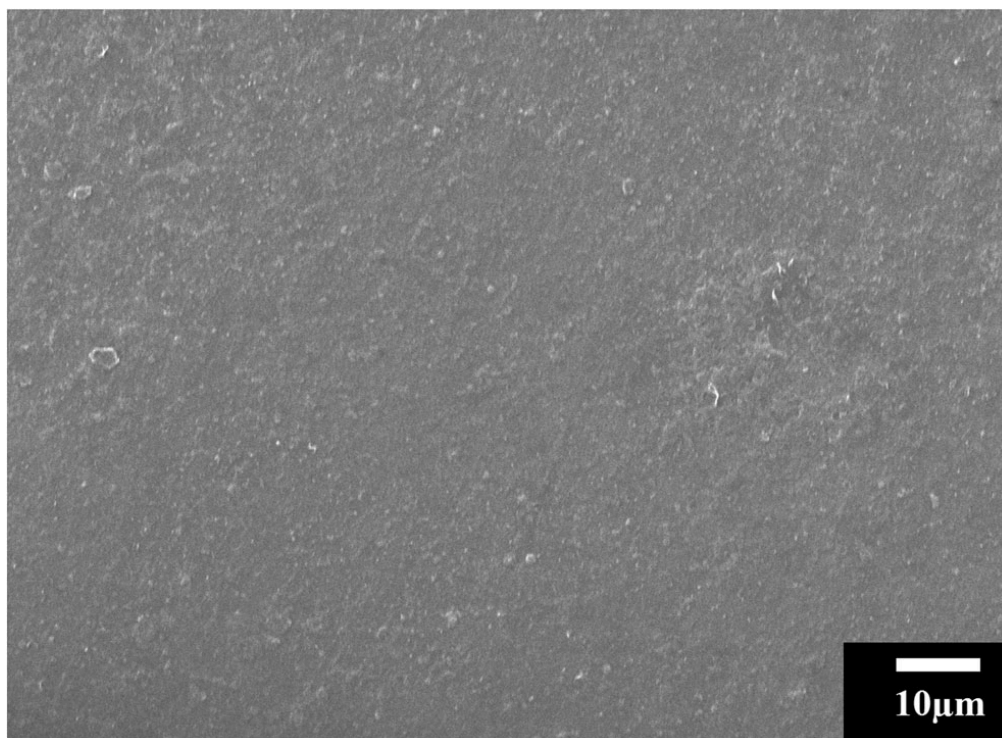


Figure. 5-26. SEM image of a film, prepared by EPD from a suspension, containing 2g/L $\text{Al}(\text{OH})_3$, extracted using LG, and 1 g/L CMC in a mixed water-alcohol solvent

To investigate the incorporation of $\text{Al}(\text{OH})_3$ and the properties of the new deposited composite film, we collected and compared the TGA data and DTA data of $\text{Al}(\text{OH})_3$ and the resulting composite film(Fig. 5-27). For $\text{Al}(\text{OH})_3$, a mass loss of 39.5% was found in the given temperature range of 20-800 °C(Fig. 5-27.a), which resulted from the removal of water and decomposition of $\text{Al}(\text{OH})_3$. The corresponding DTA curve (Fig.5-27.c) has a broad endothermic peak around 120 °C, related to the $\text{Al}(\text{OH})_3$ dehydration. For the TGA data of the new composite film (Fig.5-27.b), there are several steps in mass loss in the given temperature range. The total mass loss at 800 °C was 72.3%, which is related to $\text{Al}(\text{OH})_3$

dehydration and burning out of CMC. When we combine this mass loss with the mass loss of pure $\text{Al}(\text{OH})_3$, the $\text{Al}(\text{OH})_3$ content in the composite film was calculated to be 45.8%. The DTA data of the composite film(Fig.5-27.d) has a broad endothermic peak around 110 °C, which is attributed to the dehydration of both $\text{Al}(\text{OH})_3$ and CMC. The intense exotherm in the range of 430-620 °C is caused by the burning out of CMC. As a result, TGA and DTA data confirmed the formation of composite films, involving flame-retardant $\text{Al}(\text{OH})_3$ in the CMC matrix. Therefore, CMC can be used as a good film forming and charging agent for deposition of various functional inorganic materials and fabrication of new CMC-based composites.

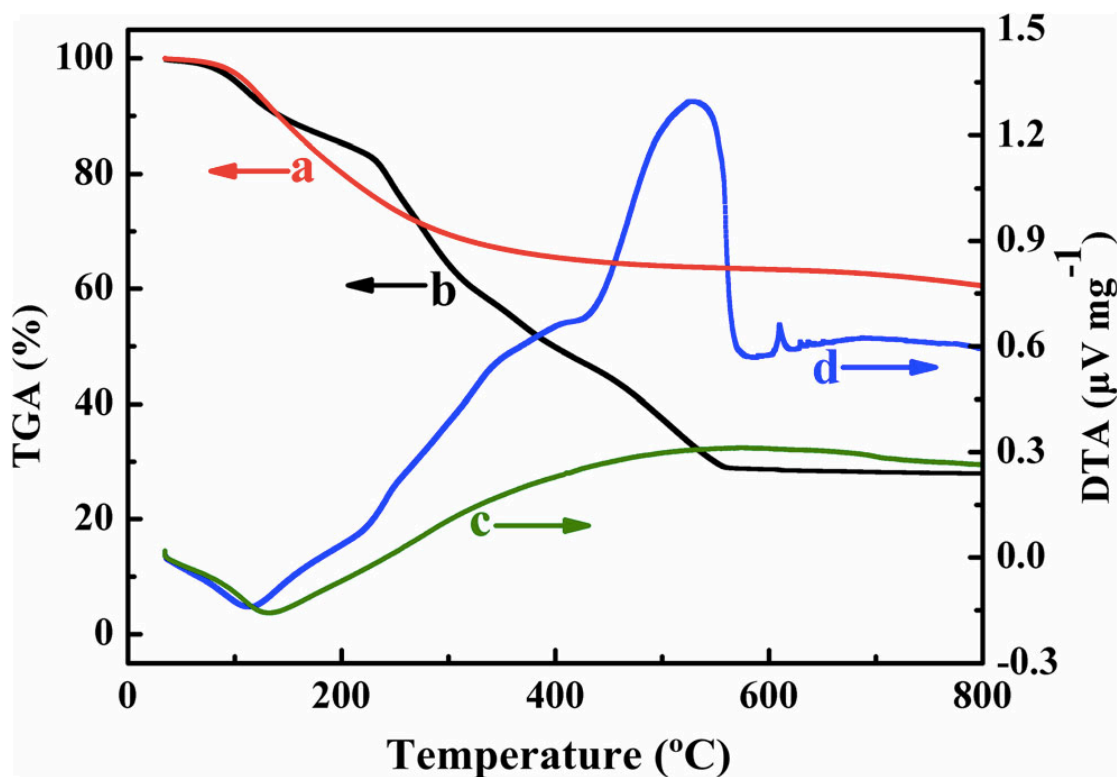


Figure. 5-27. TGA (a,b) and DTA data (c,d) for as-prepared $\text{Al}(\text{OH})_3$ (a,c) and a deposit (b,d), prepared by EPD from a suspension, containing 2 g/L $\text{Al}(\text{OH})_3$, extracted using LG, and 1 g/L CMC in a mixed water-alcohol solvent

5.3.5 Conclusion

Both LG and HDPA can be used as extractors for the one-step liquid-liquid extraction, which is related to their adsorption on $\text{Al}(\text{OH})_3$ by forming polydentate bonding to Al atoms on the particle surface. Based on their different solubility properties, different extraction procedures were developed. However, they can both help to get non-agglomerated $\text{Al}(\text{OH})_3$ particles. The analysis of the experimental data and influence of the extractor structure and chemical properties all provided an insight into the extraction mechanism and efficiency. As a versatile method, one-step liquid-liquid extraction can be extensively used in the process of preparing non-agglomerated oxide particles.

Anodic EPD has been successfully developed for the deposition of CMC films from CMC-Na solutions. The pH decrease at the electrode surface and charge neutralization result in the formation of protonated water-insoluble CMC film at the electrode surface. The deposition yield was varied and could be controlled by the variation of CMC concentration and deposition time. Anodic EPD can also deposit CMC composite film with non-agglomerated $\text{Al}(\text{OH})_3$ particles from the stable suspension, where CMC played as a film-forming and charging agent.

Anodic EPD can be extended into the fields of depositing various polymers and inorganic particles and forming advanced nanocomposites.

5.4 Liquid-liquid extraction of titania

In addition to $\text{Al}(\text{OH})_3$, we also used liquid-liquid extraction to extract other functional metal oxides, such as TiO_2 .

5.4.1 Synthesis of TiO_2

The XRD patterns(Fig.5-28) showed that the synthesized TiO_2 were mainly amorphous.

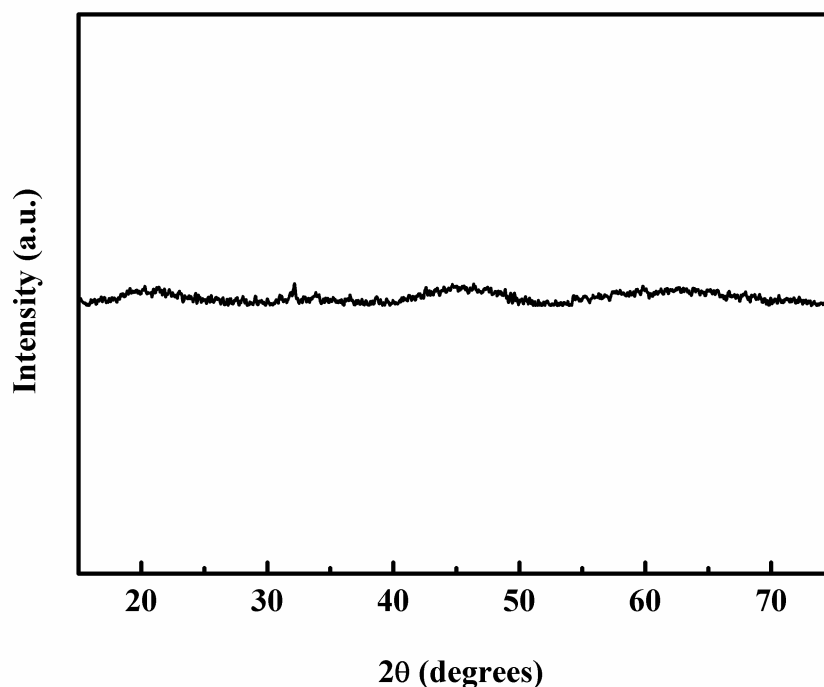


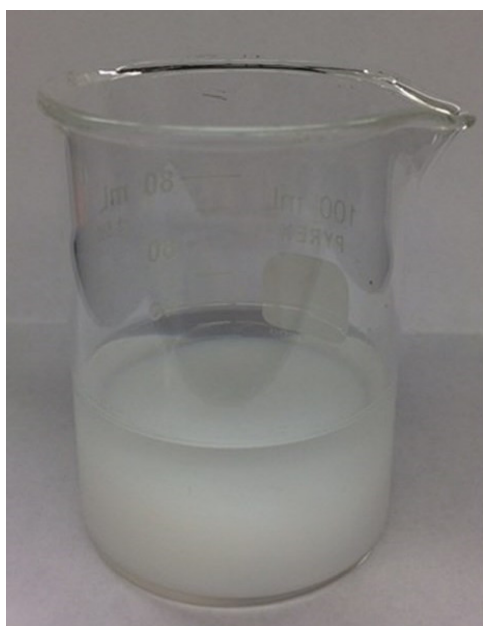
Figure. 5-28. X-ray diffraction pattern of titania

5.4.2 Experimental results of liquid-liquid extraction of titania

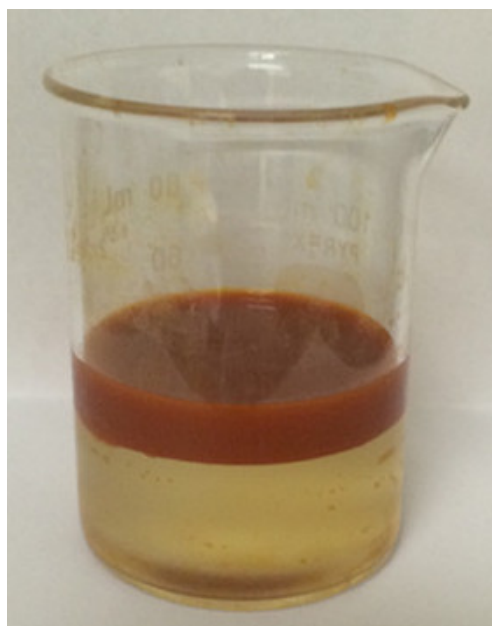
First, we used LG and HDPAs as the extractors for liquid-liquid extraction of titania. For both extractors we used one-step extraction mechanism. The schematic of extraction is shown in Fig.5-29a and b, which illustrates

the images of TiO₂ suspension before and after extraction. We used DLS method to investigate the extracted particles which showed reduced particle agglomeration. The average radius of TiO₂ was only 63 nm (Fig.5-29c). The particle size was significantly lower than the size of agglomerates (Fig.5-29d).

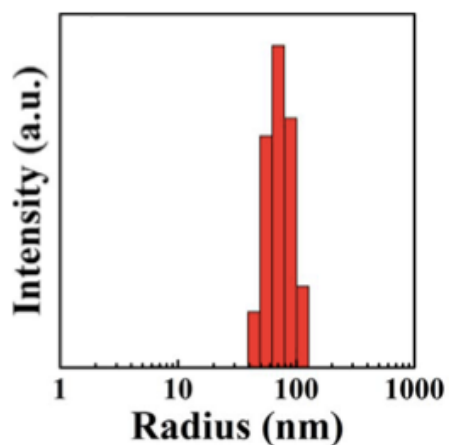
A



B



C



D

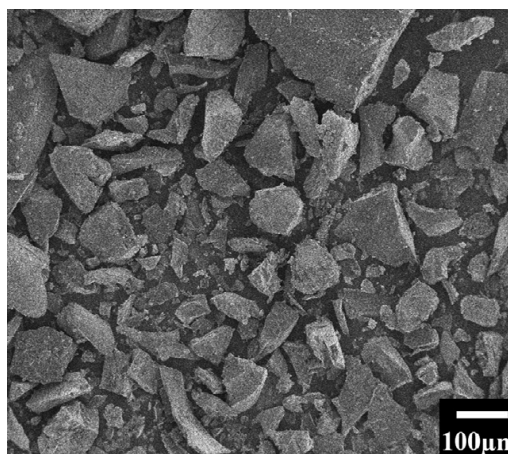


Figure. 5-29. (A) as-prepared titania in water, (B) extraction by the addition of LG in

n-butanol, (C) particle size distribution of titania extracted using LG and (D) SEM image of titania agglomerates

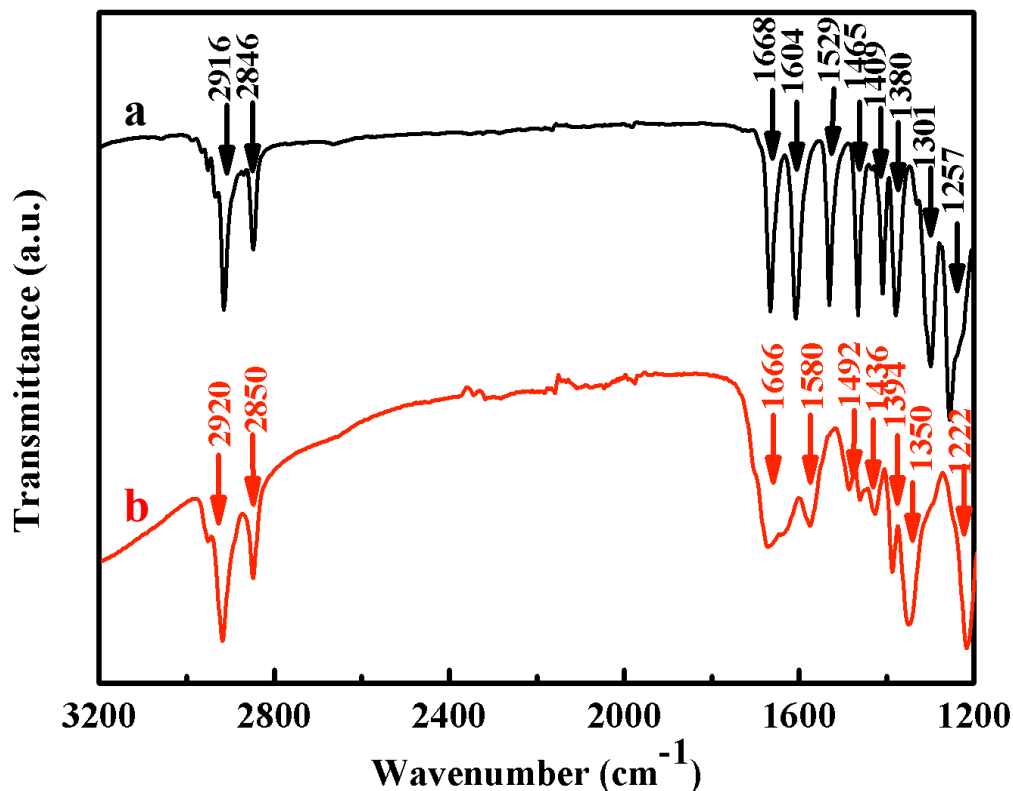
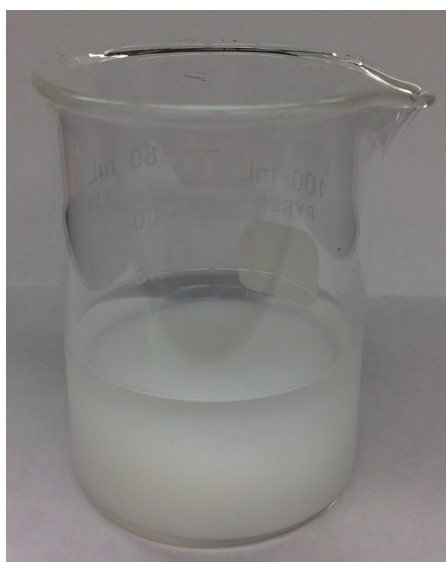


Figure. 5-30. FTIR spectra of (a) LG, (b) TiO₂ extracted using LG

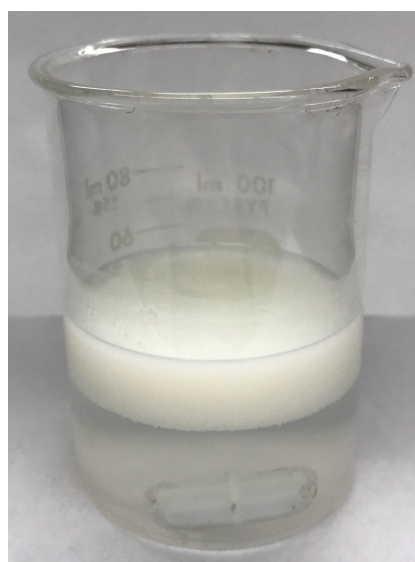
The adsorption of LG on TiO₂ particles was confirmed by the results of FTIR studies. The FTIR spectrum of pure LG (Fig.5-30a) shows adsorptions at 2916 and 2848 cm⁻¹, related to stretching vibrations of CH₂ and CH₃ groups. The spectra of extracted materials (Fig.5-30b) have similar peaks, indicating that LG was successfully adsorbed on the particle surfaces. The peaks in the range of 1400-1600 cm⁻¹, related to stretching C-C vibrations of the aromatic ring of LG (Fig.5-30a) were also found in the spectra of the extracted TiO₂ (Fig.5-30b).

The addition of HDPA solution in n-butanol and stirring resulted in the extraction of TiO_2 from the aqueous phase to n-butanol phase (Fig.5-31a,b). It can be seen that the extracted TiO_2 has formed a stable suspension in n-butanol. The investigation of extracted particles by the DLS showed that the average radius of TiO_2 was around 188.1nm, which indicates that, based on the same one-step extraction mechanism, LG works better than HDPA in the extraction of TiO_2 particles.

A



B



C

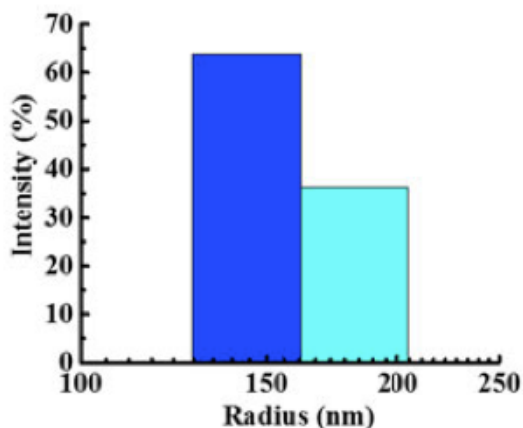


Figure. 5-31. (A) as-prepared titania in water, (B) extraction of titania to the n-butanol solvent after addition of HDPA solution in n-butanol and mixing, red arrow shows the interface of water and n-butanol and (C) particle size distribution of titania extracted using HDPA

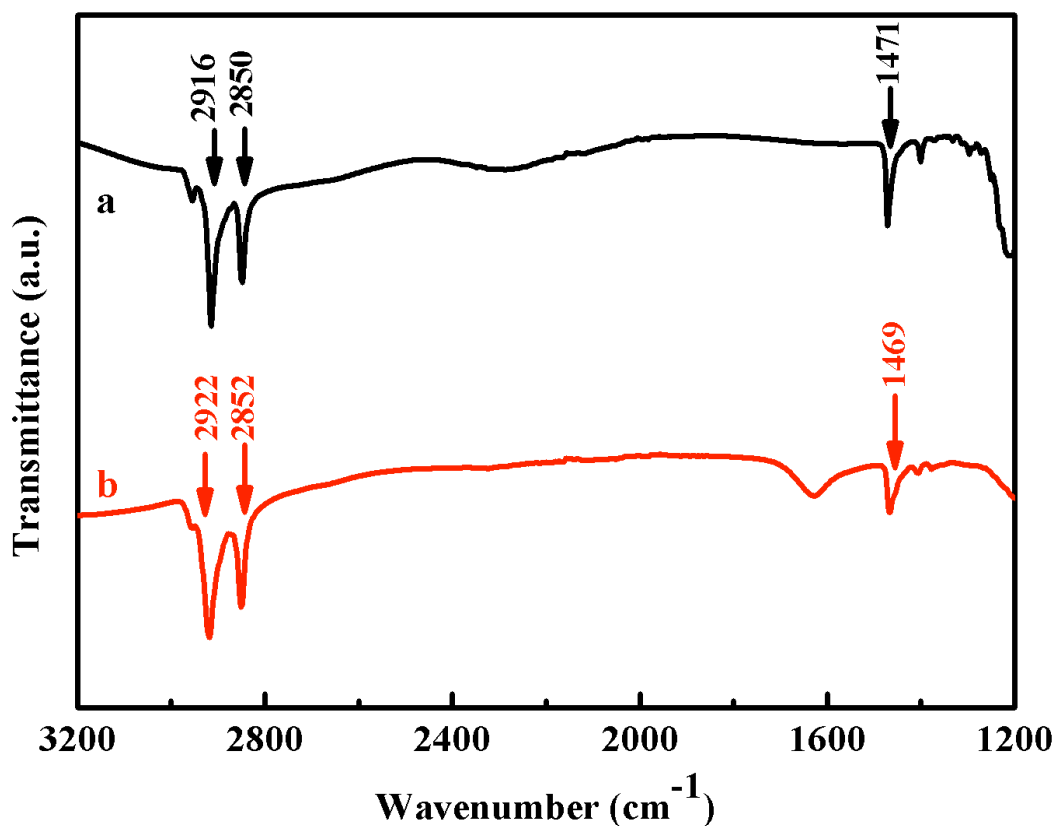


Figure. 5-32. FTIR spectra of (a) HDPA, (b) TiO_2 extracted using HDPA

The extracted particles have also been analyzed by the FTIR method.

Fig.5-32 compares the FTIR spectra of extracted particles and HDPA. The adsorptions in the range of 2800-3000 cm^{-1} in the spectra of TiO_2 particles are attributed to stretching vibrations of CH_2 and CH_3 groups of adsorbed HDPA. The FTIR spectrum of pure HDPA showed similar adsorptions. The adsorptions at 1469 cm^{-1} in the spectra of particles and corresponding adsorption at 1471 cm^{-1} in the spectrum of pure HDPA resulted from the deformation C-H vibrations of HDPA. The strong adsorption of HDPA was critical for the extraction.

In addition to one-step liquid-liquid extraction, we also exploited two-step liquid-liquid extraction for TiO_2 . Similar with $\text{Al}(\text{OH})_3$, R-CHO and NH_2L are also involved in the two-step liquid-liquid extraction for TiO_2 . It was found that R-CHO adsorption on colloidal TiO_2 particles resulted in the color change from white to red (Fig.5-33a). This red color of the particles also remained after their transfer to the organic phase (Fig.5-33b). The clear aqueous phase after the transfer, indicated that the efficient extraction was achieved for relatively high suspension concentration. Besides, the average radius of extracted particles (Fig.5-33c) was found to be 71nm.

A



B



C

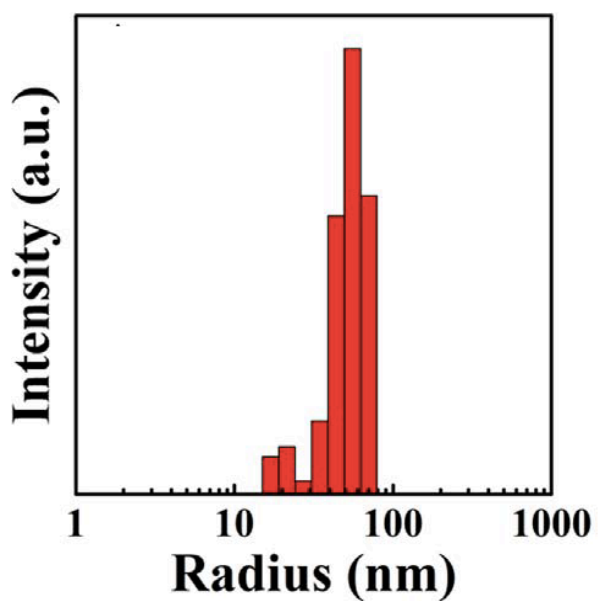


Figure. 5-33. (A) as-prepared titania in water, modified with R-CHO (B) extracted titania using Schiff base reaction and (C) particle size distribution.

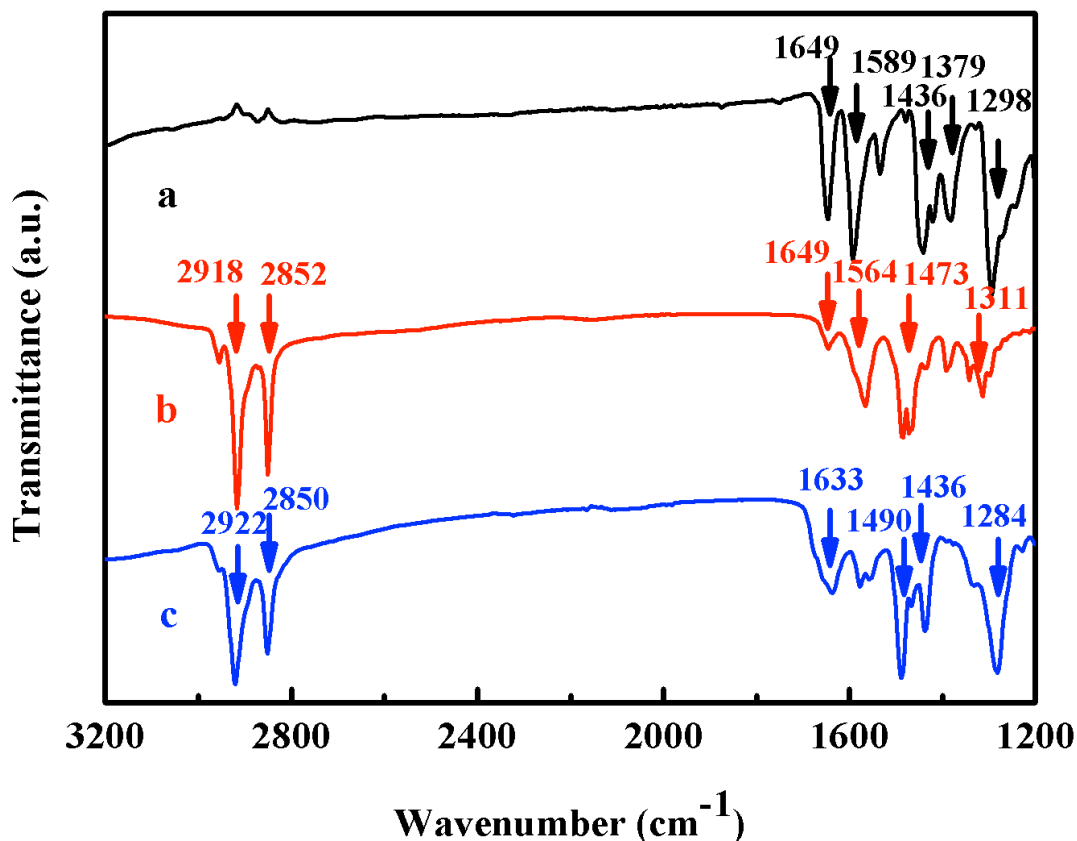


Figure. 5-34. FTIR spectra of (a) R-CHO, (b) NH₂L and (c) TiO₂ extracted using Schiff base reaction

The results of the FTIR also supported the proposed two-step extraction mechanism. Fig.5-34 compared the FTIR spectra of as-received R-CHO, NH₂L and extracted TiO₂ particles. The two peaks at 2848 and 2920 cm⁻¹ in the spectrum of NH₂R are attributed to stretching vibrations of CH₂ and CH₃ groups. The adsorption at 1488 cm⁻¹ resulted from the deformation C-H vibrations. The adsorptions at 1651 and 1589 cm⁻¹ in the spectrum of R-CHO resulted from aromatic C-C vibrations and the adsorption at 1294 cm⁻¹ was attributed to C-O stretching vibrations. Similar adsorptions can be observed in the spectra of the extracted

particles (Fig.5-34c), which indicate that NH_2R and R-CHO adsorbed on the particles and formed a Schiff base.

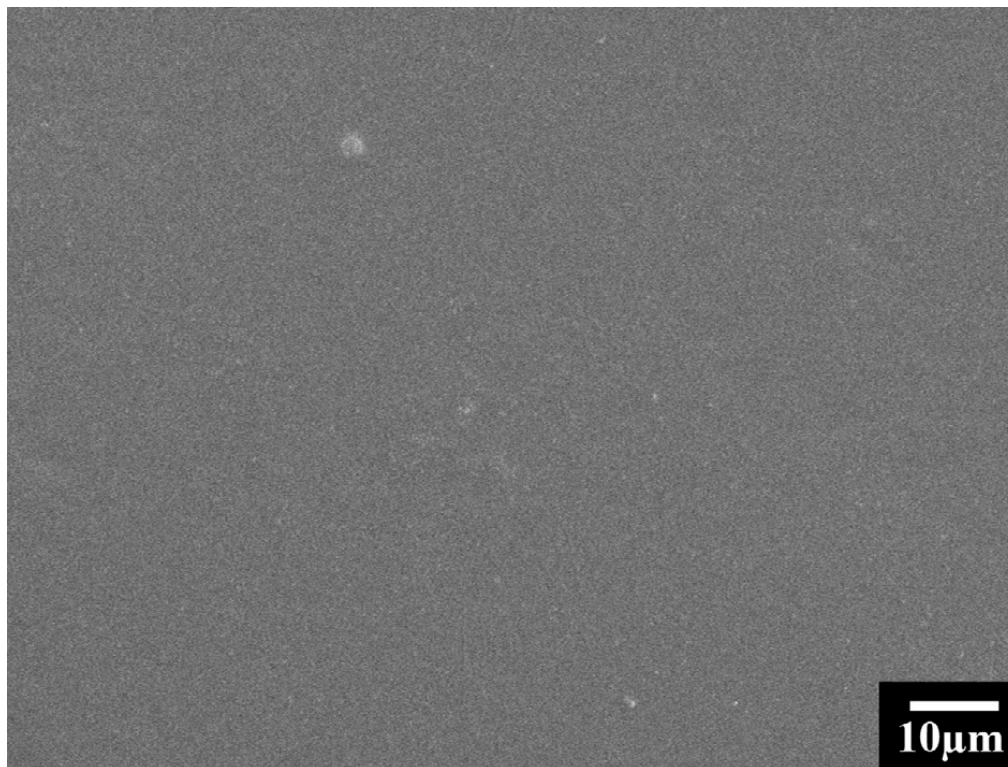


Figure. 5-35. SEM image of a titania-PVB film

In the further investigation of the extracted TiO_2 particles, we mixed titania suspension in n-butanol obtained by liquid-liquid extraction with PVB solution in n-butanol for the deposition of coatings on stainless steel foils by simple dip coating. After that, we performed SEM for the resulting film and found that the surface of the composite titania-PVB film is smooth and non-agglomerated (Fig.5-35). This indicates that the ability to avoid agglomerates can help with the deposition of oxide materials by various techniques.

5.4.3 Conclusion

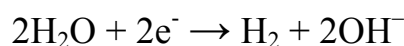
Liquid-liquid extraction techniques have been developed for the extraction of titania, prepared by wet chemical precipitation method. One-step extraction mechanisms involved the adsorption of LG or HDPA on particles at the liquid-liquid interface and extraction. Two-step liquid-liquid extraction mechanism involved the modification of titania particles in-situ during synthesis and Schiff base reaction at the liquid-liquid interface. Composite films were prepared containing non-agglomerated titania in the polymer matrix.

5.5 Cathodic EPD of LPEI and its composite films

Polyethylenimine (PEI), a cationic polymer with high ionic charge density¹³⁴, is widely used as carriers in the gene delivery¹³⁵, coatings for electrodes¹³⁶ and also adsorbent and catalyst for water purification¹³⁷.

These applications of PEI are mainly related to its adsorption and electrokinetic properties¹³⁸. PEI can adsorb on metal oxide nanoparticles

and perform as a dispersant to stabilize related aqueous suspensions¹³⁹. Besides, with film forming and binding properties, PEI can be involved in the fabrication of composite films by EPD method, avoiding the possibility of cracking¹⁴⁰. Adsorbed PEI can allow the electromigration of ceramics in a given electric field through providing a positive charge for the ceramic particles or forming PEI-metal ion complexes¹⁴¹. Compared with branched PEI, linear PEI (LPEI) contains simply secondary amines(Fig.5-36) and nearly insoluble in water, which are critical for the formation of films and composites by EPD. The protonation of its NH groups can form a cationic LPEI-H⁺, which can migrate under a given electric field. With the generation of OH⁻ at the cathode surface,



LPEI-H⁺ can be neutralized at the cathode surface and facilitate the formation of water insoluble LPEI films:

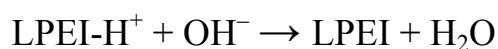


Figure. 5-36. Structure of LPEI

The goal of this investigation was the application of LPEI as a charging and film forming agent for EPD to fabricate LPEI-MgAlLDH, LPEI-halloysite and LPEI-titania composite films.

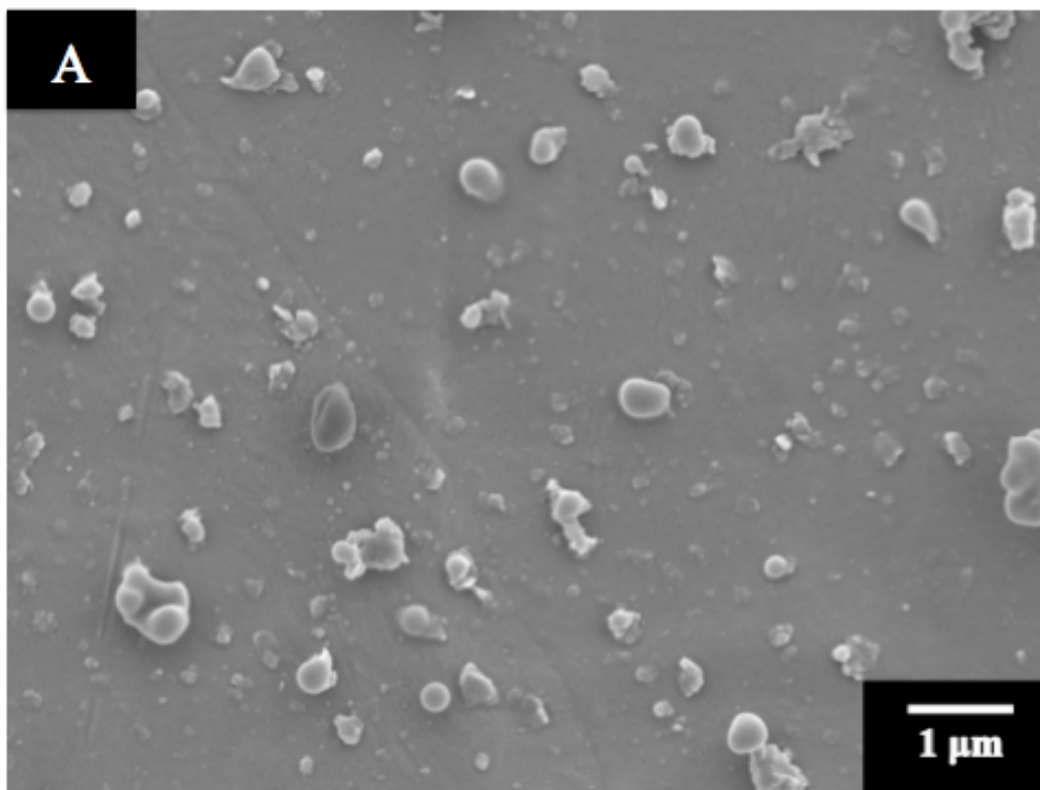
5.5.1 Experimental results of Cathodic EPD of LPEI composite films

The SEM images of LPEI-MgAlLDH composite film obtained by cathodic EPD are shown in Fig.5-37. The film was prepared from 0.5 g/L LPEI suspension, containing 1 g/L MgAlLDH. The surface of the composite film has uniformly packed with MgAlLDH platelets without any crack. Besides, there is no peeling shown on the surface, indicating the adhesion of film on the substrate. However, in the high-magnification image, large agglomerates of MgAlLDH platelets can be observed on the surface.

LPEI-halloysite film was obtained from 0.5 g/L LPEI solution, containing 1 g/L halloysite (Fig.5-38). The film is obviously continuous and crack-free, with a large number of halloysite nanotubes uniformly dispersed in LPEI matrix. In higher magnification, the film is dense and contained halloysite nanotubes aligned parallel to the film surface.

Figure.5-39 shows SEM images of a film prepared from 0.5 g/L LPEI solution, containing 1 g/L titania. The SEM images revealed a great amount of pores existing on the surface. This porosity is related to the

packing of titania particles. The film is relatively dense and contained large amount of titania particles in the LPEI matrix.



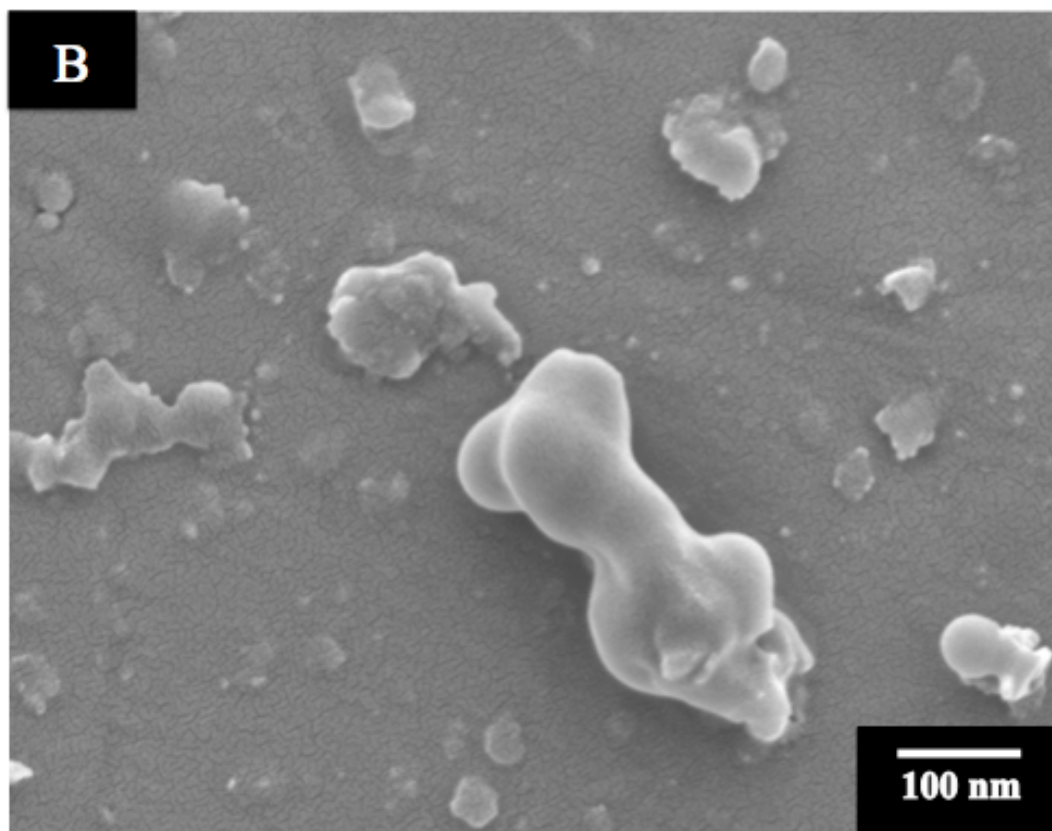


Figure. 5-37. A and B SEM images of LPEI-MgAILDH film at different magnifications, prepared by EPD from 0.5 g/L LPEI solution, containing 1 g/L MgAILDH at a deposition voltage of 30V.

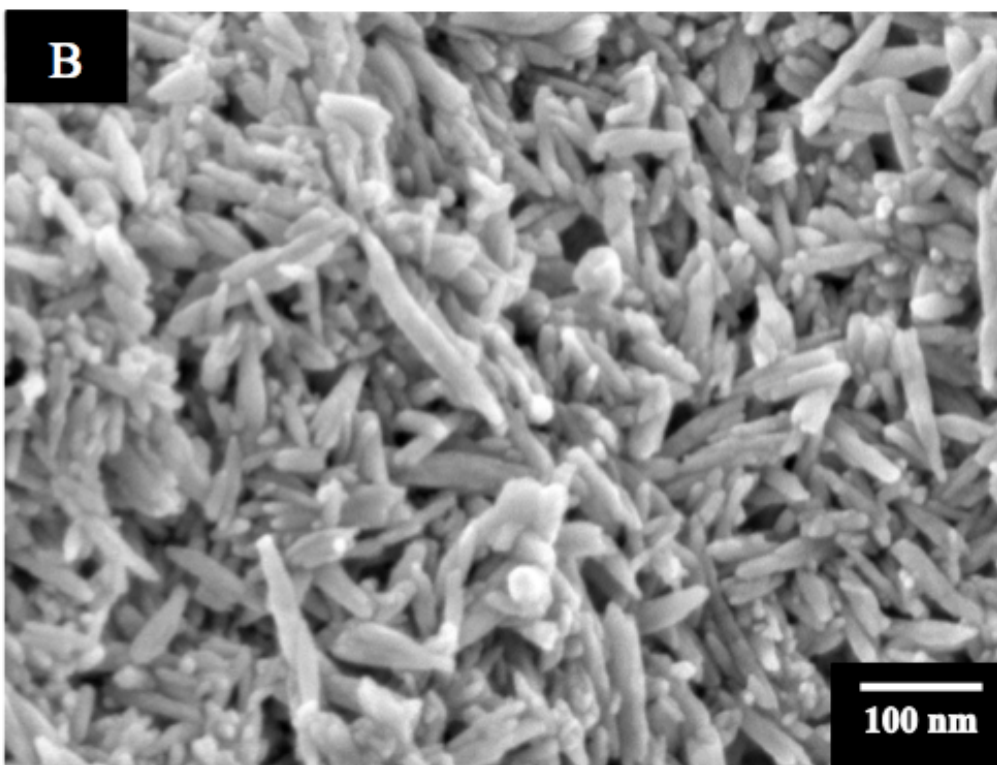
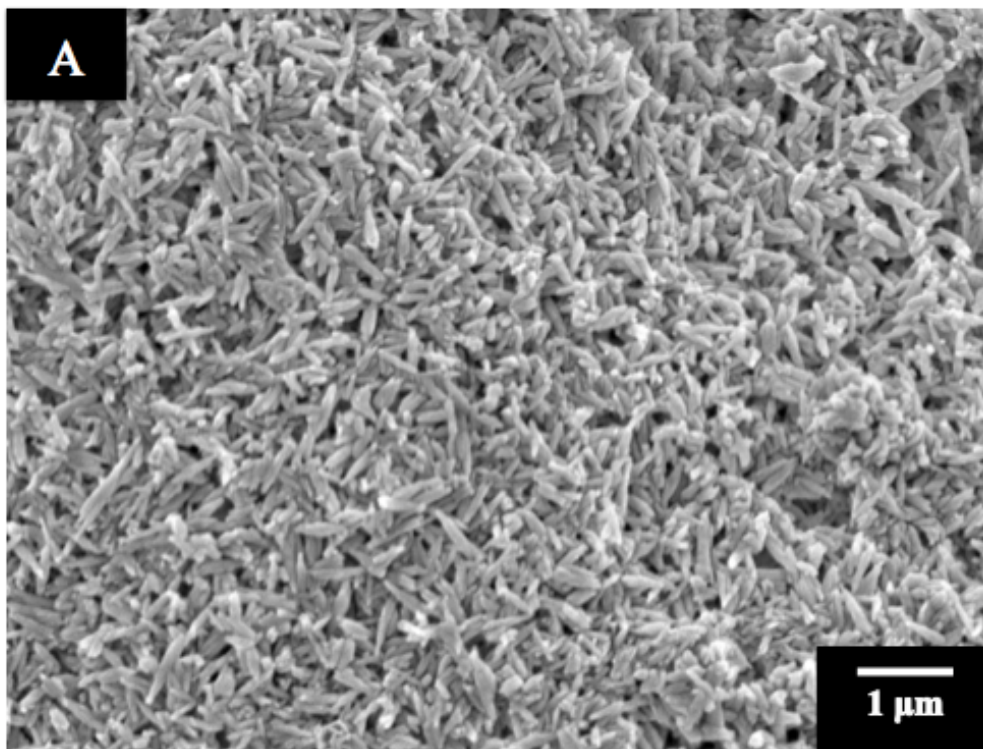


Figure. 5-38. A and B SEM images of LPEI-halloysite film at different magnifications, prepared by EPD from 0.5 g/L LPEI solution, containing 1 g/L halloysite at a deposition voltage of 30V.

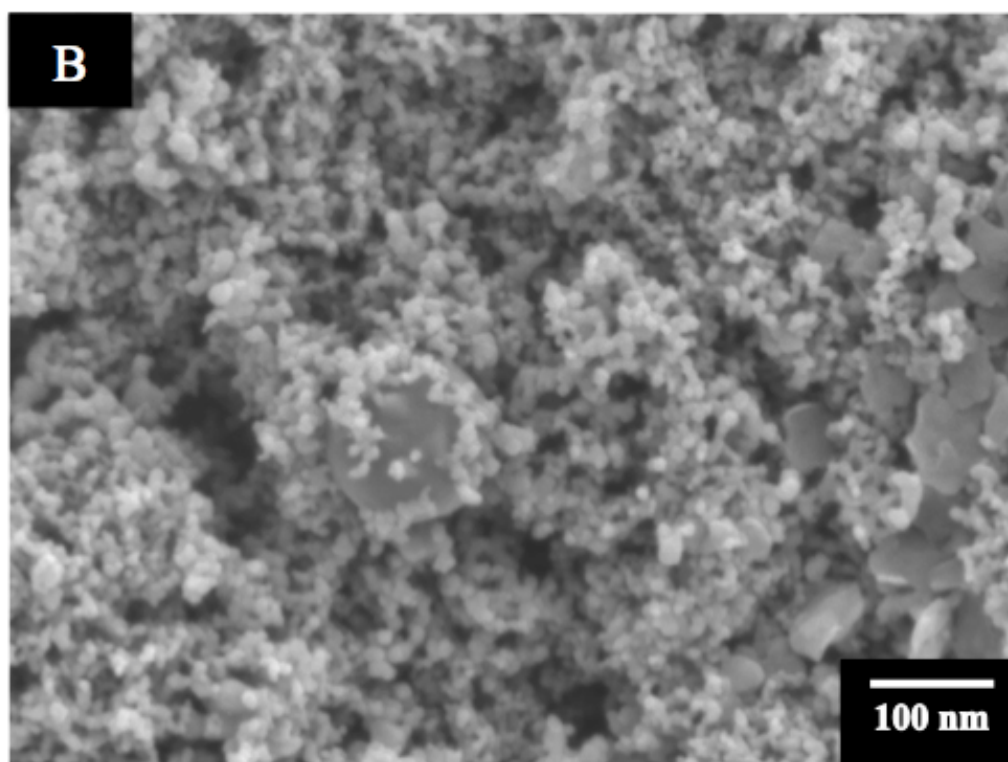
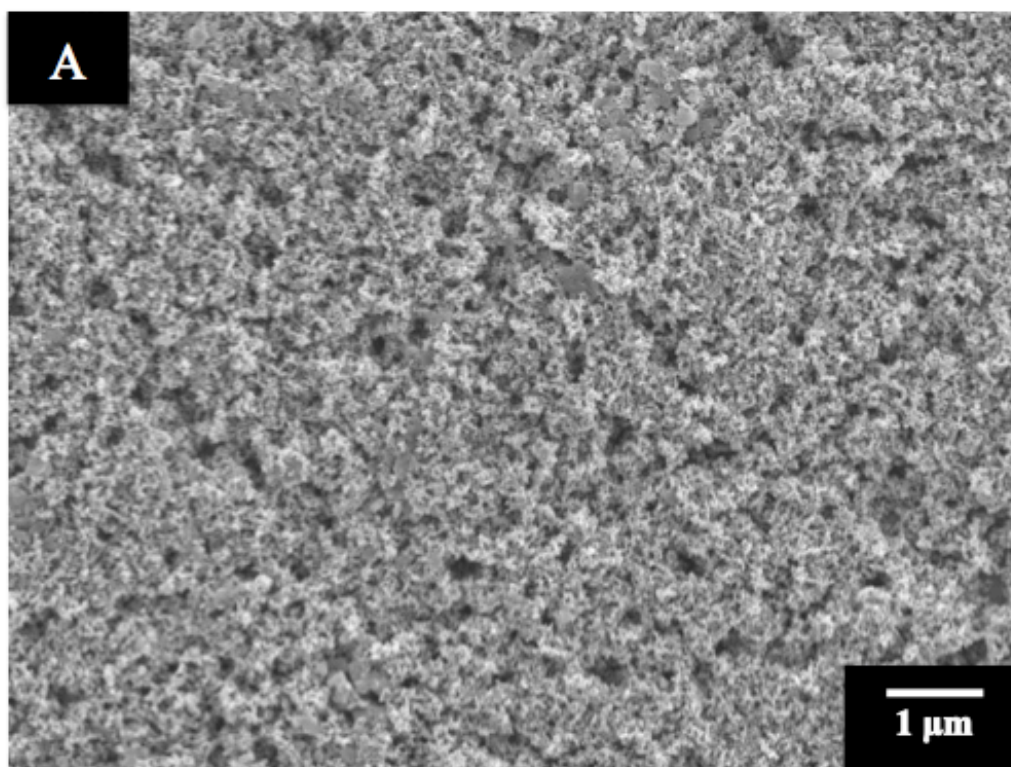


Figure. 5-39. A and B SEM images of LPEI-titania film at different magnifications, prepared by EPD from 0.5 g/L LPEI solution, containing 1 g/L titania at a deposition voltage of 30V.

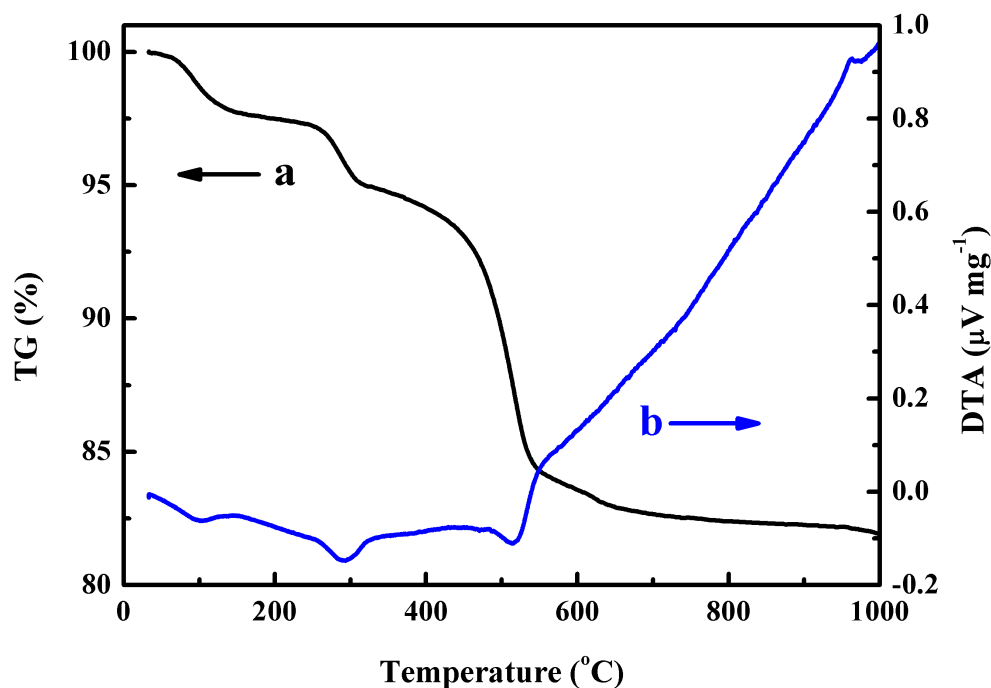


Figure. 5-40. (a) TGA and (b) DTA data for as-received halloysite

The incorporation of halloysite into the PEI composite film can be confirmed by the TGA and DTA analyses. We collected and compared the TGA and DTA data of pure halloysite and LPEI-halloysite composite, prepared by EPD. There are several steps in the results of TGA data of pure halloysite in the given temperature range (Fig.5-40a). In the first step, 5% mass loss can be observed at 100 °C, which was caused by the loss of physically adsorbed water. The second mass loss around 300 °C was related to the thermal dehydration of halloysite in the structure layer and the third large step can be attributed to the decomposition of the hydroxyl groups. In the given temperature range, the mass reduction was mainly observed below 600 °C and the total mass loss at 1000 °C was approximately 17.6%. The TGA data of related composite film also

showed several steps in mass loss, which results from the loss of water and burning out of LPEI (Fig.5-41a). Combined with the DTA curve of the composite (Fig.5-41b), the endothermic peak at 100 °C and other two exothermic peaks in the corresponding temperature can also confirm the reactions. Compared with the total mass loss of pure halloysite, LPEI-halloysite composite showed a totally 35% mass loss at 1000 °C, indicating the formation of composite film.

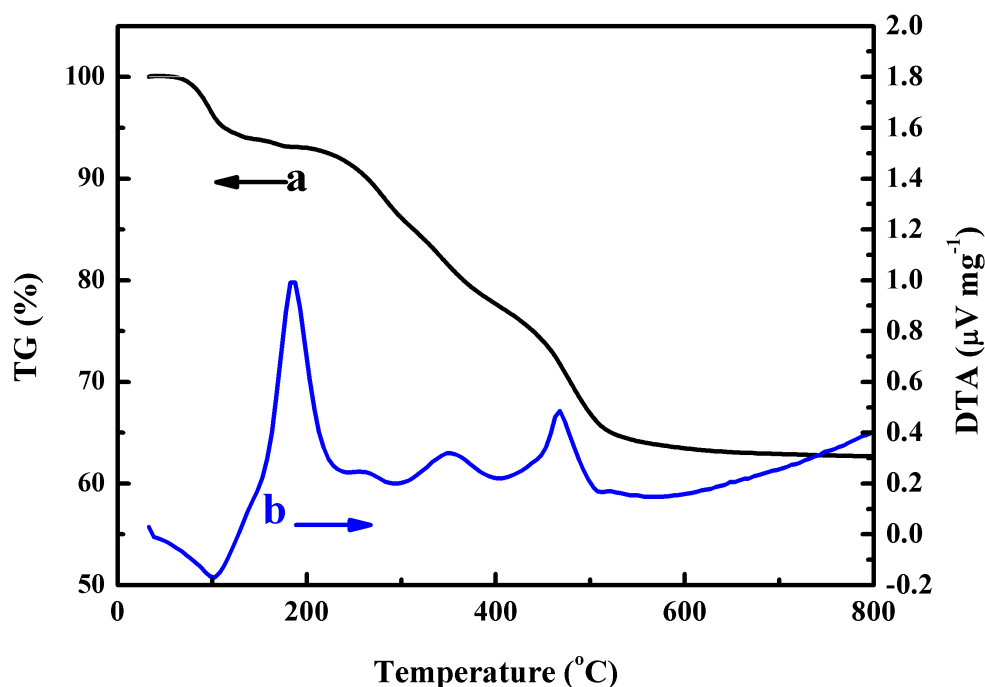


Figure. 5-41. (a) TGA and (b) DTA data for LPEI-halloysite composite film, prepared by EPD from 0.5 g/L LPEI solution, containing 1 g/L halloysite at a deposition voltage of 30V

Figure.5-42 and Figure.5-43 illustrated the TGA and DTA curves of pure MgAILDH and LPEI-MgAILDH composite film, respectively. For the pure MgAILDH, there are two steps of mass loss in its TGA curve. The

first step at 200 °C can be ascribed to the desorption of water and the second step at 400 °C was related to the dehydroxylation of MgAILDH layers. Correspondingly, the two endothermic peaks at related temperature can support these reactions. The total weight loss at 800 °C was 37%. Similar weight loss steps can be found in the TGA curve of LPEI-MgAILDH composite film at the silimilar temperature but the total weight loss has been rose to 50%. In addition to the two endothermic peaks, an intense exothermic peak occurs at 240 °C was observed, which resulted from the burning out of LPEI. Consequently, the formation of LPEI-MgAILDH composite film can be confirmed.

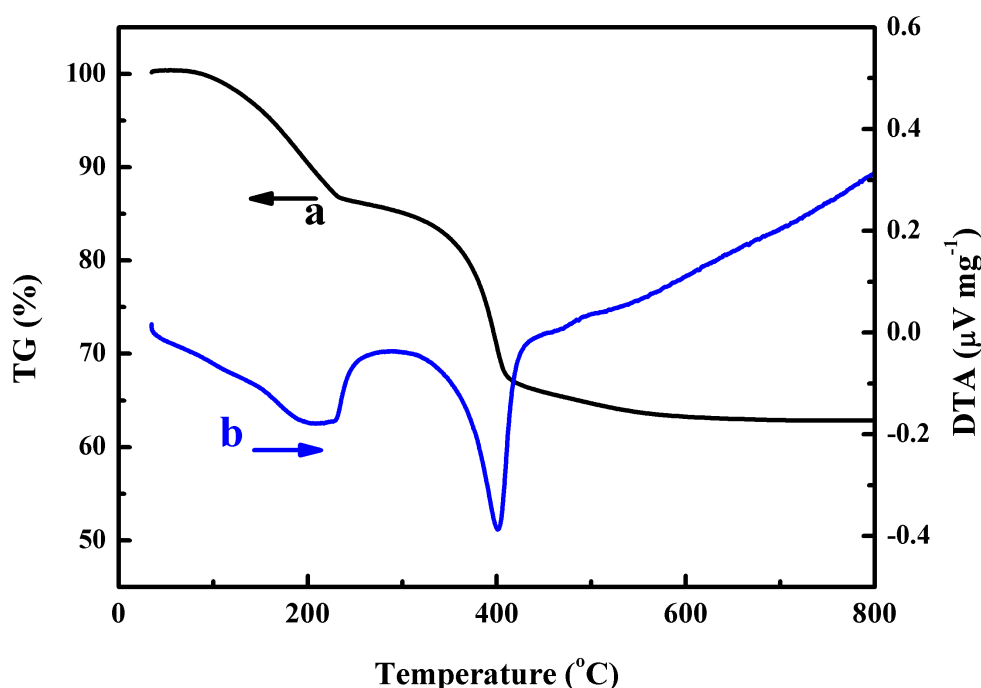


Figure. 5-42. (a) TGA and (b) DTA data for as-received MgAILDH

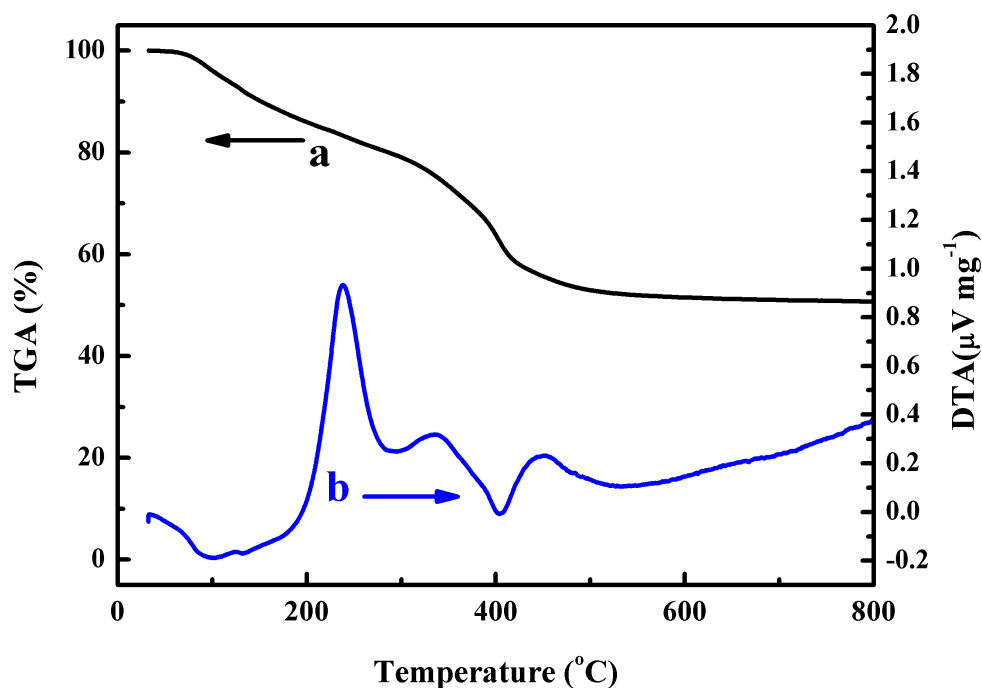


Figure. 5-43. (a) TGA and (b) DTA data for LPEI-MgAILDH composite film, prepared by EPD from 0.5 g/L LPEI solution, containing 1 g/L MgAILDH at a deposition voltage of 30V

5.5.2 Conclusion

PEI films were deposited by cathodic EPD. The deposition mechanism involved dissolution of PEI in acidic solution, electrophoresis of cationic PEI molecules toward cathode, local pH increase at the cathode surface, charge neutralization and deposition of PEI films.

PEI can be used as a charging, dispersing and film forming agent for the deposition of titania, MaAILDH and halloysite. Composite films were prepared by cathodic EPD. SEM, TGA and DTA data confirmed the

formation of composite films. The MgAlLDH and halloysite particles incorporated into the PEI matrix imparted flame retardant properties to the films.

6. Conclusions

In our investigation, liquid-liquid extraction has been successfully used for the reduction of particles agglomeration and also helped to achieve the requirement of relative stable suspension. Two extraction mechanisms, one-step liquid-liquid extraction and two-step liquid-liquid extraction, were both found to be effective. Different extractors follow different extraction mechanisms, which are determined by their structures.

LG and HDPA are confirmed as typical extractors, which are based on the one-step liquid-liquid extraction. The galloyl group of LG and phosphonate group of HDPA allowed their adsorption on metal oxides by forming polydentate bonding to metal atoms on the particles. Moreover, different solubility of LG and HDPA can result in their different extraction procedure but the related mechanisms are similar. The analysis of the experiments and deep understanding of the extractor structure and corresponding properties pave the way for the future investigation of new extractors.

Compared with one-step liquid-liquid extraction, the two-step liquid-liquid extraction involves the surface modification of inorganic particles during synthesis and a second modification based on Schiff base reaction. Similarly, the first modification is related to the adsorption properties of phenolic OH groups of DBA and TBA. This extraction

process also effectively reduced the particle size and improved the stability of the suspension for future EPD. The ability of reducing particle growth during synthesis can help to extract smaller particles than the one-step liquid-liquid extraction. However, the process of one-step liquid-liquid extraction is simpler than that of two-step liquid-liquid extraction.

Extracted $\text{Al}(\text{OH})_3$ particles and polyelectrolytes have been deposited by EPD and formed uniform composite films without cracking and agglomerates. The film forming and charging properties of the polyelectrolytes allowed the reduction of cracking and improved the deposition adhesion. The pH change at the electrode surface and charge neutralization result in the formation of polymer film at the electrode surface. Cathodic EPD has been employed for the fabrication of QHECE composite films and PEI composite films while anodic EPD has been exploited in the fabrication of CMC composite films. The amounts of deposits were found to be controlled by the variation of time and also concentration of polyelectrolytes.

Containing the flame retardant $\text{Al}(\text{OH})_3$ particles, the QHECE composite film and CMC composite film showed improved flame retardant properties in the analysis of their TGA and DTA data. Similarly, with the incorporation of MgAlLDH or halloysite particles, PEI composite films have also been imparted flame retardant properties.

The developed liquid-liquid extraction mechanisms can be also involved in the extraction of some other functional inorganic particles like metals, hydroxides and oxides in the future. Besides, further development of liquid-liquid extraction methods can be exploited for the fabrication of advanced polymer nanocomposites, containing various functional inorganic materials and EPD can perform as a versatile technique in the fabrication of inorganic-organic nanocomposites.

7. References

1. Verwey, E. J. W., Overbeek, J. T. G. & Overbeek, J. T. G. *Theory of the Stability of Lyophobic Colloids*. (Courier Corporation, 1999).
2. Zhitomirsky, I. Cathodic electrodeposition of ceramic and organoceramic materials. Fundamental aspects. *Adv. Colloid Interface Sci.* **97**, 279–317 (2002).
3. Pashley, R. M. & Israelachvili, J. N. DLVO and hydration forces between mica surfaces in Mg²⁺, Ca²⁺, Sr²⁺, and Ba²⁺ chloride solutions. *J. Colloid Interface Sci.* **97**, 446–455 (1984).
4. Pashley, R. M. DLVO and hydration forces between mica surfaces in Li⁺, Na⁺, K⁺, and Cs⁺ electrolyte solutions: A correlation of double-layer and hydration forces with surface cation exchange properties. *J. Colloid Interface Sci.* **83**, 531–546 (1981).
5. Zhang, Y. & Cremer, P. S. Interactions between macromolecules and ions: the Hofmeister series. *Curr. Opin. Chem. Biol.* **10**, 658–663 (2006).
6. Bhattacharjee, S., Ko, C.-H. & Elimelech, M. DLVO Interaction between Rough Surfaces. *Langmuir* **14**, 3365–3375 (1998).
7. Ninham, B. W. On progress in forces since the DLVO theory. *Adv. Colloid Interface Sci.* **83**, 1–17 (1999).
8. Pashley, R. M. Hydration forces between mica surfaces in electrolyte solutions. *Adv. Colloid Interface Sci.* **16**, 57–62 (1982).

9. Boström, M., Williams, D. R. M. & Ninham, B. W. Specific Ion Effects: Why DLVO Theory Fails for Biology and Colloid Systems. *Phys. Rev. Lett.* **87**, 168103 (2001).
10. Ducker, W. A., Xu, Z., Clarke, D. R. & Israelachvili, J. N. Forces between Alumina Surfaces in Salt Solutions: Non-DLVO Forces and the Implications for Colloidal Processing. *J. Am. Ceram. Soc.* **77**, 437–443 (1994).
11. Grasso*, D., Subramaniam, K., Butkus, M., Strevett, K. & Bergendahl, J. A review of non-DLVO interactions in environmental colloidal systems. *Rev. Environ. Sci. Biotechnol.* **1**, 17–38 (2002).
12. Parks, G. A. The Isoelectric Points of Solid Oxides, Solid Hydroxides, and Aqueous Hydroxo Complex Systems. *Chem. Rev.* **65**, 177–198 (1965).
13. Dickinson, E. & Eriksson, L. Particle flocculation by adsorbing polymers. *Adv. Colloid Interface Sci.* **34**, 1–29 (1991).
14. Van der Biest, O. O. & Vandeperre, L. J. Electrophoretic deposition of materials. *Annu. Rev. Mater. Sci.* **29**, 327–352 (1999).
15. Sarkar, P. & Nicholson, P. S. Electrophoretic deposition (EPD): mechanisms, kinetics, and application to ceramics. *J. Am. Ceram. Soc.* **79**, 1987–2002 (1996).
16. Hamaker, H. & Verwey, E. Part II.—(C) Colloid stability. The role of the forces between the particles in electrodeposition and other phenomena.

Trans. Faraday Soc. **35**, 180–185 (1940).

17. Fukada, Y., Nagarajan, N., Mekky, W., Bao, Y., Kim, H. S., & Nicholson, P. S. Electrophoretic deposition—mechanisms, myths and materials. *J. Mater. Sci.* **39**, 787–801 (2004).

18. Grillon, F., Fayeulle, D. & Jeandin, M. Quantitative image analysis of electrophoretic coatings. *J. Mater. Sci. Lett.* **11**, 272–275 (1992).

19. Corni, I., Ryan, M. P. & Boccaccini, A. R. Electrophoretic deposition: From traditional ceramics to nanotechnology. *J. Eur. Ceram. Soc.* **28**, 1353–1367 (2008).

20. Ristenpart, W. D., Aksay, I. A. & Saville, D. A. Assembly of colloidal aggregates by electrohydrodynamic flow: Kinetic experiments and scaling analysis. *Phys. Rev. E* **69**, 021405 (2004).

21. Sarkar Partho, Haung Xuening & Nicholson Patrick S. Structural Ceramic Microlaminates by Electrophoretic Deposition. *J. Am. Ceram. Soc.* **75**, 2907–2909 (2005).

22. Anné Guy, Vanmeensel Kim, Vleugels Jef & Van der Biest Omer. A Mathematical Description of the Kinetics of the Electrophoretic Deposition Process for Al₂O₃-Based Suspensions. *J. Am. Ceram. Soc.* **88**, 2036–2039 (2005).

23. Jones Stanley L. & Norman Colin J. Dehydration of Hydrous Zirconia with Methanol. *J. Am. Ceram. Soc.* **71**, C-190-C-191 (2005).

24. Aruna, S. T. & Rajam, K. S. A study on the electrophoretic deposition

- of 8YSZ coating using mixture of acetone and ethanol solvents. *Mater. Chem. Phys.* **111**, 131–136 (2008).
25. Du, C., Heldbrant, D. & Pan, N. Preparation and preliminary property study of carbon nanotubes films by electrophoretic deposition. *Mater. Lett.* **57**, 434–438 (2002).
26. Damodaran, R. & Moudgil, B. M. Electrophoretic deposition of calcium phosphates from non-aqueous media. *Colloids Surf. Physicochem. Eng. Asp.* **80**, 191–195 (1993).
27. Zunic, M., Chevallier, L., Deganello, F., D'Epifanio, A., Licoccia, S., Di Bartolomeo, E., & Traversa, E. Electrophoretic deposition of dense BaCe_{0.9}Y_{0.1}O_{3-x} electrolyte thick-films on Ni-based anodes for intermediate temperature solid oxide fuel cells. *J. Power Sources* **190**, 417–422 (2009).
28. Dusoulier, L., Cloots, R., Vertruyen, B., Moreno, R., Burgos-Montes, O., & Ferrari, B. YBa₂Cu₃O_{7-x} dispersion in iodine acetone for electrophoretic deposition: Surface charging mechanism in a halogenated organic media. *J. Eur. Ceram. Soc.* **31**, 1075–1086 (2011).
29. Sun, Y., Wang, Y. & Zhitomirsky, I. Dispersing agents for electrophoretic deposition of TiO₂ and TiO₂-carbon nanotube composites. *Colloids Surf. Physicochem. Eng. Asp.* **418**, 131–138 (2013).
30. Zarbov, M., Schuster, I. & Gal-Or, L. Methodology for selection of charging agents for electrophoretic deposition of ceramic particles. *J.*

Mater. Sci. **39**, 813–817 (2004).

31. Du, C. & Pan, N. Supercapacitors using carbon nanotubes films by electrophoretic deposition. *J. Power Sources* **160**, 1487–1494 (2006).

32. Ma, R. Z., Liang, J., Wei, B. Q., Zhang, B., Xu, C. L., & Wu, D. H. Study of electrochemical capacitors utilizing carbon nanotube electrodes. *J. Power Sources* **84**, 126–129 (1999).

33. Cabot, B. & Foissy, A. Reversal of the surface charge of a mineral powder: application to electrophoretic deposition of silica for anticorrosion coatings. *J. Mater. Sci.* **33**, 3945–3952 (1998).

34. S. Ata, M., Liu, Y. & Zhitomirsky, I. A review of new methods of surface chemical modification, dispersion and electrophoretic deposition of metal oxide particles. *RSC Adv.* **4**, 22716–22732 (2014).

35. Jiang, L., Gao, L. & Liu, Y. Adsorption of salicylic acid, 5-sulfosalicylic acid and Tiron at the alumina–water interface. *Colloids Surf. Physicochem. Eng. Asp.* **211**, 165–172 (2002).

36. Hanaor, D., Michelazzi, M., Leonelli, C. & Sorrell, C. C. The effects of carboxylic acids on the aqueous dispersion and electrophoretic deposition of ZrO₂. *J. Eur. Ceram. Soc.* **32**, 235–244 (2012).

37. R. Rice, C., D. Ward, M., K. Nazeeruddin, M. & Grätzel, M. Catechol as an efficient anchoring group for attachment of ruthenium–polypyridine photosensitisers to solar cells based on nanocrystalline TiO₂ films. *New J. Chem.* **24**, 651–652 (2000).

38. Wang, Y. & Zhitomirsky, I. Electrophoretic Deposition of Manganese Dioxide–Multiwalled Carbon Nanotube Composites for Electrochemical Supercapacitors. *Langmuir* **25**, 9684–9689 (2009).
39. Togashi, T., Takami, S., Kawakami, K., Yamamoto, H., Naka, T., Sato, K., ... & Adschiri, T. Continuous hydrothermal synthesis of 3,4-dihydroxyhydrocinnamic acid-modified magnetite nanoparticles with stealth-functionality against immunological response. *J. Mater. Chem.* **22**, 9041–9045 (2012).
40. Araujo, P. Z., Morando, P. J. & Blesa, M. A. Interaction of Catechol and Gallic Acid with Titanium Dioxide in Aqueous Suspensions. 1. Equilibrium Studies. *Langmuir* **21**, 3470–3474 (2005).
41. Regazzoni, A. E., Mandelbaum, P., Matsuyoshi, M., Schiller, S., Bilmes, S. A., & Blesa, M. A. Adsorption and Photooxidation of Salicylic Acid on Titanium Dioxide: A Surface Complexation Description. *Langmuir* **14**, 868–874 (1998).
42. Dobson, K. D. & McQuillan, A. J. In situ infrared spectroscopic analysis of the adsorption of aromatic carboxylic acids to TiO₂, ZrO₂, Al₂O₃, and Ta₂O₅ from aqueous solutions. *Spectrochim. Acta. A. Mol. Biomol. Spectrosc.* **56**, 557–565 (2000).
43. Biber, M. V. & Stumm, W. An In-Situ ATR-FTIR Study: The Surface Coordination of Salicylic Acid on Aluminum and Iron(III) Oxides. *Environ. Sci. Technol.* **28**, 763–768 (1994).

44. Hidber, P. C., Graule, T. J. & Gauckler, L. J. Competitive Adsorption of Citric Acid and Poly(vinyl alcohol) onto Alumina and Its Influence on the Binder Migration during Drying. *J. Am. Ceram. Soc.* **78**, 1775–1780 (1995).
45. Grandfield, K. & Zhitomirsky, I. Electrophoretic deposition of composite hydroxyapatite–silica–chitosan coatings. *Mater. Charact.* **59**, 61–67 (2008).
46. Russ, B. E. An Analysis of the Binder Formation in Electrophoretic Deposition. *J. Electrochem. Soc.* **145**, 1253 (1998).
47. de Beer, E., Duval, J. & Meulenkaamp, E. A. Electrophoretic Deposition: A Quantitative Model for Particle Deposition and Binder Formation from Alcohol-Based Suspensions. *J. Colloid Interface Sci.* **222**, 117–124 (2000).
48. Benekohal, N. P. & Demopoulos, G. P. Green Preparation of TiO₂-ZnO Nanocomposite Photoanodes by Aqueous Electrophoretic Deposition. *J. Electrochem. Soc.* **159**, B602–B610 (2012).
49. Russ, B. E. & Talbot, J. B. A Study of the Adhesion of Electrophoretically Deposited Phosphors. *J. Electrochem. Soc.* **145**, 1245–1252 (1998).
50. Boccaccini, A. R. & Zhitomirsky, I. Application of electrophoretic and electrolytic deposition techniques in ceramics processing. *Curr. Opin. Solid State Mater. Sci.* **6**, 251–260 (2002).

51. Wang, C., Ma, J. & Cheng, W. Formation of polyetheretherketone polymer coating by electrophoretic deposition method. *Surf. Coat. Technol.* **173**, 271–275 (2003).
52. Yang, L., Pang, X., Fox-Rabinovich, G., Veldhuis, S. & Zhitomirsky, I. Electrophoretic deposition of polymer and composite films. *Surf. Eng.* **28**, 585–589 (2012).
53. Verde, M., Peiteado, M., Caballero, A. C., Villegas, M. & Ferrari, B. Electrophoretic Deposition of Transparent ZnO Thin Films from Highly Stabilized Colloidal Suspensions. *J. Colloid Interface Sci.* **373**, 27–33 (2012).
54. Zhitomirsky, I. & Petric, A. Electrophoretic deposition of ceramic materials for fuel cell applications. *J. Eur. Ceram. Soc.* **20**, 2055–2061 (2000).
55. Grandfield, K., Sun, F., FitzPatrick, M., Cheong, M. & Zhitomirsky, I. Electrophoretic deposition of polymer-carbon nanotube–hydroxyapatite composites. *Surf. Coat. Technol.* **203**, 1481–1487 (2009).
56. Zhu, H., Liu, H., Zhitomirsky, I. & Zhu, S. Preparation of metal–organic framework films by electrophoretic deposition method. *Mater. Lett.* **142**, 19–22 (2015).
57. Su, Y. & Zhitomirsky, I. Electrophoretic deposition of graphene, carbon nanotubes and composite films using methyl violet dye as a dispersing agent. *Colloids Surf. Physicochem. Eng. Asp.* **436**, 97–103

(2013).

58. Lee, S. B., Choi, O., Lee, W., Yi, J. W., Kim, B. S., Byun, J. H., ... & Chou, T.W. Processing and characterization of multi-scale hybrid composites reinforced with nanoscale carbon reinforcements and carbon fibers. *Compos. Part Appl. Sci. Manuf.* **42**, 337–344 (2011).

59. Zhitomirsky, I. Cathodic electrophoretic deposition of diamond particles. *Mater. Lett.* **37**, 72–78 (1998).

60. Creus, J., Brezault, F., Rebere, C. & Gadouleau, M. Synthesis and characterisation of thin cerium oxide coatings elaborated by cathodic electrolytic deposition on steel substrate. *Surf. Coat. Technol.* **200**, 4636–4645 (2006).

61. Zhitomirsky, I. Composite nickel hydroxide – polyelectrolyte films prepared by cathodic electrosynthesis. *J. Appl. Electrochem.* **34**, 235–240 (2004).

62. Taxil, P., Massot, L., Nourry, C., Gibilaro, M., Chamelot, P., & Cassayre, L. Lanthanides extraction processes in molten fluoride media: Application to nuclear spent fuel reprocessing. *J. Fluor. Chem.* **130**, 94–101 (2009).

63. Shi, K. & Zhitomirsky, I. Polypyrrole nanofiber–carbon nanotube electrodes for supercapacitors with high mass loading obtained using an organic dye as a co-dispersant. *J. Mater. Chem. A* **1**, 11614–11622 (2013).

64. Besra, L., Uchikoshi, T., Suzuki, T. S. & Sakka, Y. Bubble-Free Aqueous Electrophoretic Deposition (EPD) by Pulse-Potential Application. *J. Am. Ceram. Soc.* **91**, 3154–3159 (2008).
65. Kovtyukhova, N. I. *et al.* Layer-by-Layer Assembly of Ultrathin Composite Films from Micron-Sized Graphite Oxide Sheets and Polycations. *Chem. Mater.* **11**, 771–778 (1999).
66. Lee, Y. H., Zhang, X. Q., Zhang, W., Chang, M. T., Lin, C. T., Chang, K. D., ... & Lin, T. W. Synthesis of Large-Area MoS₂ Atomic Layers with Chemical Vapor Deposition. *Adv. Mater.* **24**, 2320–2325 (2012).
67. Lu, Y., Ganguli, R., Drewien, C. A., Anderson, M. T., Brinker, C. J., Gong, W., ... & Zink, J. I. Continuous formation of supported cubic and hexagonal mesoporous films by sol–gel dip-coating. *Nature* **389**, 364–368 (1997).
68. Pham, V. H., Cuong, T. V., Hur, S. H., Shin, E. W., Kim, J. S., Chung, J. S., & Kim, E. J. Fast and simple fabrication of a large transparent chemically-converted graphene film by spray-coating. *Carbon* **48**, 1945–1951 (2010).
69. Natsume, Y. & Sakata, H. Zinc oxide films prepared by sol-gel spin-coating. *Thin Solid Films* **372**, 30–36 (2000).
70. Sun, X. W., & Kwok, H. S. Optical properties of epitaxially grown zinc oxide films on sapphire by pulsed laser deposition. *Journal of applied physics*, **86**(1), 408-411 (1999).

71. Wang, Y., Angelatos, A. S. & Caruso, F. Template Synthesis of Nanostructured Materials via Layer-by-Layer Assembly [†]. *Chem. Mater.* **20**, 848–858 (2008).
72. Tang, Z., Wang, Y., Podsiadlo, P. & Kotov, N. A. Biomedical Applications of Layer-by-Layer Assembly: From Biomimetics to Tissue Engineering. *Adv. Mater.* **18**, 3203–3224 (2006).
73. Javey, A., Nam, Friedman, R. S., Yan, H. & Lieber, C. M. Layer-by-Layer Assembly of Nanowires for Three-Dimensional, Multifunctional Electronics. *Nano Lett.* **7**, 773–777 (2007).
74. Che, G., Lakshmi, B. B., Martin, C. R., Fisher, E. R. & Ruoff, R. S. Chemical Vapor Deposition Based Synthesis of Carbon Nanotubes and Nanofibers Using a Template Method. *Chem. Mater.* **10**, 260–267 (1998).
75. Suk, J. W., Lee, W. H., Lee, J., Chou, H., Piner, R. D., Hao, Y., ... & Ruoff, R. S. Enhancement of the electrical properties of graphene grown by chemical vapor deposition via controlling the effects of polymer residue. *Nano letters*, **13**(4), 1462-1467 (2013).
76. Reina, A., Jia, X., Ho, J., Nezich, D., Son, H., Bulovic, V., ... & Kong, J. Large area, few-layer graphene films on arbitrary substrates by chemical vapor deposition. *Nano letters*, **9**(1), 30-35 (2008).
77. Dong, X., Li, B., Wei, A., Cao, X., Chan-Park, M. B., Zhang, H., ... & Chen, P. One-step growth of graphene–carbon nanotube hybrid materials by chemical vapor deposition. *Carbon*, **49**(9), 2944-2949 (2011).

78. Thongsuriwong, K., Amornpitoksuk, P. & Suwanboon, S. Structure, morphology, photocatalytic and antibacterial activities of ZnO thin films prepared by sol–gel dip-coating method. *Adv. Powder Technol.* **24**, 275–280 (2013).
79. Li, T., Lee, J., Kobayashi, T. & Aoki, H. Hydroxyapatite coating by dipping method, and bone bonding strength. *J. Mater. Sci. Mater. Med.* **7**, 355–357 (1996).
80. McCool, B. A., Hill, N., DiCarlo, J. & DeSisto, W. J. Synthesis and characterization of mesoporous silica membranes via dip-coating and hydrothermal deposition techniques. *J. Membr. Sci.* **218**, 55–67 (2003).
81. Hall, D. B., Underhill, P. & Torkelson, J. M. Spin coating of thin and ultrathin polymer films. *Polym. Eng. Sci.* **38**, 2039–2045 (1998).
82. Bornside, D. E., Macosko, C. W. & Scriven, L. E. Spin coating: One-dimensional model. *J. Appl. Phys.* **66**, 5185–5193 (1989).
83. Jiang, P. & McFarland, M. J. Large-Scale Fabrication of Wafer-Size Colloidal Crystals, Macroporous Polymers and Nanocomposites by Spin-Coating. *J. Am. Chem. Soc.* **126**, 13778–13786 (2004).
84. Schubert, D. W. Spin coating as a method for polymer molecular weight determination. *Polym. Bull.* **38**, 177–184 (1997).
85. Giroto, C., Rand, B. P., Genoe, J. & Heremans, P. Exploring spray coating as a deposition technique for the fabrication of solution-processed solar cells. *Sol. Energy Mater. Sol. Cells* **93**, 454–458 (2009).

86. Herman, H., Sampath, S. & McCune, R. Thermal Spray: Current Status and Future Trends. *MRS Bull.* **25**, 17–25 (2000).
87. Gärtner, F., Stoltenhoff, T., Schmidt, T. & Kreye, H. The cold spray process and its potential for industrial applications. *J. Therm. Spray Technol.* **15**, 223–232 (2006).
88. Hassani-Gangaraj, S. M., Moridi, A. & Guagliano, M. Critical review of corrosion protection by cold spray coatings. *Surf. Eng.* **31**, 803–815 (2015).
89. Zheng, B. J., Lian, J. S., Zhao, L. & Jiang, Q. Optical and electrical properties of In-doped CdO thin films fabricated by pulse laser deposition. *Appl. Surf. Sci.* **256**, 2910–2914 (2010).
90. Voevodin, A. A. & Donley, M. S. Preparation of amorphous diamond-like carbon by pulsed laser deposition: a critical review. *Surf. Coat. Technol.* **82**, 199–213 (1996).
91. Muth, J. F., Kolbas, R. M., Sharma, A. K., Oktyabrsky, S. & Narayan, J. Excitonic structure and absorption coefficient measurements of ZnO single crystal epitaxial films deposited by pulsed laser deposition. *J. Appl. Phys.* **85**, 7884–7887 (1999).
92. Zhitomirsky, I. Electrophoretic deposition of organic–inorganic nanocomposites. *J. Mater. Sci.* **41**, 8186–8195 (2006).
93. Zhitomirsky, D., Roether, J. A., Boccaccini, A. R. & Zhitomirsky, I. Electrophoretic deposition of bioactive glass/polymer composite coatings

with and without HA nanoparticle inclusions for biomedical applications.

J. Mater. Process. Technol. **209**, 1853–1860 (2009).

94. Boccaccini, A. R., Keim, S., Ma, R., Li, Y. & Zhitomirsky, I. Electrophoretic deposition of biomaterials. *J. R. Soc. Interface* **7**, S581–S613 (2010).

95. Ishihara, T., Sato, K. & Takita, Y. Electrophoretic Deposition of Y₂O₃-Stabilized ZrO₂ Electrolyte Films in Solid Oxide Fuel Cells. *J. Am. Ceram. Soc.* **79**, 913–919 (1996).

96. Besra, L., Compson, C., & Liu, M. Electrophoretic Deposition of YSZ Particles on Non - Conducting Porous NiO–YSZ Substrates for Solid Oxide Fuel Cell Applications. *Journal of the American Ceramic Society*, **89**(10), 3003-3009 (2006).

97. Singhal, S. C. Science and technology of solid-oxide fuel cells. *Mrs Bulletin*, **25**(3), 16-21 (2000).

98. Zhang, H., Zhang, X., Zhang, D., Sun, X., Lin, H., Wang, C., & Ma, Y. One-Step Electrophoretic Deposition of Reduced Graphene Oxide and Ni(OH)₂ Composite Films for Controlled Syntheses Supercapacitor Electrodes. *J. Phys. Chem. B* **117**, 1616–1627 (2013).

99. Thomas, B. J. C., Boccaccini, A. R. & Shaffer, M. S. P. Multi-Walled Carbon Nanotube Coatings Using Electrophoretic Deposition (EPD). *J. Am. Ceram. Soc.* **88**, 980–982 (2005).

100. Singh, A., English, N. J. & Ryan, K. M. Highly Ordered Nanorod

Assemblies Extending over Device Scale Areas and in Controlled Multilayers by Electrophoretic Deposition. *J. Phys. Chem. B* **117**, 1608–1615 (2013).

101. Wang, Y.-C., Leu, I.-C. & Hon, M.-H. Preparation of Nanosized ZnO Arrays by Electrophoretic Deposition. *Electrochem. Solid-State Lett.* **5**, C53–C55 (2002).

102. Staiger, M. P., Pietak, A. M., Huadmai, J. & Dias, G. Magnesium and its alloys as orthopedic biomaterials: A review. *Biomaterials* **27**, 1728–1734 (2006).

103. Razavi, M., Fathi, M., Savabi, O., Beni, B. H., Vashae, D., & Tayebi, L. Nanostructured merwinite bioceramic coating on Mg alloy deposited by electrophoretic deposition. *Ceram. Int.* **40**, 9473–9484 (2014).

104. Pang, X. & Zhitomirsky, I. Electrophoretic deposition of composite hydroxyapatite-chitosan coatings. *Mater. Charact.* **58**, 339–348 (2007).

105. Minh, N. Q. Solid oxide fuel cell technology—features and applications. *Solid State Ion.* **174**, 271–277 (2004).

106. Negishi, H., Sakai, N., Yamaji, K., Horita, T. & Yokokawa, H. Application of Electrophoretic Deposition Technique to Solid Oxide Fuel Cells. *J. Electrochem. Soc.* **147**, 1682–1687 (2000).

107. Negishi, H., Yamaji, K., Sakai, N., Horita, T., Yanagishita, H., & Yokokawa, H. Electrophoretic deposition of YSZ powders for solid oxide

- fuel cells. *J. Mater. Sci.* **39**, 833–838 (2004).
108. Jia, L., Lü, Z., Huang, X., Liu, Z., Chen, K., Sha, X., ... & Su, W. Preparation of YSZ film by EPD and its application in SOFCs. *J. Alloys Compd.* **424**, 299–303 (2006).
109. Talebi, T., Haji, M., Raissi, B. & Maghsoudipour, A. YSZ electrolyte coating on NiO–YSZ composite by electrophoretic deposition for solid oxide fuel cells (SOFCs). *Int. J. Hydrog. Energy* **35**, 9455–9459 (2010).
110. Snook, G. A., Kao, P. & Best, A. S. Conducting-polymer-based supercapacitor devices and electrodes. *J. Power Sources* **196**, 1–12 (2011).
111. Liu, C., Yu, Z., Neff, D., Zhamu, A., & Jang, B. Z. Graphene-based supercapacitor with an ultrahigh energy density. *Nano letters*, **10**(12), 4863-4868 (2010).
112. Frackowiak, E., Metenier, K., Bertagna, V. & Beguin, F. Supercapacitor electrodes from multiwalled carbon nanotubes. *Appl. Phys. Lett.* **77**, 2421–2423 (2000).
113. Boccaccini, A. R., Cho, J., Roether, J. A., Thomas, B. J., Minay, E. J., & Shaffer, M. S. *Carbon* **44**, 3149–3160 (2006).
114. Du, C. & Pan, N. High power density supercapacitor electrodes of carbon nanotube films by electrophoretic deposition. *Nanotechnology* **17**, 5314 (2006).

115. Khoo, E., Lee, P. S. & Ma, J. Electrophoretic deposition (EPD) of WO₃ nanorods for electrochromic application. *J. Eur. Ceram. Soc.* **30**, 1139–1144 (2010).
116. Wang, H. W., Ting, C. F., Hung, M. K., Chiou, C. H., Liu, Y. L., Liu, Z., ... & Ringer, S. P. Three-dimensional electrodes for dye-sensitized solar cells: synthesis of indium–tin-oxide nanowire arrays and ITO/TiO₂ core–shell nanowire arrays by electrophoretic deposition. *Nanotechnology* **20**, 055601 (2009).
117. Ohnishi, S., Hirokawa, Y., Shiosaki, T. & Kawabata, A. Chemical Vapor Deposition of Single-Crystalline ZnO Film with Smooth Surface on Intermediately Sputtered ZnO Thin Film on Sapphire. *Jpn. J. Appl. Phys.* **17**, 773 (1978).
118. Umar, A., Kim, S. H., Suh, E. K., & Hahn, Y. B. Ultraviolet-emitting javelin-like ZnO nanorods by thermal evaporation: growth mechanism, structural and optical properties. *Chemical physics letters*, **440**(1-3), 110-115 (2007).
119. Chen, J., A e, L., Aichele, C. & Lux-Steiner, M. C. High internal quantum efficiency ZnO nanorods prepared at low temperature. *Appl. Phys. Lett.* **92**, 161906 (2008).
120. Zhao, A. W., Ye, C. H., Meng, G. W., Zhang, L. D. & Ajayan, P. M. Tellurium nanowire arrays synthesized by electrochemical and electrophoretic deposition. *J. Mater. Res.* **18**, 2318–2322 (2003).

121. Wahyuningsih, S., Ramelan, A. H., Munifa, R. M. I., Saputri, L. N. M. Z. & Chasanah, U. Synthesis of TiO₂ nanorods from titania and titanyl sulfate produced from ilmenite dissolution by hydrothermal method. *J. Phys. Conf. Ser.* **776**, 012044 (2016).
122. Edgar, K. J. Cellulose esters in drug delivery. *Cellulose* **14**, 49–64 (2007).
123. Nyholm, L., Nyström, G., Mihranyan, A. & Strømme, M. Toward Flexible Polymer and Paper-Based Energy Storage Devices. *Adv. Mater.* **23**, 3751–3769 (2011).
124. Tankhiwale, R., & Bajpai, S. K. Graft copolymerization onto cellulose-based filter paper and its further development as silver nanoparticles loaded antibacterial food-packaging material. *Colloids and Surfaces B: Biointerfaces*, **69**(2), 164-168 (2009).
125. El-Saied, H., Basta, A. H. & Gobran, R. H. Research Progress in Friendly Environmental Technology for the Production of Cellulose Products (Bacterial Cellulose and Its Application). *Polym.-Plast. Technol. Eng.* **43**, 797–820 (2004).
126. Wu, C.-N., Saito, T., Fujisawa, S., Fukuzumi, H. & Isogai, A. Ultrastrong and High Gas-Barrier Nanocellulose/Clay-Layered Composites. *Biomacromolecules* **13**, 1927–1932 (2012).
127. Pinto, R. J. B., Marques, P. A. A. P., Barros-Timmons, A. M., Trindade, T. & Neto, C. P. Novel SiO₂/cellulose nanocomposites

obtained by in situ synthesis and via polyelectrolytes assembly. *Compos.*

Sci. Technol. **68**, 1088–1093 (2008).

128. Zhou, T., Zhang, J., Qiao, J., Liu, L., Jiang, G., Zhang, J., & Liu, Y.

High durable poly(vinyl alcohol)/Quaterized hydroxyethylcellulose
ethoxylate anion exchange membranes for direct methanol alkaline fuel
cells. *J. Power Sources* **227**, 291–299 (2013).

129. Li, J., Lewis, R. B. & Dahn, J. R. Sodium Carboxymethyl Cellulose
A Potential Binder for Si Negative Electrodes for Li-Ion Batteries.

Electrochem. Solid-State Lett. **10**, A17–A20 (2007).

130. Nadagouda, M. N., & Varma, R. S. Synthesis of thermally stable
carboxymethyl cellulose/metal biodegradable nanocomposites for
potential biological applications. *Biomacromolecules*, **8**(9), 2762-2767
(2007).

131. Wu, X. J. & Choi, M. M. F. An optical glucose biosensor based on
entrapped-glucose oxidase in silicate xerogel hybridised with
hydroxyethyl carboxymethyl cellulose. *Anal. Chim. Acta* **514**, 219–226
(2004).

132. Ninan, N., Muthiah, M., Park, I. K., Elain, A., Thomas, S., &
Grohens, Y. Pectin/carboxymethyl cellulose/microfibrillated cellulose
composite scaffolds for tissue engineering. *Carbohydr. Polym.* **98**, 877–
885 (2013).

133. Butun, S., Ince, F. G., Erdugan, H. & Sahiner, N. One-step

fabrication of biocompatible carboxymethyl cellulose polymeric particles for drug delivery systems. *Carbohydr. Polym.* **86**, 636–643 (2011).

134. Boussif, O., Lezoualc'h, F., Zanta, M. A., Mergny, M. D., Scherman, D., Demeneix, B., & Behr, J. P. A versatile vector for gene and oligonucleotide transfer into cells in culture and in vivo: polyethylenimine. *Proc. Natl. Acad. Sci.* **92**, 7297–7301 (1995).

135. Wiseman, J. W., Goddard, C. A., McLelland, D. & Colledge, W. H. A comparison of linear and branched polyethylenimine (PEI) with DCCChol/DOPE liposomes for gene delivery to epithelial cells in vitro and in vivo. *Gene Ther.* **10**, 1654–1662 (2003).

136. Herlem, M. *et al.* Surface modification of p-Si by a polyethylenimine coating: influence of the surface pre-treatment. Application to a potentiometric transducer as pH sensor. *Electrochimica Acta* **47**, 2597–2602 (2002).

137. Wang, J. *et al.* Polyethylenimine coated bacterial cellulose nanofiber membrane and application as adsorbent and catalyst. *J. Colloid Interface Sci.* **440**, 32–38 (2015).

138. Mészáros, R., Thompson, L., Bos, M. & de Groot, P. Adsorption and Electrokinetic Properties of Polyethylenimine on Silica Surfaces. *Langmuir* **18**, 6164–6169 (2002).

139. Wang, J. & Gao, L. Adsorption of Polyethylenimine on Nanosized Zirconia Particles in Aqueous Suspensions. *J. Colloid Interface Sci.* **216**,

436–439 (1999).

140. Sun, Y., Ata, M. S., & Zhitomirsky, I. Electrophoretic deposition of linear polyethylenimine and composite films. *Surface Engineering*, **29**(7), 495-499 (2013).

141. Nagarajan, N., Humadi, H. & Zhitomirsky, I. Cathodic electrodeposition of MnO_x films for electrochemical supercapacitors. *Electrochimica Acta* **51**, 3039–3045 (2006).